PHILOSOPHICAL MAGAZINE

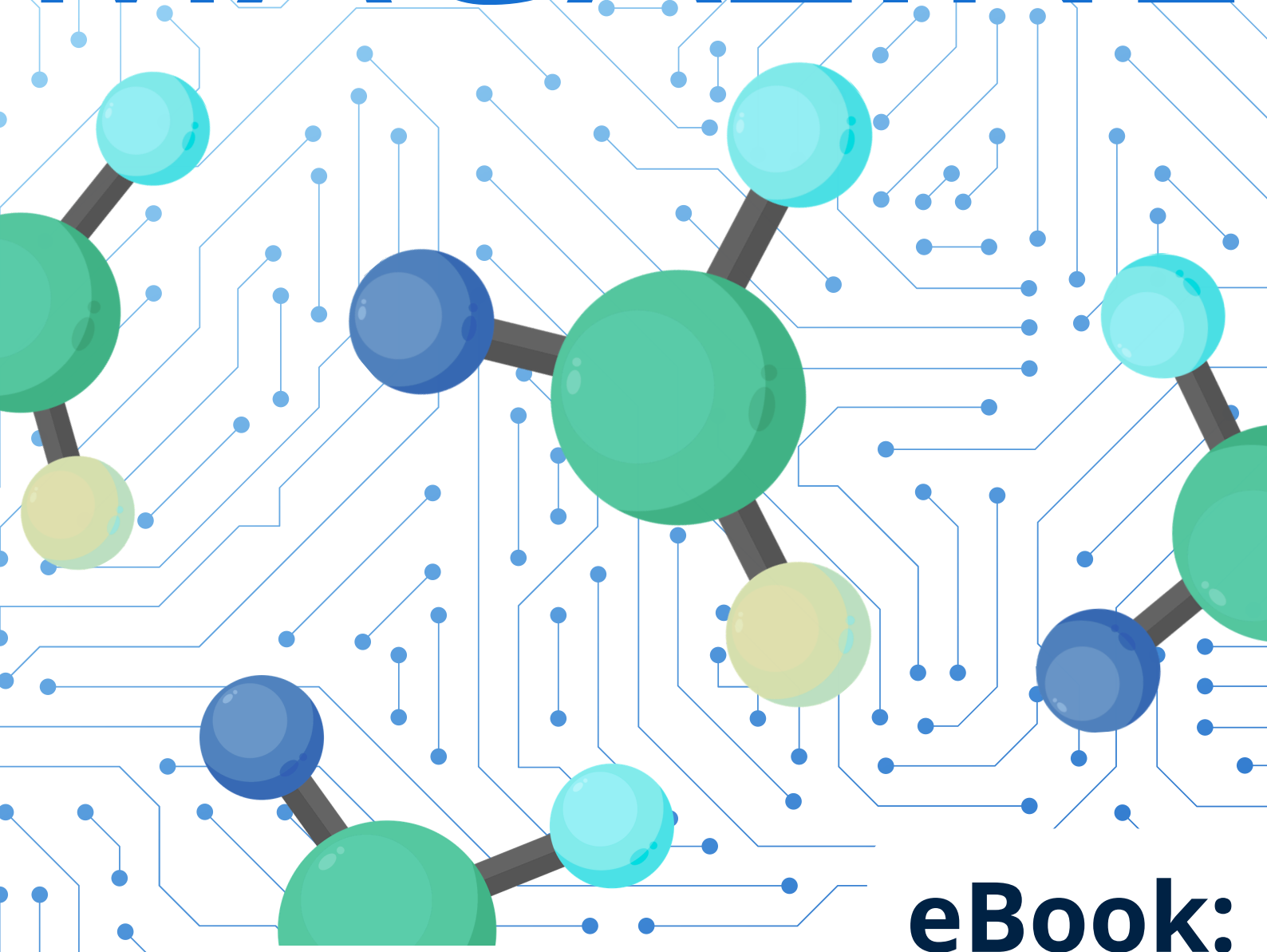

eBook: Machine learning in materials science

Taylor & Francis
by informa

eBook

Machine learning in materials science

Contents:

- Machine learning approach for predicting the fracture toughness of bulk metallic glasses
- Phase diagram determination using machine learning methods in materials science and engineering: a review
- Prediction of impact damage to Fe-based amorphous coatings via interpretable machine learning
- An intelligent screening for rare earth in Ni alloy based on machine learning and multi-objective optimisation
- Development of a force-matched embedded-atom method (EAM) potential for rhodium-barium alloy system

Taylor & Francis
by informa

Philosophical Magazine

ISSN: 1478-6435 (Print) 1478-6443 (Online) Journal homepage: www.tandfonline.com/journals/tphm20

Machine learning approach for predicting the fracture toughness of bulk metallic glasses

Hui Guo, Wenhai Sun, Weiyan Lu, Qinghui Sun, Mingsheng Wang & Limin Xu

To cite this article: Hui Guo, Wenhai Sun, Weiyan Lu, Qinghui Sun, Mingsheng Wang & Limin Xu (2025) Machine learning approach for predicting the fracture toughness of bulk metallic glasses, Philosophical Magazine, 105:17, 991-1005, DOI: 10.1080/14786435.2025.2484719

To link to this article: https://doi.org/10.1080/14786435.2025.2484719

PHILOSOPHICAL MAGAZINE
2025, VOL. 105, NO. 17, 991–1005
https://doi.org/10.1080/14786435.2025.2484719

Taylor & Francis
Taylor & Francis Group

Machine learning approach for predicting the fracture toughness of bulk metallic glasses

Hui Guo [a], Wenhai Sun[b], Weiyan Lu[b], Qinghui Sun[a], Mingsheng Wang[c] and Limin Xu[d]

[a]Institute of Applied Physics, Jiangxi Academy of Sciences, Nanchang, People's Republic of China; [b]Shenyang National Laboratory for Materials Science, Institute of Metal Research, Chinese Academy of Sciences, Shenyang, People's Republic of China; [c]Institute of Metal Research, Chinese Academy of Sciences, Shenyang, People's Republic of China; [d]Key Laboratory of Photonic Technology for Integrated Sensing and Communication, Ministry of Education, Guangdong University of Technology, Guangzhou, People's Republic of China

ABSTRACT

This study developed a machine learning (ML) model to accurately predict the fracture toughness, K_Q, of bulk metallic glasses (BMGs). To achieve this goal, this work established a dataset of 85 BMGs from the literature comprising the chemical composition and fracture toughness of these BMGs. Various ML algorithms were then employed to develop predictive models for fracture toughness based on the atomic chemical concentration alone. Among the eight ML models that were compared, the extremely randomised trees regression (ETR) model performed the best performance, with the highest determination coefficient (R^2) of 0.779 and the lowest mean absolute error (MAE) of 11.826 MPa$\sqrt{m}$ on the testing set. The generalizability was shown by the pseudo-ternary diagram $Al_xNi_{y\text{-}4.5}Y_{4.5}Co_{98.5\text{-}x\text{-}y}La_{1.5}$, which demonstrated how the ETR model predicts K_Q based on chemical composition. These findings indicate that the ETR model is very reliable and has great potential for predicting the fracture toughness of BMGs.

ARTICLE HISTORY
Received 31 January 2025
Accepted 21 March 2025

KEYWORDS
Machine learning; fracture toughness; bulk metallic glasses; prediction

1. Introduction

Over the past three decades, bulk metallic glasses (BMGs) have attracted considerable attention owing to extraordinary strength, high elasticity, and remarkable corrosion resistance [1]. In general, fracture toughness, which reflects the resistance to crack propagation, is an important property of engineering materials [2]. Often, BMGs are not sufficiently tough to obtain fracture

CONTACT Hui Guo guohui@jxas.ac.cn Institute of Applied Physics, Jiangxi Academy of Sciences, Nanchang 330029, People's Republic of China; Mingsheng Wang mswang@imr.ac.cn Institute of Metal Research, Chinese Academy of Sciences, Shenyang 110016, People's Republic of China; Limin Xu xulimin@gdut.edu.cn Key Laboratory of Photonic Technology for Integrated Sensing and Communication, Ministry of Education, Guangdong University of Technology, Guangzhou 510006, People's Republic of China
Supplemental data for this article can be accessed online at https://doi.org/10.1080/14786435.2025.2484719.

toughness K_{IC} when fatigue precracked samples are subjected to the crack tip opening displacement (CTOD) test. For many BMGs, the fracture toughness, K_Q, is highly variable, ranging from 10 to 130 MPa$\sqrt{m}$ when assessed without the pre-fatigue procedure. Traditional material design, fabrication, and performance characterisation are expensive and time-consuming processes that involve trial and error. Accordingly, establishing a feasible and inexpensive method to evaluate the fracture toughness of BMGs is important.

Intelligent machine learning (ML) is an interdisciplinary approach that involves statistics and computer science. ML can derive additional insights from complex datasets while reducing level of risk, research cost, and time, thereby shortening the development cycle of advanced functional materials. In recent years, ML technology has been successfully applied to the design and prediction of BMGs across various domains, such as determining glass forming ability [3–7] and identifying flow defects [8], soft magnetism [9–18], neutron absorption [19], elastic modulus [4, 20], hardness [21], etc. Sun et al. [3] developed ML models to identify BMGs with good glass-forming ability. Li et al. [20] established a variety of ML models to predict and explain the elastic properties of BMGs, ultimately achieving a well-generalized prediction model. Liu et al. [21] utilised ML to predict the hardness of BMGs. Nevertheless, there is currently no research involving the use of ML to predict the fracture toughness of BMGs. We aim to develop a fracture toughness model for BMGs using ML with powerful modelling ability and then apply the ML-K_Q model to alloy design.

In the present work, various ML algorithms were employed to develop predictive models for fracture toughness of BMGs based on the atomic chemical concentration alone, and then, model accuracy was compared. To verify the generalizability of the optimal model, a pseudo-ternary diagram was used to predict fracture toughness. This research provides a novel quick, simple, and effective method for predicting the fracture toughness of BMGs.

2. Materials and methods

2.1. Data collection

The dataset utilised in this study was collected from experimental findings published in previous literature [22–54]. The dataset comprises the composition of 85 BMGs and the corresponding fracture toughness at room temperature. The collected data are provided in the Supplementary Materials. When the K_Q value of a BMG was slightly different in various studies, the average K_Q was taken. The dataset includes an array of alloy types, including Pd-, Pt-, Zr-, Cu-, Mg-, Ni-, Fe-, Ti-, Ce-, Ca-, and La-based BMGs. To quantitatively predict the effects of alloying elements on the fracture toughness of BMGs, we present a workflow of the data collection, feature construction, and machine learning

processes used in this study in Figure 1. To accomplish the study objective, we divided the input/output features into chemical elements and the corresponding fracture toughness. Figure 2 shows the distribution of the input alloy elements, indicating 32 input features (Cu, Ni, Zr, Al, Ti, Fe, B, P, C, Mo, Mg, Y, Cr, Pd, Nb, Si, Ag, Be, Er, Co, Sn, Hf, Nd, Gd, Mn, Ce, Ca, Tb, La, V,

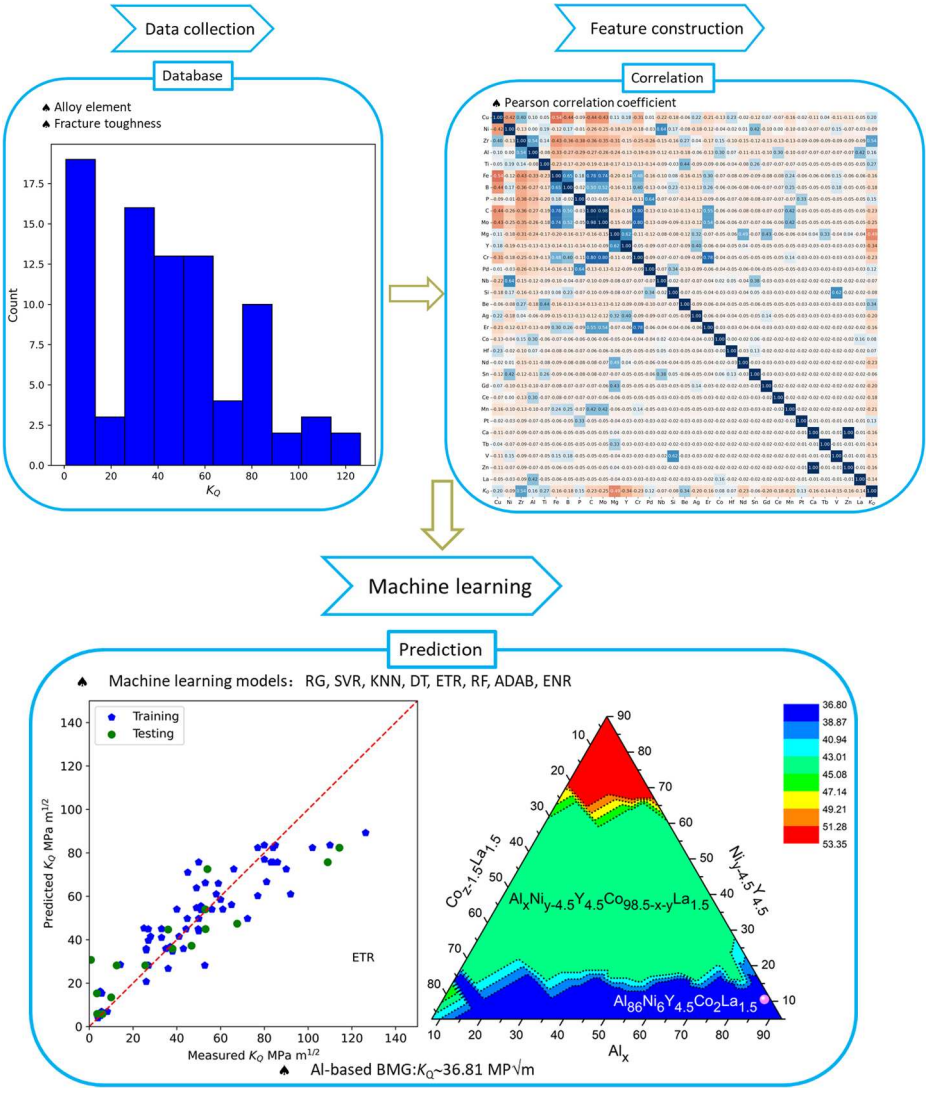

Figure 1. Workflow for ML prediction in this study. Experimental data on BMGs were obtained from published literature. The alloying elements were chosen as input parameters affecting the fracture toughness of the BMGs. Data analysis was conducted to evaluate the strength of the correlation between the input features and fracture toughness of the BMGs. The results of the data analysis were subsequently used to train various ML models.

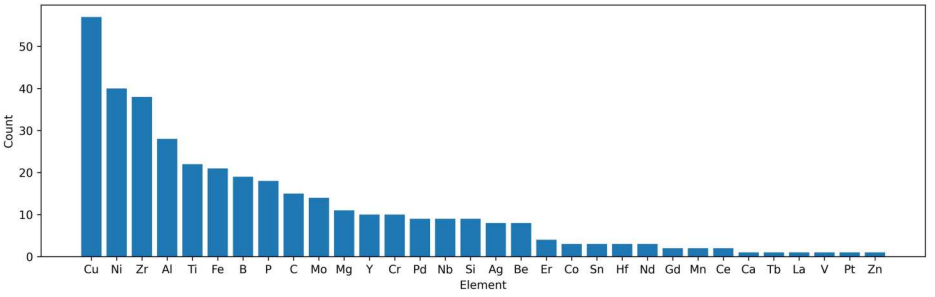

Figure 2. Distribution of the alloy elements in the dataset.

Pt, and Zn). Figure 3 shows the distribution of the output fracture toughness, ranging between 0 and 130 MPa$\sqrt{\text{m}}$.

2.2. Feature construction

As the range and scale differ among the features, standardisation was performed on the input features to normalise the mean and variance.

$$x^* = \frac{x - x_{\text{ave}}}{x_{\text{std}}} \tag{1}$$

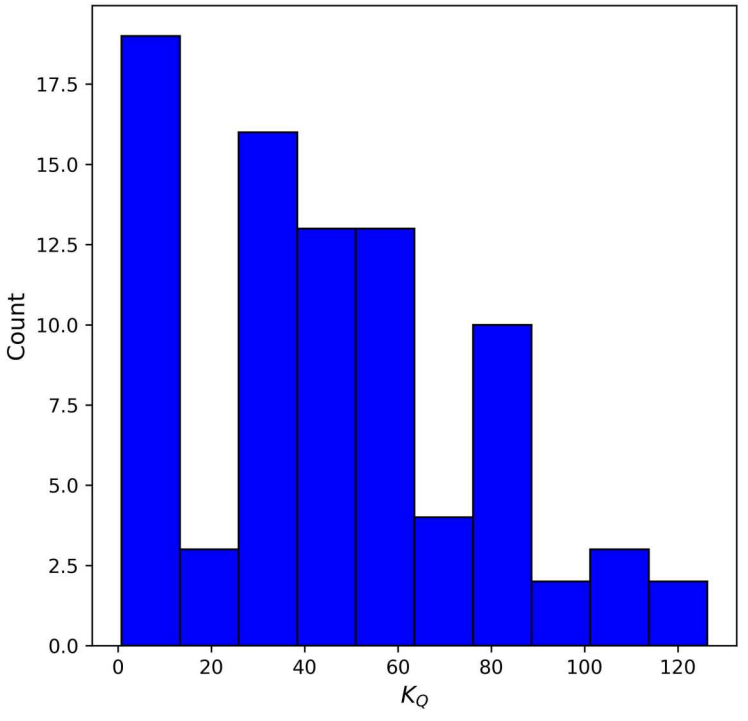

Figure 3. Distribution of fracture toughness K_Q in the dataset.

where x^* is the standardised value, x_{ave} is the mean and x_{std} is the standard deviation.

The Pearson correlation coefficient (PCC) has been extensively used to perform correlation analyses between features [55]. The PCC is a statistical measure that is used to assess the linear correlation between two continuous variables by computing their covariance and standard deviations, given by Eq. (2),

$$PCC = \frac{\sum_{i=1}^{n}(x_i - \overline{x_i})(y_i - \overline{y_i})}{\sqrt{\sum_{i=1}^{n}(x_i - \overline{x_i})^2 \sum_{i=1}^{n}(y_i - \overline{y_i})^2}} \tag{2}$$

where x_i and y_i represent the input feature and target variable, respectively, and $\overline{xi}$ and $\overline{yi}$ represent the mean values of x_i and y_i, respectively. The PCC ranges from – 1–1, where – 1 indicates a perfect negative correlation, 0 indicates no correlation, and 1 indicates a perfect positive correlation.

2.3. Machine learning

In this study, the ML algorithm was implemented by the open source Scikit-Learn in the Python 3.9.0 environment [56]. We tested eight commonly used ML models, including ridge regression (RG) [57], support vector regression (SVR) [58], k-nearest neighbour regression (KNN) [59], decision tree regression (DT) [60], extremely randomised trees regression (ETR) [61], random forest regression (RF) [62], AdaBoost regression (ADAB) [63], and elastic net regression (ENR) [64]. The performance and ability of all the mentioned machine learning models to predict fracture toughness were compared to identify the model most suitable for the data.

During the model development process, the dataset was randomly divided into training (80%) and testing (20%) sets. The training set was used to adjust hyperparameters through a grid search and train the models. The testing set was subsequently used to validate the models' effectiveness. To mitigate the potential bias from dataset partitioning, fivefold cross-validation was employed.

To quantitatively compare the predictive performance of different algorithms, the determination coefficient (R^2) and mean absolute error (MAE) are commonly considered evaluation metrics [65], which are described as follows:

$$R^2 = 1 - \frac{\sum_{i=1}^{n}(y_i - \widehat{y_i})^2}{\sum_{i=1}^{n}(y_i - \overline{y_i})^2} \tag{3}$$

$$MAE = \frac{1}{n}\sum_{i=1}^{n}|y_i - \widehat{y_i}| \tag{4}$$

where y_i, $\overline{\text{yi}}$ and $\widehat{\text{y}_\text{i}}$ denote the measured, average and predicted i-th fracture toughness values, respectively. The R^2 value ranges from negative infinity to 1, where a value closer to 1 denotes a better ability of the model to explain the variability of the dependent variable and a higher degree of fit. The MAE value ranges from 0 to positive infinity, with a value closer to 0 indicating better accuracy of the model. This process was repeated five times, and the performance was averaged over the iterations to determine the final model performance.

3. Results and discussion

3.1. Model prediction

Figure 4 shows the heatmap based on the PCC. This heatmap reflects the correlation between 32 input features and K_Q. Notably, the PCC values between the alloying elements (input feature) and fracture toughness (output feature) are relatively low, indicating the absence of multicollinearity issues.

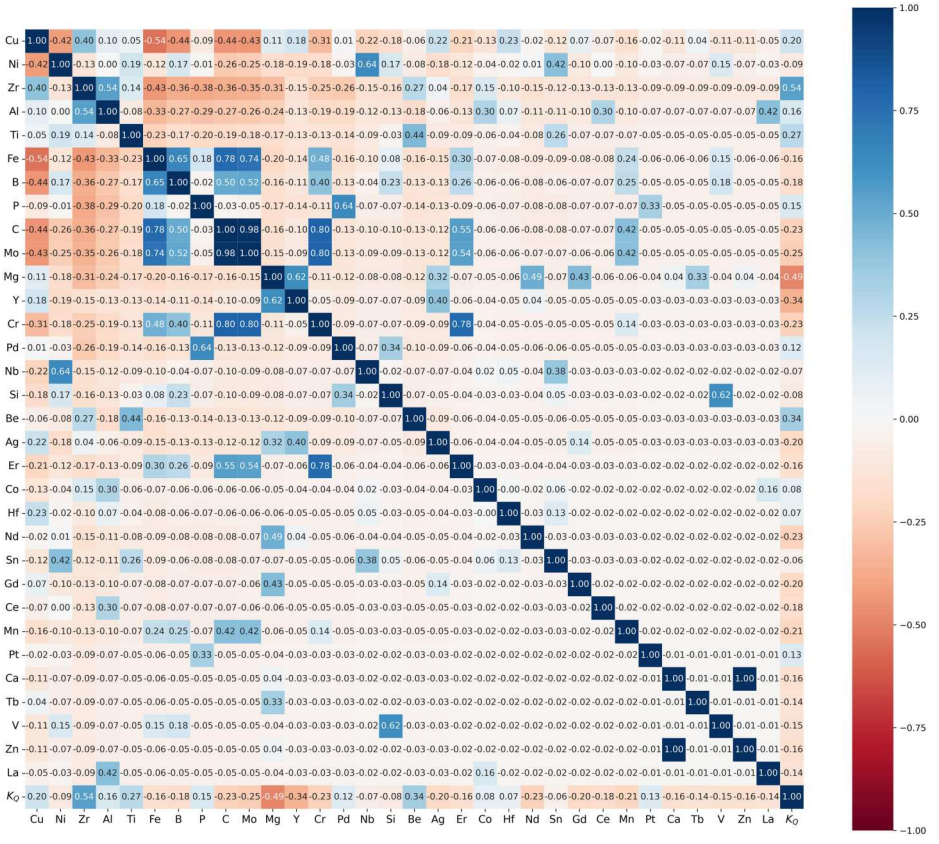

Figure 4. Pearson correlation between 32 input alloy elements (Cu, Ni, Zr, Al, Ti, Fe, B, P, C, Mo, Mg, Y, Cr, Pd, Nb, Si, Be, Ag, Er, Co, Hf, Nd, Sn, Gd, Ce, Mn, Pt, Ca, Tb, V, Zn, and La) and one output fracture toughness K_Q.

To construct the optimal model for predicting K_Q, eight widely used ML models, RG, SVR, KNN, DT, ETR, RF, ADAB, and ENR, were employed and compared. In ML algorithms, several hyperparameters can have a significant effect on the model's ability to accurately fit the data. In order to optimise the eight models, the hyperparameters were tuned via a grid search. The search space and optimal values of different parameters are summarised in Table 1.

Figure 5 presents the performance metrics, R^2 and MAE values from the eight ML models, utilising the optimised hyperparameters. The performance metrics obtained after hyperparameter tuning are summarised in Table 2. The prediction accuracies of the models are in the order of ETR > DT > RF > KNN > ENR > RG > ADAB > SVR. Among these models, the ETR model demonstrated the highest R^2 of 0.779 and the lowest MAE of 11.826 MPa$\sqrt{\text{m}}$ on the testing set, indicating superior prediction accuracy and stronger predictive ability.

Figure 6 displays a comparison between the measured and predicted K_Q values of the eight ML algorithms equipped with optimised hyperparameters on the training and testing sets. The x-axis shows the measured K_Q values from experiments, and the y-axis shows the predicted K_Q values of different regression models. The red diagonal $y = x$ indicates perfect fitting. Each point corresponds to the predicted and measured values of a unique BMG. The closer the points are to the red diagonal line, the smaller the prediction errors. The diagonal distribution suggests that the predicted K_Q values align well with the measured K_Q values, confirming the effectiveness of the model in predicting the fracture toughness of BMGs in this context. Among the eight ML models, the ETR model consistently outperforms the other prediction models, demonstrating the best performance in both the training and testing sets.

Figures 5 and 6 show that the ETR model is the optimal algorithm for predicting fracture toughness in this study. The outstanding performance of the ETR model primarily stems from its characteristics as an ensemble learning algorithm for complex nonlinear relationships. Moreover, ETR leverages the use of multiple decision trees, employing randomised feature and data subset selection during tree construction to minimise overfitting and enhance robustness. This feature enables ETR to perform exceptionally well in predicting fracture toughness, particularly in handling complex and high-dimensional datasets.

3.2. Model validation

Al-based BMGs exhibit exceptional specific strength, good ductility and good corrosion resistance [66, 67]. For these reasons, substantial attention has been given to investigate the comprehensive properties of Al-based BMGs,

Table 1. Hyperparameter adjustments.

Model	Hyperparameters	Search range	Optimal hyperparameters	Model	Hyperparameters	Search range	Optimal Hyperparameters
RG	alpha	[1, 100]	27	ETR	n_estimators	[1, 50]	2
	random_state	[1, 100]	1		max_depth	[1, 20]	14
					min_samples_split	[2, 10]	6
					min_samples_leaf	[1, 10]	1
					max_features	[1, 20]	9
					random_state	[1, 60]	6
SVR	degree	[1, 10]	1	RF	n_estimators	[1, 10]	6
	C	[1, 30]	1		max_depth	[1, 20]	8
	gamma	[1, 10]	1		min_samples_split	[2, 10]	6
	epsilon	[1, 10]	2		min_samples_leaf	[1, 10]	1
	kernel	['linear', 'poly', 'rbf', 'sigmoid']	linear		max_features	[1, 10]	6
					random_state	[1, 50]	27
KNN	n_neighbors	[1, 10]	2	ADAB	n_estimators	[1, 100]	6
	weights	['uniform', 'distance']	uniform		learning_rate	[0.01, 1]	0.02
	leaf_size	[1, 40]	1		random_state	[1, 50]	35
	p	[1, 2]	1		loss	['linear', 'exponential', 'square']	square
	algorithm	['auto', 'kd_tree', 'brute', 'ball_tree']	auto				
DT	max_depth	[1, 20]	7	ENR	alpha	[0, 1]	1
	min_samples_leaf	[1, 10]	1		l1_ratio	[0, 1]	1
	min_samples_split	[2, 10]	8		random_state	[0, 50]	1
	max_features	[1, 20]	9				
	random_state	[1, 40]	23				
	splitter	['best','random']	random				

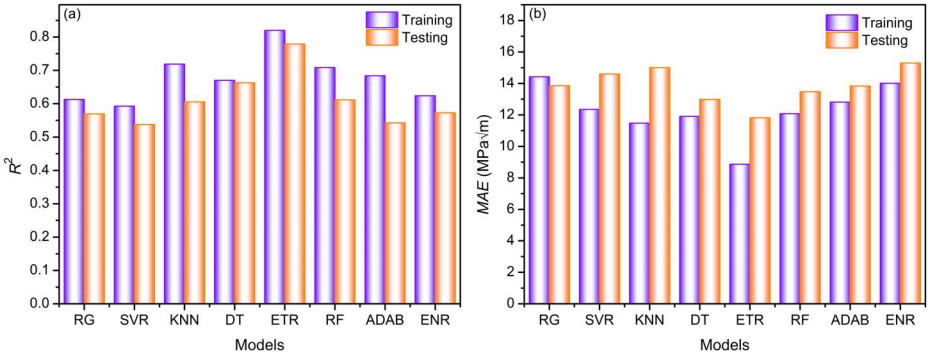

Figure 5. R^2 and MAE values of eight ML models on the training and testing datasets.

Table 2. Performance metrics of R^2, MAE, and Pearsonr of the eight ML models on the training and testing sets.

Model	R^2_train	MAE_train	Pearsonr_train	R^2_test	MAE_test	Pearsonr_test
RG	0.613	14.427	0.796	0.570	13.854	0.761
SVR	0.593	12.352	0.792	0.538	14.603	0.735
KNN	0.719	11.481	0.849	0.606	15.009	0.784
DT	0.670	11.907	0.819	0.663	12.989	0.846
ETR	0.820	8.871	0.910	0.779	11.826	0.911
RF	0.709	12.085	0.855	0.612	13.476	0.788
ADAB	0.684	12.817	0.828	0.543	13.840	0.738
ENR	0.624	14.014	0.795	0.573	15.300	0.771

especially their fracture toughness. Unfortunately, the maximum diameter obtained thus far for bulk glassy Al-rich BMGs is only ~ 1.5 mm [68, 69]. This does not meet the required sample size necessary for the CTOD test. Our ETR model can be used to predict the fracture toughness without conducting a CTOD test.

In order to validate the generalizability of the ETR model, we constructed a hypothetical K_Q of $Al_xNi_{y\text{-}4.5}Y_{4.5}Co_{98.5\text{-}x\text{-}y}La_{1.5}$ BMG with $8 \leq$ Al at.% ≤ 93, $5 \leq$ Ni at.% ≤ 90, $2 \leq$ Co at.% ≤ 87, in a pseudo-ternary diagram, as demonstrated in Figure 7. The K_Q values for the $Al_xNi_{y\text{-}4.5}Y_{4.5}Co_{98.5\text{-}x\text{-}y}La_{1.5}$ BMG predicted using the ETR model range from 36.80–53.35 MPa$\sqrt{m}$. For the $Al_{86}Ni_6Y_{4.5}Co_2La_{1.5}$ BMG with high yield strength of 1050 MPa [66, 68], the K_Q value is predicted to be 36.81 MPa$\sqrt{m}$ with the ETR model, which is comparable to the 35 MPa$\sqrt{m}$ predicted by nanoindentation [70]. The location of the $Al_{86}Ni_6Y_{4.5}Co_2La_{1.5}$ BMG is indicated on the pseudo-ternary diagram. Upon analysis, it is evident that the ETR model is more robust for predicting the K_Q of BMGs.

4. Conclusions

(1) Various ML algorithms, namely, RG, SVR, KNN, DT, ETR, RF, ADAB, and ENR, were constructed and compared to evaluate fracture toughness based on the atomic chemical concentration alone.

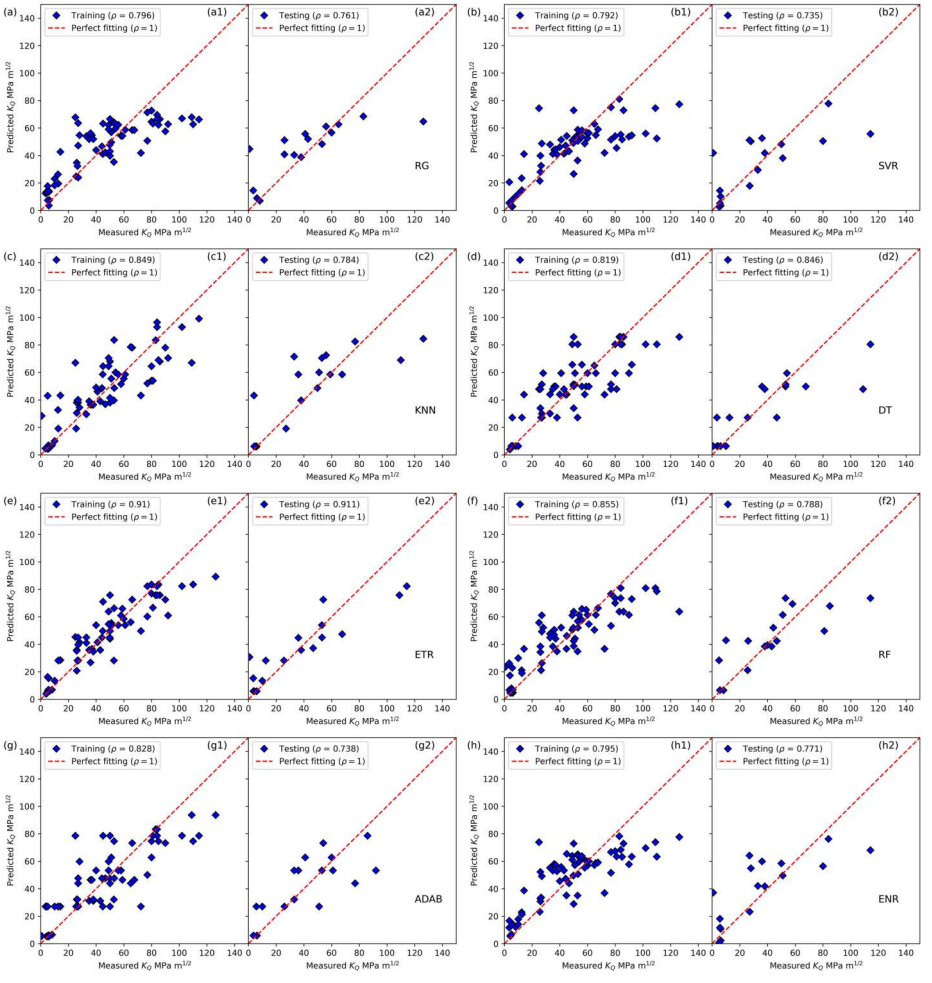

Figure 6. Measured versus predicted K_Q of eight ML models on the training dataset and testing dataset by (a) RG, (b) SVR, (c) KNN, (d) DT, (e) ETR, (f) RF, (g) ADAB, and (h) ENR.

(2) Among the eight ML models, the ETR model exhibited the highest prediction accuracy on the test set, with the largest R^2 value of 0.779 and the smallest MAE of 11.826 MPa$\sqrt{\text{m}}$.

(3) A pseudo-ternary diagram of $Al_xNi_{y\text{-}4.5}Y_{4.5}Co_{98.5\text{-}x\text{-}y}La_{1.5}$ was constructed from the ETR model. The fracture toughness K_Q of the $Al_{86}Ni_6Y_{4.5}Co_2La_{1.5}$ BMG was predicted to be ~ 36.81 MPa$\sqrt{\text{m}}$.

Credit authorship contribution statement

H. Guo: Methodology, Formal analysis, Software, Validation, Investigation, Data curation, Conceptualisation, Writing – original draft, Writing – review & editing, Resources, Project administration. **W.H. Sun:** Methodology, Data curation. **W.Y. Lu:** Methodology, Data Curation. **Q.H. Sun:** Methodology,

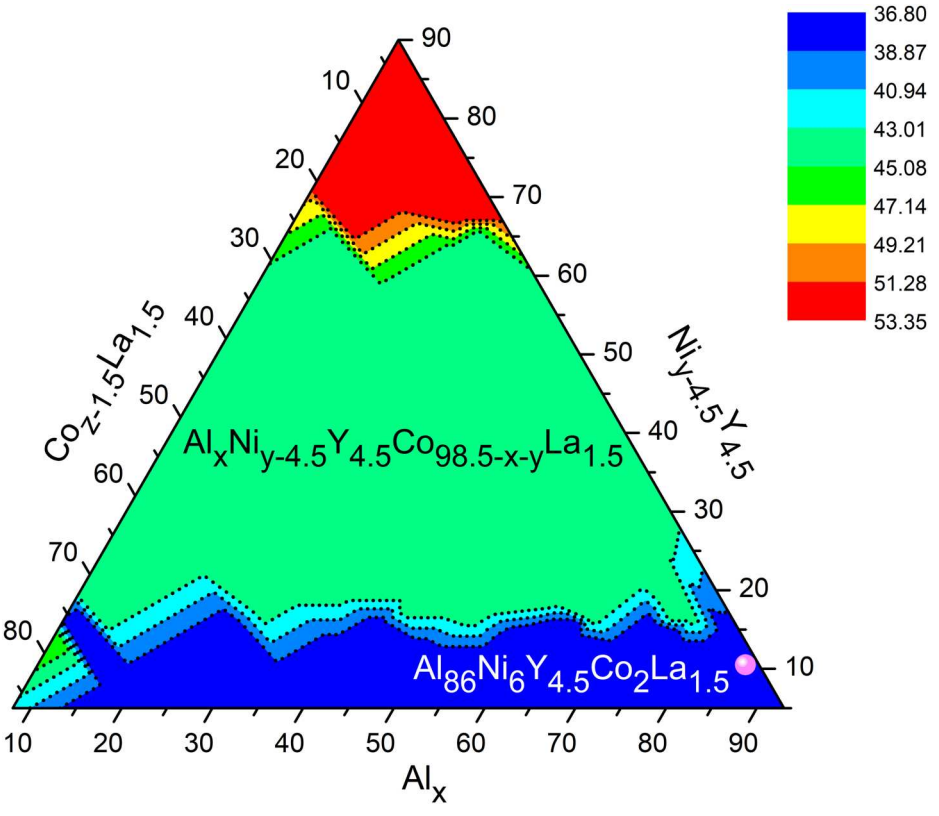

Figure 7. Composition maps of the predicted fracture toughness for the pseudo-ternary diagram of $Al_xNi_{y-4.5}Y_{4.5}Co_{98.5-x-y}La_{1.5}$ BMG predicted with the ETR model. The experimentally reported fracture toughness value for the $Al_{86}Ni_6Y_{4.5}Co_2La_{1.5}$ BMG is shown inside the composition maps.

Data curation. **M.S. Wang:** Methodology, Data Curation, Investigation. **L.M. Xu:** Methodology, Data Curation, Software.

Disclosure statement

No potential conflict of interest was reported by the author(s).

Funding

This work was supported by National Natural Science Foundation of China: [Grant Number 52001148]; Jiangxi Provincial Natural Science Foundation: [Grant Number 20232BAB214012]; Ganpo Promising Talents Supporting Plan: Talent Development Project of Leading Academic and Technological Researchers in Key Disciplines: [Grant Number 20232BCJ23099]; Provincial Science and Technology Program of Jiangxi Academy of Sciences: [Grant Number 2023YSBG21015 and 2023YSBG50009].

ORCID

Hui Guo http://orcid.org/0000-0001-9538-3312

References

[1] M.F. Ashby and A. Greer, *Metallic glasses as structural materials*. Scripta Mater 54 (2006), pp. 321–326.

[2] J. Xu, U. Ramamurty, and E. Ma, *The fracture toughness of bulk metallic glasses*. JOM 62 (2010), pp. 10–18.

[3] Y.T. Sun, H.Y. Bai, M.Z. Li, and W.H. Wang, *Machine learning approach for prediction and understanding of glass-forming ability*. J. Phys. Chem. Lett 8 (2017), pp. 3434–3439.

[4] J. Xiong, S.Q. Shi, and T.Y. Zhang, *A machine-learning approach to predicting and understanding the properties of amorphous metallic alloys*. Mater. Design 187 (2020), pp. 108378–108392.

[5] X.W. Liu, Z.L. Long, W. Zhang, and L.M. Yang, *Key feature space for predicting the glass-forming ability of amorphous alloys revealed by gradient boosted decision trees model*. J. Alloys Compd 901 (2022), pp. 163606–163612.

[6] G. Liu, S. Sohn, S.A. Kube, A. Raj, A. Mertz, A. Nawano, A. Gilbert, M.D. Shattuck, C.S. O'Hern, and J. Schroers, *Machine learning versus human learning in predicting glass-forming ability of metallic glasses*. Acta Mater. 243 (2023), pp. 118497–118507.

[7] X. Liu, Z. Long, L. Yang, W. Zhang, and Z. Li, *Prediction of glass forming ability in amorphous alloys based on different machine learning algorithms*. J. Non-Cryst. Solids 570 (2021), pp. 121000–121005.

[8] E.D. Cubuk, S.S. Schoenholz, J.M. Rieser, B.D. Malone, J. Rottler, D.J. Durian, E. Kaxiras, and A.J. Liu, *Identifying structural flow defects in disordered solids using machine-learning methods*. Phys. Rev. Lett 114 (2015), pp. 108001–108005.

[9] Y. Tang, Y. Wan, Z. Wang, C. Zhang, J. Han, C. Hu, and C. Tang, *Machine learning and Python assisted design and verification of Fe–based amorphous/nanocrystalline alloy*. Mater. Design 219 (2022), pp. 110726–110736.

[10] Z. Li, Z. Long, S. Lei, L. Yang, W. Zhang, and T. Zhang, *Explicit expressions of the saturation flux density and thermal stability in Fe-based metallic glasses based on Lasso regression*. Intermetallics 139 (2021), pp. 107361–107372.

[11] X. Li, G. Shan, and C.H. Shek, *Machine learning prediction of magnetic properties of Fe-based metallic glasses considering glass forming ability*. J. Mater. Sci. Technol 103 (2022), pp. 113–120.

[12] Y. Wang, Y. Tian, T. Kirk, O. Laris, J.H. Ross, R.D. Noebe, V. Keylin, and R. Arróyave, *Accelerated design of Fe-based soft magnetic materials using machine learning and stochastic optimization*. Acta Mater. 194 (2020), pp. 144–155.

[13] Z. Lu, X. Chen, X. Liu, D. Lin, Y. Wu, Y. Zhang, H. Wang, S. Jiang, H. Li, X. Wang, and Z. Lu, *Interpretable machine-learning strategy for soft-magnetic property and thermal stability in Fe-based metallic glasses*. NPJ Comput. Mater 6 (2020), pp. 187–195.

[14] N. Zhang, A. He, G. Zhang, P. Cai, B. Zhang, Y. Ling, Y. Dong, J. Li, Q. Man, and B. Shen, *Interpretable machine learning-assisted design of Fe-based nanocrystalline alloys with high saturation magnetic induction and low coercivity*. J. Mater. Sci. Technol 188 (2024), pp. 73–83.

[15] C. Liu, X. Wang, W. Cai, and H. Su, *Prediction of magnetocaloric properties of Fe-based amorphous alloys based on interpretable machine learning*. J. Non-Cryst. Solids 625 (2024), pp. 122749–122757.

[16] Y.X. Zhang, S.J. Xie, W. Guo, J. Ding, L.H. Poh, and Z.D. Sha, *Multi-objective optimization for high-performance Fe-based metallic glasses via machine learning approach*. J. Alloys Compd 960 (2023), pp. 170793–170803.

[17] C. Nam, *Convolutional neural network guided prediction of saturation magnetic flux density of Fe-based metallic glasses*. Comp. Mater. Sci 225 (2023), pp. 112198–112207.
[18] X. Li, G.C. Shan, H.B. Zhao, and C.H. Shek, *Domain knowledge aided machine learning method for properties prediction of soft magnetic metallic glasses*. T. Nonferr. Metal. Soc 33 (2023), pp. 209–219.
[19] J. Gao, J. Hou, Y. Wu, B. Ji, D. Wang, K. Qiu, J. You, and J. Wang, *Machine learning-enabled design of Fe-based bulk metallic glasses for superior thermal neutron absorption properties*. J. Alloys Compd 1010 (2025), pp. 177595–177604.
[20] Z. Li, Z. Long, S. Lei, and Y. Tang, *Machine learning driven rationally design of amorphous alloy with improved elastic models*. Mater. Design 220 (2022), pp. 110881–110892.
[21] X. Liu, Z. Long, and L. Peng, *Prediction of Vickers hardness of amorphous alloys based on interpretable machine learning*. J. Non-Cryst. Solids 602 (2023), pp. 122095–122103.
[22] L. Shao, J. Ketkaew, P. Gong, S. Zhao, S. Sohn, P. Bordeenithikasem, A. Datye, R.M.O. Mota, N. Liu, S.A. Kube, Y. Liu, W. Chen, K. Yao, S. Wu, and J. Schroers, *Effect of chemical composition on the fracture toughness of bulk metallic glasses*. Materialia 12 (2020), pp. 100828–100839.
[23] W. Chen, H.F. Zhou, Z. Liu, J. Ketkaew, L. Shao, N. Li, P. Gong, W. Samela, H.J. Gao, and J. Schroers, *Test sample geometry for fracture toughness measurements of bulk metallic glasses*. Acta Mater. 145 (2018), pp. 477–487.
[24] J.J. Lewandowski, W.H. Wang, and A.L. Greer, *Intrinsic plasticity or brittleness of metallic glasses*. Phil. Mag. Lett 85 (2005), pp. 77–87.
[25] J. Schroers and W.L. Johnson, *Ductile bulk metallic glass*. Phys. Rev. Lett 93 (2004), pp. 255506–255509.
[26] W. Chen, Z. Liu, J. Ketkaew, R.M.O. Mota, S. Kim, M. Power, W. Samela, and J. Schroers, *Flaw tolerance of metallic glasses*. Acta Mater. 107 (2016), pp. 220–228.
[27] C.P. Kim, J.Y. Suh, A. Wiest, M.L. Lind, R.D. Conner, and W.L. Johnson, *Fracture toughness study of new Zr-based Be-bearing bulk metallic glasses*. Scripta Mater 60 (2009), pp. 80–83.
[28] W. Chen, J. Ketkaew, Z. Liu, R.M.O. Mota, K. O'Brien, C.S. da Silva, and J. Schroers, *Does the fracture toughness of bulk metallic glasses scatter?* Scripta Mater 107 (2015), pp. 1–4.
[29] Y.S. Chang, K.T. Hsu, J.B. Li, P.H. Tsai, J.S.C. Jang, and J.C. Huang, *Effect of cast process and microalloying on the fracture toughness of Zr-based bulk amorphous alloys*. J. Alloys Compd 614 (2014), pp. 87–93.
[30] Q. He, Y.Q. Cheng, E. Ma, and J. Xu, *Locating bulk metallic glasses with high fracture toughness: chemical effects and composition optimization*. Acta Mater. 59 (2011), pp. 202–215.
[31] C.T. Liu, L. Heatherly, D.S. Easton, C.A. Carmichael, J.H. Schneibel, C.H. Chen, J.L. Wright, M.H. Yoo, J.A. Horton, and A. Inoue, *Test environments and mechanical properties of Zr-base bulk amorphous alloys*. Metall. Mater. Trans. A 29 (1998), pp. 1811–1820.
[32] J.H. Schneibel, J.A. Horton, and P.R. Munroe, *Fracture toughness, fracture morphology, and crack-tip plastic zone of a Zr-based bulk amorphous alloy*. Metall. Mater. Trans. A 32 (2001), pp. 2819–2825.
[33] A. Kawashima, H. Kurishita, H. Kimura, T. Zhang, and A. Inoue, *Fracture toughness of $Zr_{55}Al_{10}Ni_5Cu_{30}$ bulk metallic glass by 3-point bend testing*. Mater. Trans 46 (2005), pp. 1725–1732.
[34] J.J. Lewandowski, A.K. Thurston, and P. Lowhaphandu, *Fracture toughness of amorphous metals and composites*. Mater. Res. Soc. Symp. Proc 754 (2003), pp. 307–313.

[35] J.P. Best, H.E. Ostergaard, B. Li, M. Stolpe, F. Yang, K. Nomoto, M.T. Hasib, O. Muránsky, R. Busch, X. Li, and J.J. Kruzic, *Fracture and fatigue behaviour of a laser additive manufactured Zr-based bulk metallic glass*. Addit. Manuf 36 (2020), pp. 101416–101426.
[36] P. Zhang, C. Zhang, and L. Liu, *Toughening 3D-printed Zr-based bulk metallic glass via synergistic defects engineering*. Mater. Res. Lett 10 (2022), pp. 377–384.
[37] Q. He, J.K. Shang, E. Ma, and J. Xu, *Crack-resistance curve of a Zr–Ti–Cu–Al bulk metallic glass with extraordinary fracture toughness*. Acta Mater. 60 (2012), pp. 4940–4949.
[38] Y. Shen and J. Xu, *Improving plasticity and toughness of Cu-Zr-Y-Al bulk metallic glasses via compositional tuning towards the CuZr*. J. Mater. Res 25 (2009), pp. 375–382.
[39] L.M. Andersen, D.C. Hofmann, and K.S. Vecchio, *Effect of zirconium purity on the glass-forming-ability and notch toughness of $Cu_{43}Zr_{43}Al_7Be_7$*. Mat. Sci. Eng: A 674 (2016), pp. 397–405.
[40] P. Jia, Z.D. Zhu, E. Ma, and J. Xu, *Notch toughness of Cu-based bulk metallic glasses*. Scripta Mater 61 (2009), pp. 137–140.
[41] P. Wesseling, T.G. Nieh, W.H. Wang, and J.J. Lewandowski, *Preliminary assessment of flow, notch toughness, and high temperature behavior of $Cu_{60}Zr_{20}Hf_{10}Ti_{10}$ bulk metallic glass*. Scripta Mater 51 (2004), pp. 151–154.
[42] S.G. Wang, L.L. Shi, and J. Xu, *Mg-based bulk metallic glasses: elastic properties and their correlations with toughness and glass transition temperature*. J. Mater. Res 26 (2011), pp. 923–933.
[43] L.L. Shi and J. Xu, *Mg based bulk metallic glasses: glass transition temperature and elastic properties versus toughness*. J. Non-Cryst. Solids 357 (2011), pp. 2926–2933.
[44] Z.D. Zhu, P. Jia, and J. Xu, *Optimization for toughness in metalloid-free Ni-based bulk metallic glasses*. Scripta Mater 64 (2011), pp. 785–788.
[45] B. Li, L.M. Ruschel, K. Nomoto, O. Gross, B. Adam, N. Neuber, M. Frey, S.P. Ringer, B. Gludovatz, R. Busch, and J.J. Kruzic, *Fracture behavior of NiNb and NiNbP bulk metallic glasses*. J. Alloys Compd 1010 (2025), pp. 177369–177378.
[46] J. Zhou, Q. Wang, X. Hui, Q. Zeng, Y. Xiong, K. Yin, B. Sun, L. Sun, M. Stoica, W. Wang, and B. Shen, *A novel FeNi-based bulk metallic glass with high notch toughness over 70 MPa $m^{1/2}$ combined with excellent soft magnetic properties*. Mater. Design 191 (2020), pp. 108597–108605.
[47] C.H. Shek, G.M. Lin, K.L. Lee, and J.K.L. Lai, *Fractal fracture of amorphous $Fe_{46}Ni_{32}V_2Si_{14}B_6$ alloy*. J. Non-Cryst. Solids 224 (1998), pp. 244–248.
[48] A. Shamimi Nouri, X.J. Gu, S.J. Poon, G.J. Shiflet, and J.J. Lewandowski, *Chemistry (intrinsic) and inclusion (extrinsic) effects on the toughness and Weibull modulus of Fe-based bulk metallic glasses*. Phil. Mag. Lett 88 (2008), pp. 853–861.
[49] J.J. Lewandowski, X.J. Gu, A. Shamimi Nouri, S.J. Poon, and G.J. Shiflet, *Tough Fe-based bulk metallic glasses*. Appl. Phys. Lett 92 (2008), pp. 091918–091920.
[50] M.D. Demetriou, G. Kaltenboeck, J.Y. Suh, G. Garrett, M. Floyd, C. Crewdson, D.C. Hofmann, H. Kozachkov, A. Wiest, J.P. Schramm, and W.L. Johnson, *Glassy steel optimized for glass-forming ability and toughness*. Appl. Phys. Lett 95 (2009), pp. 041907–041909.
[51] S.F. Guo, K.C. Chan, and L. Liu, *Notch toughness of Fe-based bulk metallic glass and composites*. J. Alloys Compd 509 (2011), pp. 9441–9446.
[52] X.J. Gu, S.J. Poon, G.J. Shiflet, and J.J. Lewandowski, *Ductile-to-brittle transition in a Ti-based bulk metallic glass*. Scripta Mater 60 (2009), pp. 1027–1030.
[53] X.K. Xi, D.Q. Zhao, M.X. Pan, W.H. Wang, Y. Wu, and J.J. Lewandowski, *Fracture of brittle metallic glasses: brittleness or plasticity*. Phys. Rev. Lett 94 (2005), pp. 125510–125513.

[54] S.V. Madge, D.V. Louzguine-Luzgin, J.J. Lewandowski, and A.L. Greer, *Toughness, extrinsic effects and Poisson's ratio of bulk metallic glasses*. Acta Mater. 60 (2012), pp. 4800–4809.
[55] J. Benesty, J.D. Chen, Y.T. Huang, and I. Cohen, *Pearson correlation coeffcient, noise reduction in speech processing*, Springer, Berlin, Heidelberg, 2009.
[56] F. Pedregosa, G. Varoquaux, A. Gramfort, V. Michel, and B. Thirion, *Scikit-learn: machine learning in Python*. J. Mach. Learn. Res 12 (2011), pp. 2825–2830.
[57] H. Zou, *Comment: Ridge Regression—still inspiring after 50 years*. Technometrics. 62 (2020), pp. 456–458.
[58] M.A. Hearst, S.T. Dumais, E. Osuna, J. Platt, and B. Scholkopf, *Support vector machines*. IEEE Intell. Syst. Appl 13 (1998), pp. 18–28.
[59] Y. Zhang, G. Cao, B. Wang, and X. Li, *A novel ensemble method for k-nearest neighbor*. Pattern Recogn. 85 (2019), pp. 13–25.
[60] M. Xu, P. Watanachaturaporn, P.K. Varshney, and M.K. Arora, *Decision tree regression for soft classification of remote sensing data*. Remote Sens. Environ 97 (2005), pp. 322–336.
[61] P. Geurts, D. Ernst, and L. Wehenkel, *Extremely randomized trees*. Mach. Learn 63 (2006), pp. 3–42.
[62] L. Breiman, *Random forests*. Mach. Learn 45 (2001), pp. 5–32.
[63] D.P. Solomatine and D.L. Shrestha, *AdaBoost.RT: a boosting algorithm for regression problems*. Neural Netw. 2 (2004), pp. 1163–1168.
[64] J.O. Ogutu, T. Schulz-Streeck, and H.P. Piepho, *Genomic selection using regularized linear regression models ridge regression, lasso, elastic net and their extensions*. BMC Proc. 6 (2012), pp. S10–S15.
[65] J.O. Rawlings, S.G. Pantula, and D.A. Dickey, *Applied regression analysis a research tool*, Springer, New York, 1998.
[66] B.J. Yang, J.H. Yao, J. Zhang, H.W. Yang, J.Q. Wang, and E. Ma, *Al-rich bulk metallic glasses with plasticity and ultrahigh specific strength*. Scripta Mater 61 (2009), pp. 423–426.
[67] B.J. Yang, J.H. Yao, Y.S. Chao, J.Q. Wang, and E. Ma, *Developing aluminum-based bulk metallic glasses*. Philos. Mag 90 (2010), pp. 3215–3231.
[68] J.P. Liao, B.J. Yang, Y. Zhang, W.Y. Lu, X.J. Gu, and J.Q. Wang, *Evaluation of glass formation and critical casting diameter in Al-based metallic glasses*. Mater. Design 88 (2015), pp. 222–226.
[69] N.C. Wu, L. Zuo, J.Q. Wang, and E. Ma, *Designing aluminum-rich bulk metallic glasses via electronic-structure-guided microalloying*. Acta Mater. 108 (2016), pp. 143–151.
[70] H. Guo, C.B. Jiang, B.J. Yang, and J.Q. Wang, *On the fracture toughness of bulk metallic glasses under Berkovich nanoindentation*. J. Non-Cryst. Solids 481 (2018), pp. 321–328.

Taylor & Francis
Taylor & Francis Group

Philosophical Magazine

ISSN: 1478-6435 (Print) 1478-6443 (Online) Journal homepage: www.tandfonline.com/journals/tphm20

Phase diagram determination using machine learning methods in materials science and engineering: a review

Abhishek Kumar Thakur, Sanyam Nitin Totade, Krishna Muralidharan & Monojit Dutta

To cite this article: Abhishek Kumar Thakur, Sanyam Nitin Totade, Krishna Muralidharan & Monojit Dutta (2026) Phase diagram determination using machine learning methods in materials science and engineering: a review, Philosophical Magazine, 106:2, 180-204, DOI: 10.1080/14786435.2025.2558154

To link to this article: https://doi.org/10.1080/14786435.2025.2558154

PHILOSOPHICAL MAGAZINE
2026, VOL. 106, NO. 2, 180–204
https://doi.org/10.1080/14786435.2025.2558154

Taylor & Francis
Taylor & Francis Group

Phase diagram determination using machine learning methods in materials science and engineering: a review

Abhishek Kumar Thakur[a], Sanyam Nitin Totade[a], Krishna Muralidharan[b] and Monojit Dutta[a]

[a]Research and Development Division, Tata Steel Limited, Jamshedpur, India; [b]Department of Materials Science and Engineering, University of Arizona, Tucson, AZ, USA

ABSTRACT

Machine learning methods are widely applied in various areas of materials science and engineering. They prove to be a powerful framework for understanding structure–property relationships and aid in discovering novel materials. In this review, we address various machine learning approaches used to determine the phase diagram of different material systems. We provide a detailed discussion on data generation methods, preprocessing, and common data operations that are essential for model development. We examine unsupervised and supervised machine learning methods, along with their training, testing, and validation processes. Furthermore, we highlight the challenges in phase diagram calculation and propose potential solutions. Finally, we discuss the applications of different machine learning methods in constructing phase and transformation diagrams.

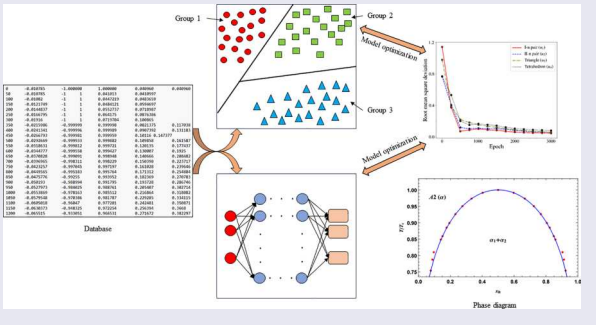

ARTICLE HISTORY
Received 9 May 2025
Accepted 1 September 2025

KEYWORDS
Neural networks; miscibility gap; thermodynamic models; first-principles calculations; phase boundaries; steel alloys

1. Introduction

Phase diagrams are central to alloy design and development. It is an important tool to study the stability and coexistence of different phases in a material system. It is helpful in understanding the phase transformation with respect to different thermodynamic variables such as temperature, pressure, and composition. Although phase diagrams do not provide information regarding materials kinetics, they serve as a guide for alloy design and development. Using phase diagrams, we can tune up to get the optimised

CONTACT Abhishek Kumar Thakur abhishek.thakur1@tatasteel.com Research and Development Division, Tata Steel Limited, Jamshedpur 831007, Jharkhand, India

state of an alloy having the desired microstructure and properties. Traditionally, phase diagrams are primarily constructed based on experiments. These experiments are reliable but are costly and time consuming. Experimentally, phase diagrams are constructed by preparing alloys of different compositions followed by heating them to different temperatures to achieve their equilibrium states. Once equilibrium is achieved, different phases present in the system are identified and consequently phase boundaries are drawn. Different techniques are utilised to draw phase diagrams such as metallography, x-ray diffraction (XRD), and thermal analysis [1].

Experimentally, it is cumbersome to cover all compositions, pressures, and temperatures for a binary system, and it becomes nearly impossible to do the same for ternary or other higher-order systems. Nevertheless, experimentally determined phase equilibria are important and provide valuable data that can further be used in computational modelling tools such as the CALculation of PHAse Diagram (CALPHAD) method [2]. Experimental data play a vital role in extrapolating a binary and ternary phase diagram to higher order systems using the CALPHAD method. Thus, this method provides a potential route for the phase diagram calculation of multi-component systems. It constructs thermodynamic models with adjustable parameters which can be optimised based on the available experimental data to obtain an accurate description of the system [3]. Further, the developed model can also be extrapolated to higher order systems [4]. However, one of the major shortcomings of this method is that it provides no information on metastable phases or any new phase which is yet to be discovered. First-principles calculations can aid in the exploration of new phases using the ground state total energy calculations [5,6]. This is helpful in calculating a robust phase diagram, but the first-principles calculations are mainly restricted to 0 K. Furthermore, the computational burden increases significantly with system size, and the challenges in determining high temperature phase equilibria severely limit this approach and its applications to multi-component systems.

Data-driven machine learning methods provide a viable solution for constructing phase diagrams and help in accelerating phase diagram calculations for multi-component systems. It is considered a paradigm for guiding the ideology of materials science [7]. Machine learning methods have found their applications in various sectors of engineering and technology [8–12]. One of the primary benefits of machine learning methods is their low computational cost. Further, it rapidly accelerates the development process and provides a powerful tool in materials exploration. Using machine learning algorithms, the underlying thermodynamics of a material system can be studied based on local spatial composition descriptors and phase distribution data [13,14]. It has been successfully applied to study amorphous and disordered materials [15], polymers [16], ferroelectric systems [17], as well as to infer thermodynamic state functions of materials [18], among other applications. Moreover, the development of novel simulation techniques and increasing computational power generates a tremendous amount of data. This vast collection of data supports data-driven machine learning methods, which can be used to extract underlying patterns and knowledge.

In this article, we summarise the application of various machine learning algorithms to the calculation of phase diagrams and related predictions for different material systems. Database generation, preprocessing of data, data normalisation, and data visualisation methods are presented in section 2. Next, in section 3, two major categories of

machine learning methods viz., unsupervised, and supervised learning along with different activation functions and loss calculation methods are discussed. In section 4, we highlight some common challenges in calculating phase diagrams using machine learning models and their solutions. In section 5, we discuss the applications of machine learning methods in predicting phase diagrams for various material systems. Finally, we discuss future perspective and highlight potential areas and probable methods for improving machine learning models.

2. Database

A machine learning model is essentially a data-driven process. It learns, tunes its parameters, makes predictions, and makes decisions based on the data provided by the user. So, data clearly play a central role in machine learning algorithm design, working, and its performance. Thus, a database should be created and prepared before implementing a machine learning model. The created database should be scrutinised for missing values, wrong values, unrealistic values, and noises. The following sections highlight a few major available databases, their generation and preprocessing methods, followed by data visualisation.

2.1. Database generation

There are several ways to generate data and establish a database. For example, data can be generated by experiments and simulations. Various databases are also available in the materials science community, such as SGTE [19], JANAF [20], LIPIDAT [21], The Materials Project [22], OQMD [23,24], Aflow [25], and the American Minerologist database [26], among others. A database can also be compiled by collecting relevant objective data from the available literature sources. For instance, to understand the phase diagram of a system, the thermodynamic data relevant to phase diagram such as temperature, composition, enthalpy of mixing, and pressure can be either generated or collected from literature. The data can be generated using various tools depending on the objective such as for the previous case, we can use computational methods such as the regular solution model, cluster variation method, first-principles calculations, molecular dynamics simulations, as well as experimental tools such as differential scanning calorimetry, x-ray diffraction, and transmission electron microscopy. Similarly, to understand transport phenomena in materials systems using machine learning, data relevant to transport in materials such as self and inter diffusion coefficients at different temperatures, thermal conductivity, and the volume fractions of different phases present in the system should be compiled into a database. Figure 1 shows a sample flowchart, that presents various ways to compile data for a database used in machine learning models.

2.2. Data preprocessing

Once the data has been generated, it is important to process it before moving forward to the next step in building a machine learning model. The generated dataset should be checked for erroneous, unrealistic, and irrelevant data points that may result from errors in experiments, computational models, or data extraction from the literature

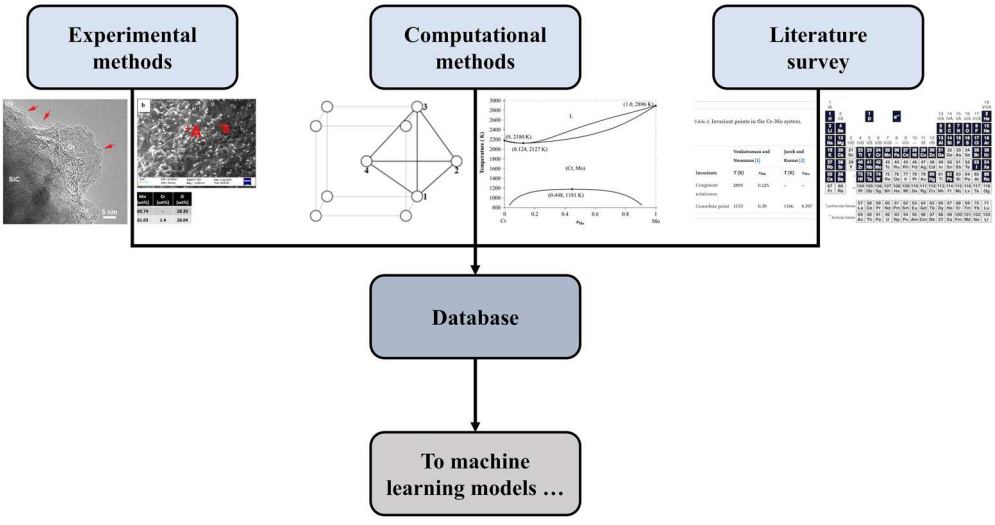

Figure 1. Different sources for database creation viz., experimental methods (figures adapted from [27,28]), computational methods (figures adapted from [29,30]), and literature surveys (figures adapted from [20,30]).

[31,32]. It should also be thoroughly checked for missing data, as wherever possible, relevant data should be added or the missing entries removed, since missing values can cause inconsistencies in the dataset.

The data collected from various sources may contain unrealistic or irrelevant values due to errors during the data collection process. There are many ways in which unrealistic or irrelevant data can enter a dataset. Some possible reasons include errors during the experimental setup, accidental changes to parameters in computational models, or the collection of incorrect or irrelevant information from the literature. For example, simply changing the cooling rate of a high temperature austenitic steel can result in end products such as pearlite, bainite, or martensite. Another example is that, for mechanically unstable phases, it is common practice to extrapolate free energies from stable region into unstable regions. However, extrapolations from different systems that share a common phase may be inconsistent, and the resulting free energies may unintentionally fall below those of truly stable phases. These types of changes or extrapolations can lead to data that may be irrelevant to the machine learning model. On the other hand, there may be multiple instances where one can have missing data in the database. This can again cause inconsistencies in the database and can affect the efficiency of the machine learning model. Sources of missing data can include experiments where a low temperature alloy of a system takes a long time to attain equilibrium [33,34], or where metastable phases form [35–37] that the user chooses to exclude from the machine learning model. Furthermore, if the computational method for data generation fails at any instance, then it will also lead to missing data. In any of these situations, a void will be created in the database that should be addressed. Now, these missing values can be filled using data obtained from a relevant computational model if the data are generated by an experimental method, and vice-versa. On the other hand, if the database is created using literature data, one can fill in the missing values by complementing it with

experiments or computational models. Lastly, if the missing values cannot be filled, it is recommended to remove that data from the database.

In some cases where only limited data is present, data augmentation can be performed. Data augmentation is beneficial in increasing the size and diversity of a database [38]. This can be performed by applying various transformation techniques, such as rotation, translation, feature engineering, and interpolation, to the database. After addressing the missing and incorrect values in a database, data normalisation is commonly practiced when building a machine learning model. The basic idea behind data normalisation is to eliminate the dominance of certain highly positive or highly negative data present in the database. Data normalisation standardises the database by transforming all data within a defined range. The data normalisation range is determined by the model developer and is generally [0, 1] or [−1, 1].

2.3. Data visualisation

Data visualisation plays an important role in understanding a database. It provides insights into our data distribution, its range, and the associations among the variables. There are several data visualisation methods available in different packages. One of the basic tools to visualise data is the histogram. It simply provides one with the number of different classes of data available in the underlying database. Another method to visualise data is by using a cluster plot in which different classes consolidate in separate groups. The clustering of data is based on different features present in the dataset. For example, Figure 2 shows two different clusters created using cluster plot based on a steel database. It clearly distinguishes between hypoeutectoid and hypereutectoid steel

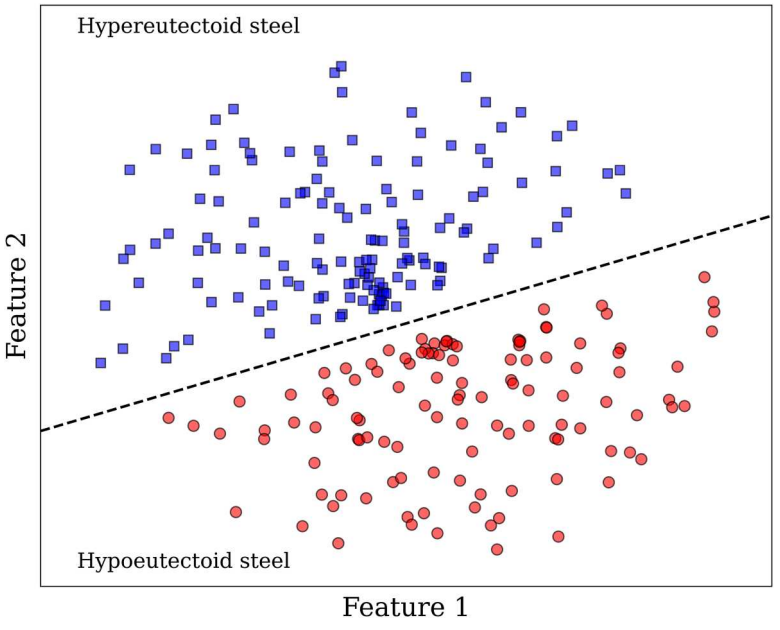

Figure 2. Samples of steel are separated into two clusters: hypoeutectoid and hypereutectoid steel, based on two features.

based on feature 1 and feature 2. The features that identify a steel sample can include its elemental compositions, processing conditions, etc. There are other methods of clustering, such as density-based clustering, centroid-based clustering, connectivity-based clustering, and distribution-based clustering [39, 40]. A dendrogram is another data visualisation technique that represents the hierarchical clustering present among the data in a database. It is based on the concept that similar data points are close to each other in terms of distance, while dissimilar data points are far away. A dendrogram is used to present data in a tree-like branching format for different non-metallic inclusions (NMIs) present in four different grades of steel [41]. This analysis can have major industrial applications, as it can be used to identify the parent NMI complex that can give rise to a target NMI.

The Pearson correlation matrix (or heatmap) and pair plot are other powerful methods for data visualisation. The Pearson correlation matrix is always a square matrix and consists of the correlations between different pairs of variables present in the database. The diagonal term represents the correlation between the same variable, and thus it is equal to unity. However, the off-diagonal terms represent correlation between different pairs of variables. The correlation coefficients between different pairs of variables in the upper diagonal terms are basically the same as those in the lower diagonal terms and thus, a Pearson correlation matrix is symmetrical. Among two variables, a positive correlation means that one variable is positively affected by an increase in the second variable and vice versa. Conversely, a negative correlation between a pair of variables means that one variable will be negatively impacted by an increase in the second variable and vice versa. This feature is highly beneficial in the field of materials science and engineering, as researchers often have to deal with several parameters simultaneously. Like the Pearson correlation matrix, the pair plot is another data visualisation tool. It simplifies data visualisation and helps users decide on future processing steps by observing data correlations. The diagonal items in a pair plot show the distribution of a single variable while the off-diagonal items show the relationship between different pairs of variables present in the database. Like the Pearson correlation matrix, the items above the diagonal are symmetric to the items below the diagonal. The common data operations are compiled and displayed in Figure 3.

3. Machine learning methods

In this section, we will discuss two major machine learning methods viz., unsupervised and supervised. Both unsupervised and supervised machine learning models are used in phase diagram prediction. We focus on the training, testing, and validation of machine learning models, especially artificial neural networks. The importance of loss functions and their selection criteria, based on the type of dataset, is also highlighted.

3.1. Unsupervised methods

Unsupervised machine learning methods refer to those methods in which the data is not labelled. In other words, the output is not specified, and the algorithm finds correlations by analyzing the input data itself. These methods relate various data points based on their similarity, which is sometimes measured as the distance between them. Unsupervised

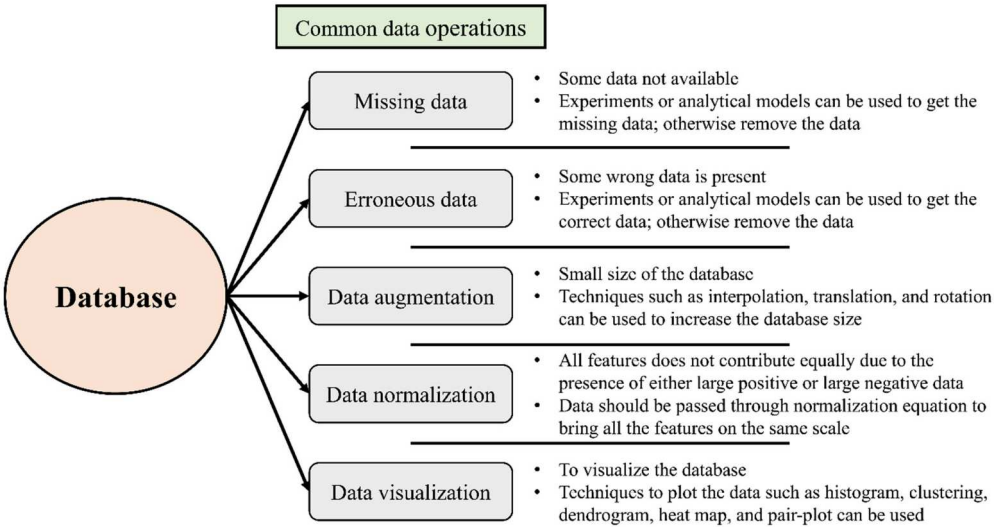

Figure 3. The image illustrates the common data operations performed on the database while building a machine learning model.

machine learning models, such as k-means clustering, hierarchical clustering, principal component analysis, support vector machines, decision tree, and random forests, are powerful in pattern recognition and grouping. Clustering is one of the most widely used unsupervised machine learning methods that classifies input data that are closely related. It provides insights into an unlabelled dataset based on the data itself and groups it into separate clusters. For instance, Figure 2 shows two clusters for the classification of hypoeutectoid and hypereutectoid steel based on the unlabelled input data itself. One of the advantages of clustering analysis is the anomaly detection in which outliers can be detected. For example, it can help monitor the phase boundary separating two phases in a phase diagram [42].

However, it has been observed that in some cases the feature space of the input data becomes too large. In such cases it becomes cumbersome to comprehend and visualise the input data. Thus, we aim to reduce the feature space and hence, dimensionality reduction becomes important. It is very important to safeguard the information contained in the input data itself, and thus a good dimensionality reduction method is one that preserves the largest data correlation. There are several methods for dimensionality reduction, such as principal component analysis (PCA), linear discriminant analysis (LDA), quadratic discriminant analysis (QDA), and singular value decomposition (SVD). PCA is one of the most common dimensionality reduction methods used, which transforms the N-dimensional input vectors into n-linear combinations that hold the maximum variability present in a dataset [43]. PCA finds applications in a large variety of materials system that include, but are not limited to, predicting the shear strength of steel fibre reinforced concrete beams [44], corrosion in mild steel plates [45], and damage identification in steel truss railroad bridges [46]. On the other hand, generative models are another class of unsupervised machine learning methods that can generate new data points by learning from the input dataset. The generative

models generate new data with a distribution similar to that of the original dataset. Variational autoencoders (VAEs) and generative adversarial networks (GANs) are two of the most commonly used generative models in the unsupervised machine learning framework.

3.2. Supervised methods

Unlike unsupervised methods, supervised machine learning methods have labelled databases i.e. each set of input data has a corresponding target value or a set of target values. There are a number of supervised methods available, such as linear regression, Gaussian Naïve Bayes, decision trees, random forests, and artificial neural networks [47]. Supervised machine learning algorithms have tremendous applications in materials science and engineering. They are used in multiple areas, including phase identification from x-ray diffraction spectra [48], alloy selection for the design of medical materials [49], prediction of elastic constants of multi-component alloys [50], and structure prediction of multi-principal element alloys [51]. Supervised machine learning methods can be seen as a fitting algorithm that map input data to its corresponding output data using a high dimensional function. Figure 4 shows the architecture of a supervised neural network model with n input and m output nodes at the input and output layer respectively. The data from the input nodes are passed to the nodes of hidden layers and then finally to the output nodes. It can be used for both regression and classification tasks.

Apart from the unsupervised and supervised learning methods, semi-supervised and reinforcement learning methods are also practiced widely. In the semi-supervised method, both labelled and unlabelled data are used for training [52]. The model relies on labelled data to identify existing patterns and correlations in unlabelled data to increase the model's efficiency. On the other hand, in reinforcement learning, the model learns from its environment and the feedback received based on its actions

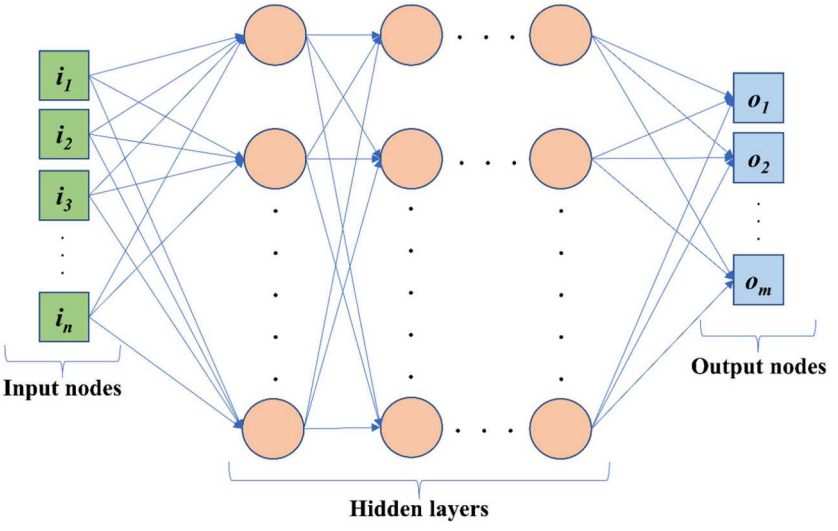

Figure 4. An artificial neural network architecture with n inputs and m output nodes.

[53]. In this case, the model essentially learns through trial and error in order to improve its performance. For every successful learning attempt, the model is rewarded, while for every unsuccessful learning attempt, the model is penalised. The reinforcement learning method is a good choice when the model has to explore and learn from its environment.

3.3. Training, testing and validation

After database preparation and preprocessing, a machine learning model is selected for training, testing, and validation. For each of these, a separate database is created, which is generally partitioned by random shuffling the data from the original database. The data in each set is passed in batches to the machine learning model. Though the process is simple, there are certain things that need to be taken care of during this process. In some machine learning models, especially neural networks, activation functions are generally applied to the data. The main objective of the activation function is to introduce non-linearity, which allows the model to identify and learn complex correlation that exists in the data. It is also used to match the data range of the target variables. There are several activation functions, such as rectified linear unit (ReLU), exponential linear unit (ELU), and hyperbolic tangent (tanh), already available in different machine learning packages [54,55].

For training, testing, and validation, a loss function is used to quantitatively measure the efficiency of a machine learning model. In other words, loss is a measure of the performance of a machine learning model. A high loss indicates that the predicted value from the trained model is very different from the corresponding actual value, and vice versa. On the other hand, any machine learning model is essentially a data-driven algorithm that aims for generalisation, and therefore, we can expect some loss even in a well-trained model. The loss functions can also be defined differently for continuous and categorical datasets. To model a dataset with numerical values, regression algorithms are generally used. Thus, in such cases, metrics like the mean absolute error (also known as the L1 loss), the mean squared error (also known as the L2 loss), the root mean squared error, and the mean bias error are used to quantify the performance of the model. Unlike regression, the loss of a model with a categorical dataset can be quantified by predicting the correct class. One such method is cross-entropy loss, also known as the negative log likelihood. As the predicted label or class from the neural network converges towards the actual label or class, the cross-entropy loss decreases and vice versa. Similarly, another loss function used in classification tasks is hinge loss. It is generally employed in the support vector machine models for maximum-margin classification [56].

4. Phase diagram calculation: challenges and solutions

Traditionally, phase diagrams have been determined using experimental techniques, which is laborious, time consuming, and expensive. Computational methods such as DFT and MD can be combined with thermodynamic models such as CALPHAD to complement and accelerate the calculation of phase diagrams. However, these methods are constrained by certain limitations, for instance, both DFT and MD become computationally expensive as the system size increases. Efforts have been

made in the development of other computational tools, such as the cluster expansion method [57] and special quasirandom structures [58], which are used to effectively capture the essential physics and thermodynamics while keeping the system size manageable. On the other hand, machine learning methods provide an alternative way to accelerate phase diagram calculation. These methods provide an elegant way to map the available material information, experimental as well as computational, to its phase boundaries.

Unlike other computational methods, any type of material relevant data, such as yield strength, ductility, phase type, temperature, composition, pressure, enthalpy, entropy, Gibbs energy, and invariant point information, can be used in machine learning models for phase diagram prediction. This provides more flexibility than traditional computational methods, as machine learning methods are not constrained by model specific parameters. However, the input data or features must be chosen carefully i.e. those features should be chosen which influence phase stability, and hence the phase diagram. The selection of irrelevant features will result in the model's inability to capture the true underlying phenomena between the input and output. This will result in poor performance and unreliable predictions from the model [59,60].

Another challenge in predicting phase diagrams with machine learning methods is the lack of a significant number of relevant, high-quality data points. Since machine learning methods are data-driven, the availability of sufficient high quality data is crucial for optimal model performance. As explained, data can be collected from literature, experimental sources, and computational resources. However, as the materials and thermodynamic complexity of the system increases, the data become scarcer. In such cases, training a machine learning model will lead to overfitting [61]. It is one of the common situations in which machine learning models, with a small dataset, try to map each set of input data to its corresponding set of output data during training. However, with a low number of data points, the training data are mapped accurately, but the model's performance on the test dataset is poor. Thus, the model loses its ability to generalise, as reflected in poor predictions on the test dataset. In other words, overfitting can be understood as a situation in which the model is not able to capture the underlying physics or patterns contained in the dataset. Overfitting can also occur as a result of using overly complex models with a large number of parameters or training the model for an unreasonably large number of epochs. Since overfitted machine learning models lose their generalisation capability, they can lead to inaccurate predictions of phase boundaries when used outside the training domain. One way to deal with overfitting is to add more data points to the training dataset. However, in some cases, producing more data is not easy, especially when using experiments. Another potential way to deal with overfitting is the k-fold cross validation method [62]. In this method, the training and test sets are created by iterating over the initial dataset, using different chunks for training and test purposes.

Data augmentation is another method that is beneficial when the size of database is small. A low data situation can arise in several conditions where the system under consideration is not thoroughly explored using experimental and computational methods. There is always a possibility of conducting relevant experiments or building computational models to generate more data and enrich the database. However, as explained

above, generating data can be difficult in some cases, and thus one is left with only a limited amount of data. In such situations, data augmentation plays a vital role in generating relevant data for machine learning models. Data augmentation essentially performs oversampling and artificially inflates the existing dataset by generating more data based on the insights learned from that dataset [38]. Data augmentation is most commonly used in convolution neural networks and image processing techniques when there is a limited number of images [63–67]. It can also be applied to other type of datasets, such as numerical and categorical datasets, by analyzing normal trends in the data and generating more data that follow similar trends [68–70]. A thorough discussion of different data augmentation methods for image data has been conducted by Shorten & Khoshgoftaar et al. (2019) [71]. A simple method for augmenting numerical or categorical datasets is to perform interpolation or extrapolation. This can be achieved by first building a mathematical model, such as a regression model, and then generating data at the required points. Synthetic minority over-sampling technique (SMOTE) is yet another over-sampling technique used to generate data for classes with fewer corresponding data points compared to other classes [72]. While interpolating data within the domain of the original dataset can be sensible and useful, extrapolating data outside that domain may not capture the trend and can lead to erroneous or unrealistic results. Thus, the data generated through these methods should always be checked to maintain inherent consistency with the original dataset. A simple flowchart illustrating the problem of overfitting and the small size of the database, along with their probable solutions for determining phase diagrams using machine learning methods, is shown in Figure 5.

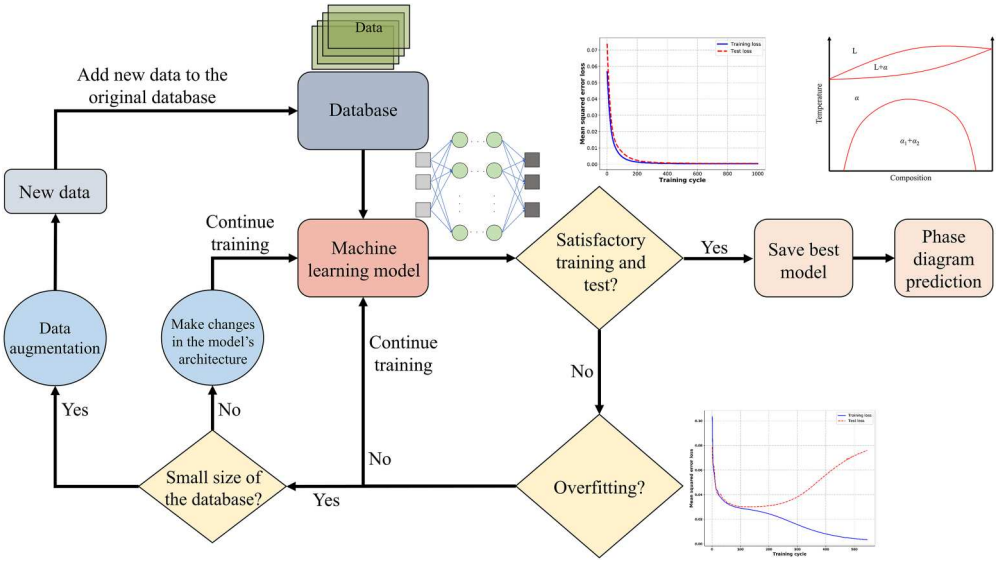

Figure 5. A flowchart illustrating the phase diagram prediction process using machine learning when size of the database is small, and it is difficult to generate more data using experimental or computational methods.

5. Application in phase diagram calculation

Recently, machine learning methods have been used in different areas of materials science and engineering to solve a wide range of problems. The basis of determining equilibrium phase diagrams using machine learning is to identify the correct stable phases as a function of various thermodynamic variables. A reasonable amount of work has been done to predict the equilibrium phase diagram of various material systems. Additionally, several studies have been conducted to predict transformation diagrams, such as the TTT and CCT diagrams, using machine learning models. Table 1

Table 1. Summary of various works predicting phase diagrams in metallurgical and materials science and engineering.

Work	Material system	Machine learning model used	Reference
Construction of ternary phase diagrams using uncertainty sampling in active learning, with space reduction based on Gibbs phase rule	Cr-Co-Ni; Co-Cr-Mn; Fe-Co-Cr; Cr-Mn-Ni	Semi-supervised: Label propagation or label spreading	[73]
Construction of a ternary phase diagram using uncertainty sampling to suggest the next experimental condition	Cu-Mg-Zn	Semi-supervised: Label propagation or label spreading	[74]
Construction of phase diagrams for chemically relevant species	Ag/Si; KNO_3/$LiNO_3$; K_2SO_4/Li_2SO_4; Hooke atoms; Helium dimers	Semi-supervised: Uncertainty sampling; Random forests	[42]
Calculation of the pressure-temperature phase diagram of uranium under extreme conditions	Uranium	Linear regression combined with regularisation	[75]
Construction of Pourbaix diagrams for IrO_2(110) and MoS_2 surfaces	IrO_2; MoS_2	Gaussian process regression	[76]
Construction of the MgO-CaO eutectic phase diagram	MgO-CaO	Machine learning interatomic potential constructed using SIMPLE-NN package	[77]
Construction of the phase diagram of Ag-Pd alloys	Ag-Pd	Two machine-learning interatomic potentials viz., Moment Tensor Potential and Gaussian Approximation Potential	[78]
Construction of the phase diagram of a BCC system exhibiting a miscibility gap boundary	A prototype BCC system	Supervised neural network model	[29]
Prediction of phase diagrams using composition, temperature, and pressure data	Inorganic compounds available in the NIST and ICSD databases	Random forest and Generative Autoencoders	[79]
Construction of a TTT diagram for high silicon steels	High silicon steels with varying compositions of other elements	Artificial Neural Network	[80]
Prediction of the TTT diagram for cold working tool steels	Cold working tool steels; Viking steels	Support Vector Machines	[81]
Prediction of the TTT diagrams for carbon and low-alloy steels	Carbon and low-alloy steel	Artificial Neural Network; LibSVM; K-nearest neighbour; Bagging; and Random Tree	[82]
Prediction of the TTT diagrams for high-alloy steels	3Cr2W8 V, Cr12, W12Cr4V2, W18Cr4V2Co5, and 5Cr4W2Mo2VS	A combination of filtered classifiers and regression models viz., random tree, random forest, bagging, K-nearest neighbour, and random committee	[83]
Prediction of the CCT diagrams of tool steels	Tool steels	Multilayered perceptron, k-Nearest Neighbours, Bagging, and Random Forest	[84]

summarises various works in the field of metallurgical and materials science and engineering aimed at predicting phase diagrams using different machine learning methods. In this section, we discuss several applications of machine learning methods in materials science and engineering. We present various works that potentially enlist the application of machine learning methods in phase diagram calculations.

5.1. Mapping uncertainty

In this method, machine learning algorithms are used to make predictions on the next configuration of a system that is to be considered for enhanced process optimisation. For example, by using uncertainty sampling, Terayama et al. (2022) [73] proposed that subsequent data points be synthesised or measured to construct a phase diagram. Similarly, Tamura et al. (2022) [74] suggested the most uncertain point in the phase diagram as the next experimental condition. These uncertainty mapping methods help greatly reduce the time needed to study a system and to construct the underlying phase diagram. Thus, instead of sampling or calculating all the points, i.e. instead of performing calculations for all the similar configurations of a system, the uncertainty algorithm provides the most probable points to consider. It has been successfully applied to calculate the isothermal sections of ternary systems such as Cr-Co-Ni, Co-Cr-Mn, Fe-Co-Cr, and Cr-Mn-Ni. Further, using uncertainty sampling, eutectic points can be characterised, and magnetic phase diagrams can also be studied. For example, when using uncertainty mapping, it is observed that the concentration of sampling points is dense near the eutectic and phase transition points compared to other regions of the phase diagram [42]. This provides a crucial idea about an invariant reaction taking place in a particular section of a phase diagram. Furthermore, anomaly detection is used to predict a possible phase transitions in a system and to identify different phases using unsupervised machine learning algorithms [85]. With potential applications in the steel industry, anomaly detection algorithms can be used to identify defects and possible phase transformations during a heat treatment cycle [86]. This anomaly detection algorithm can provide an industry with an additional tool for quality control, thereby helping to improve the product.

5.2. Integrating computational methods with machine learning algorithms

Several computational methods, such as first-principles calculations, molecular dynamics, and thermodynamic models such as the regular solution model, are integrated with machine learning algorithms to build a robust framework for the calculation of phase diagrams. These efficiently trained neural network models can provide accuracy that is comparable to ab-initio methods [87]. Moreover, the trained neural network models can help extrapolate the existing phase diagram to explore the stability and occurrence of various phases as a function of different thermodynamic parameters. For example, the pressure-temperature phase diagram for uranium and its phase boundary extrapolation are constructed using a machine-learned force field [75]. The machine-learned force field is trained on the energies and forces obtained from the density functional theory (DFT) calculations. Further developments have been made so that even a small sized database can be used to train neural network models for phase diagram calculations. For example, a Pourbaix diagram has been constructed for the IrO_2 (110)

surface using a Gaussian process regression model with just 20 electronic structure relaxations [76]. Attempts have also been made to explore metastable phases by integrating atomistic simulations with machine learning models [88].

The cluster variation method provides an accurate thermodynamic description by considering the short range order (SRO) present in a system [57]. This is performed using the equilibrium values of correlation functions obtained by minimising the energy of the system through numerical methods. However, it is computationally demanding and, in some cases, sensitive to the initial values of the correlation functions used. Thus, a machine learning model can be trained to predict the correlation functions generated using the cluster variation method up to a given maximal cluster approximation. Furthermore, using the predicted values from the trained model, the miscibility gap boundary of a prototype binary BCC system (composed of components A and B) can be illustrated, as shown in Figure 6 [29]. The phase diagram shows the variation of temperature (T) up to the consolute point temperature (T_c) as a function of composition (x_B). The machine learning predicted miscibility gap boundary (red dots) matches closely with the miscibility gap boundary calculated using the cluster variation method (solid blue line). The neural network model provides a significant advantage in this case, as the trained model can also be applied to similar BCC systems, thereby speeding up the entire phase diagram determination process. This is again beneficial from an industrial point of view, in which the final product is a function of several parameters. For example, Cr is an important element for the production of stainless steels. The Fe-Cr system consists of a miscibility gap and the presence of a σ phase. This machine learning algorithm can be used on the Fe-Cr system to further explore the miscibility gap boundary and the stability of the σ phase as a function of other plant parameters and processing conditions.

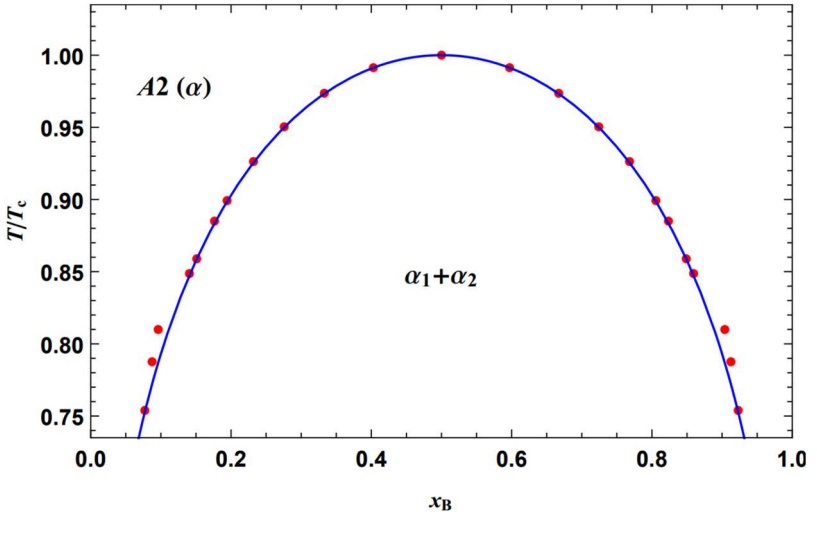

Figure 6. The miscibility gap boundary of a prototype BCC system is calculated using a trained supervised neural network model (red dots) and the cluster variation method (solid blue line) under the tetrahedron approximation. (Adapted from [29]).

5.3. Machine learning interatomic potentials

Machine learned interatomic potentials have proved to be a viable tool for phase diagram calculation. There has been a drastic increase in the construction of machine-learned interatomic potentials for a wide range of applications in materials science and engineering. A number of frameworks, such as SIMPLE-NN [89], Amp (Atomistic machine learning package) [90], N_2P_2 (Neural network potential package) [91], MAISE (Module for ab-initio structure evolution) [92], and Aenet (Atomic energy network) [15,93,94] are readily available to construct machine learning based interatomic potentials. Machine learning models provide an efficient route to map high dimensional potential energy surfaces and to predict them for a system's required configuration. It utilises high dimensional mathematical regression to interpolate between reference energies. In general, training machine learning interatomic potentials uses system information in terms of the atomic coordinates of all the atoms. The coordinates of each atom are transferred to a set of symmetry functions that are used in machine learning models [95]. Rosenbrock et al. (2021) have used machine learning potentials to describe the energy of alloy configurations for the Ag-Pd system over a wide range of compositions [78]. Ternary carbides such as the HfTaC, HfZrC, and TaTiC systems are also modelled using machine learning interatomic potentials to produce accurate convex hulls [96].

Several efforts have been made to construct phase diagrams using machine-learned interatomic potentials. Lee et al. (2022) have constructed the MgO-CaO eutectic phase diagram using a neural network interatomic potential trained via the SIMPLE-NN package [77]. The neural network is trained on data generated using two functionals viz., PBE (Perdew–Burke–Ernzerhof) and SCAN (Strongly Constrained and Appropriately Normed). The trajectories of solid and liquid phases at various compositions, calculated using DFT, are used to train the neural network potential. To include temperature effects, molecular dynamics simulations were carried out using constant pressure and constant volume ensembles, where temperature was modulated using thermostats. The trained neural network potential successfully characterises the eutectic composition and solid solubility limits, along with the topology of the phase diagram. Similarly, machine learned interatomic potentials have been used to construct a structural phase diagram for $In_xGa_{1-x}N$ alloys [87]. This drastically speeds up the phase diagram calculation with good transferability as compared to traditional methods. Additionally, a machine-learned interatomic potential has been developed for molecular hydrogen, which is used to construct its temperature-pressure phase diagram [97]. This is beneficial in the HIsarna process for next generation iron and steel making process with a focus on minimising carbon dioxide emissions [98].

On the other hand, universal machine learning interatomic potentials have also been developed, which can be used to accelerate phase diagram calculation. These potentials are pretrained on large and diverse datasets and allows transferability across different systems without retraining. Zhu et al. (2025) [99] demonstrate that universal machine learning interatomic potentials integrated into the Alloy Theoretic Automated Toolkit (ATAT) [6] programme enable rapid exploration of phase diagrams. This method speeds up the process by three orders of magnitude compared to DFT. Furthermore, Vazquez et al. (2024) [100] have used universal machine learning interatomic potentials to predict the volume and energy of the final structure for a relaxation run. This method

significantly reduces the computational cost associated with the calculation of fitting parameters.

5.4. Prediction of phase and transformation behaviour

As explained in section 2.1, there are several materials related databases readily available for use. These databases are created through rigorous experiments and simulations and are updated regularly. They contain materials specific information such as Gibbs energy, formation enthalpy, band structures, and other elastic and thermal properties of materials. Recently, these databases have been used to train machine learning models to predict various properties and identify novel structures. They are useful from the perspective of alloy design and development, as well as for achieving the required properties in a system.

MatLearn is one such web-based machine learning platform trained on DFT data [101]. It predicts formation energies at different compositions of a binary or ternary system. Figure 7 shows the variation of predicted formation energy at different compositions in a Cr-Fe binary alloy system, with a mean absolute error of 0.0761 eV/atom. This helps in exploring the compositional space of binary and ternary systems in the search of novel compounds. In another study, the machine learning model, after training on data from various sources, is able to predict the state of a system for a given composition, temperature, and pressure [79].

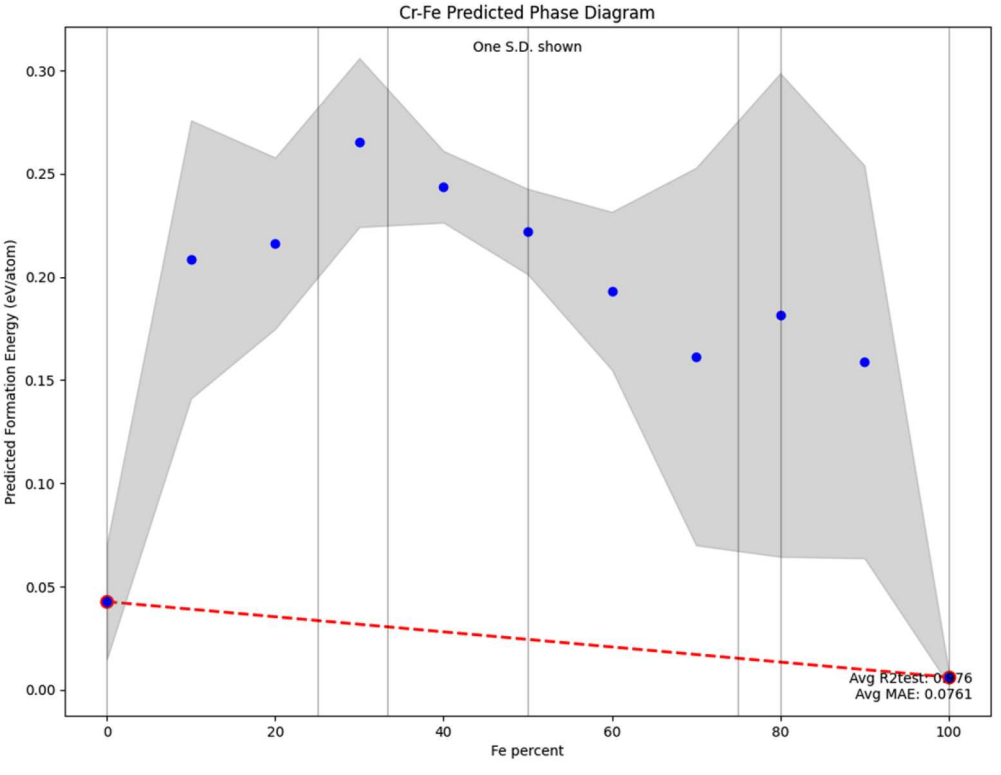

Figure 7. Cr-Fe phase diagram predicted using MatLearn.

The time-temperature-transformation curve, also known as the TTT curve, is an important tool in the steel industry. It is a plot of temperature against time that provides information about the transformation of different phases present in steel. However, since steel alloys are cooled continuously from their processing temperature to the working temperature, a continuous-cooling-transformation (CCT) curve is more beneficial in industry. However, both curves play a crucial role in designing proper heat treatment cycles for different steels. They also helps in achieving the desired phase and microstructure of steel. Predicting these diagrams for different steel systems is important and beneficial for tailoring the final product. Efforts have been made to predict the TTT diagram using a machine learning model, and the trained model is used to achieve an ultrafine bainitic microstructure in steel [80]. In another study, several TTT diagrams has been compiled and digitised to obtained the temperature, time, and phase transformation data to train a support vector machine (SVM) model [81]. This trained model is then used to predict the TTT diagram of tool steels with an accuracy of above 90%. Similarly, Huang et al., (2023) [82] have predicted the entire TTT diagram using an artificial neural network model trained on data from https://steeldata.ustb.edu.cn and Refs. [102,103]. A combination of different machine learning models can be trained and used to predict the phase diagram of stainless steel [104] and high alloy steels [83]. The CCT diagram for tool steels has also been predicted using various machine learning methods such as bagging and random forest [84].

6. Future perspective

Physics based data-driven approaches have proven useful in constructing phase diagrams and predicting the properties of materials. They are helpful for exploring the compositional space of multi-component alloys and for designing effective heat treatment cycle to obtain the desired set of properties [105,106]. Once trained, the machine learning model can make predictions on target values such as strength, ductility, microstructure, and phases present in a system. Since experiments are laborious, time consuming, and costly, these methods are also beneficial from an industrial perspective. They assist in new alloy design with a set of final properties, by narrowing down the compositional space and predicting potential phases at different temperatures. However, the efficiency of these methods is difficult to quantify for the predictions made outside their training domain. This remains an active area of research in the scientific community. A viable solution to this problem is the active learning of the machine learning model i.e. the model will be continuously trained on new data available while making predictions. In this way, the model will be able to evolve continuously and adapt to the new data.

Progress can be made by complementing the machine learning model with a relevant analytical model which can validate the accuracy of the model's predictions when predicting outside the training domain. However, since a machine learning model is highly non-linear with many-to-many mappings, an analytical model is not available in most cases. In such instances, a sub-domain of the model should be considered and complemented with a known analytical model. For example, Figure 8 illustrates a known analytical model used to complement a sub-domain of a neural network model. The analytical model presents relationships between two input nodes viz., i_1

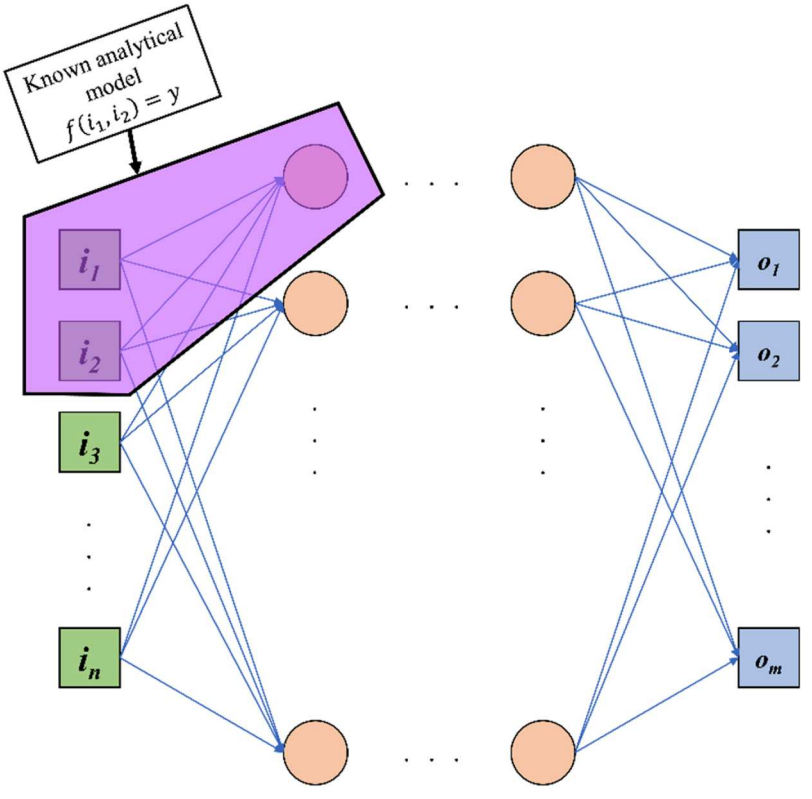

Figure 8. Complementing a sub-domain of a neural network with a known analytical model.

and i_2, using function f. The function value i.e. y, can be treated as the value in one of the hidden layers. Similarly, other areas of the model can be complemented using such knows analytical or thermodynamic models.

7. Concluding remarks

Phase diagrams are irreplaceable tools for understanding thermodynamic stability of various material systems. They provide information such as the composition range over which a particular phase is stable and temperature dependent stability of different intermetallic compounds formed in a multi-component alloy. However, the determination of a phase diagram is a cumbersome process that requires significant experimental resources. Thus, in this review, we have compiled some efforts that have been made to predict phase diagrams using machine learning methods.

Machine learning methods are powerful and have proven useful in the prediction of various types of phase diagrams in materials science and engineering. Data play a key role and are central to all these machine learning methods. The data are used for training machine learning models and making predictions. From the collection of data to the careful building of a robust database, a strong platform is ensured for the success of machine learning methods. However, in most cases, experimental data are scarce, which poses a significant challenge to these data-driven algorithms. In such cases,

computational tools extend a helping hand in enriching the database. Data augmentation also comes in handy to increase the size of the database when needed. These machine learning models are broadly classified as unsupervised and supervised. Unsupervised methods use unlabelled data while supervised methods use labelled data for training. These methods are used in phase diagram predictions by mapping uncertainty, coupling with available computational methods, constructing interatomic potentials, and predicting the phase and transformation behaviour. In most cases, the machine learning predicted phase diagram closely matches the corresponding phase diagram from the literature. However, model predictions outside the training domain are questionable and remain an active area of research in the scientific community. Active learning, in which new data is fed continuously to the model, is employed to improve the model. Furthermore, the model or a section of the model should be complemented with a relevant analytical model to improve its predictions for data outside the training domain.

Disclosure statement

No potential conflict of interest was reported by the author(s).

References

[1] C.-K. Kuo, Z.-X. Lin, and D.-S. Yan, *High Temperature Phase Equilibria and Phase Diagrams*, Elsevier Ltd., Pergamon, 1990. https://doi.org/10.1016/C2009-0-11091-7.
[2] N. Saunders and A.P. Miodownik, *CALPHAD (Calculation of Phase Diagrams): A Comprehensive Guide*, Vol. 1, Elsevier, 1998.
[3] Y.A. Chang, S. Chen, F. Zhang, X. Yan, F. Xie, R. Schmid-Fetzer, and W.A. Oates, *Phase diagram calculation: Past, present and future*. Prog. Mater. Sci. 49 (2004), pp. 313–345. https://doi.org/10.1016/S0079-6425(03)00025-2.
[4] K.-C. Chou and Y. Austin Chang, *A study of ternary geometrical models*. Berichte Der Bunsengesellschaft Für Phys. Chemie 93 (1989), pp. 735–741. https://doi.org/10.1002/bbpc.19890930615.
[5] G. Hautier, A. Jain, and S.P. Ong, *From the computer to the laboratory: Materials discovery and design using first-principles calculations*. J. Mater. Sci 47 (2012), pp. 7317–7340. https://doi.org/10.1007/s10853-012-6424-0.
[6] A. Van de Walle, M. Asta, and G. Ceder, *The alloy theoretic automated toolkit: A user guide*. Calphad Comput. Coupling Phase Diagrams Thermochem 26 (2002), pp. 539–553. https://doi.org/10.1016/S0364-5916(02)80006-2.
[7] J. Wei, X. Chu, X.-Y. Sun, K. Xu, H.-X. Deng, J. Chen, Z. Wei, and M. Lei, *Machine learning in materials science*. InfoMat 1 (2019), pp. 338–358. https://doi.org/10.1002/inf2.12028.
[8] S. Kumar, A.K. Thakur, V. Jindal, and K. Muralidharan, *A neural network driven approach for characterizing the interplay between short range ordering and enthalpy of mixing of binary subsystems in the NbTiVZr high entropy alloy*. J. Phase Equilibria Diffus 44 (2023), pp. 520–538. https://doi.org/10.1007/s11669-023-01055-x.
[9] J. Hegde and B. Rokseth, *Applications of machine learning methods for engineering risk assessment – A review*. Saf. Sci 122 (2020), pp. 104492. https://doi.org/10.1016/J.SSCI.2019.09.015.
[10] Z. Xu and J.H. Saleh, *Machine learning for reliability engineering and safety applications: Review of current status and future opportunities*. Reliab. Eng. Syst. Saf 211 (2021), pp. 107530. https://doi.org/10.1016/J.RESS.2021.107530.
[11] T. Wu and R. Snaiki, *Applications of machine learning to wind engineering*. Front. Built Environ 8 (2022), pp. 6–22. https://doi.org/10.3389/fbuil.2022.811460.

[12] K. Dimililer, H. Dindar, and F. Al-Turjman, *Deep learning, machine learning and internet of things in geophysical engineering applications: An overview*. Microprocess. Microsyst 80 (2021), pp. 103613. https://doi.org/10.1016/J.MICPRO.2020.103613.
[13] K. Tsutsui and K. Moriguchi, *A computational experiment on deducing phase diagrams from spatial thermodynamic data using machine learning techniques*. Calphad 74 (2021), pp. 102303. https://doi.org/10.1016/J.CALPHAD.2021.102303.
[14] G. Deffrennes, K. Terayama, T. Abe, and R. Tamura, *A machine learning–based classification approach for phase diagram prediction*. Mater. Des 215 (2022), pp. 110497. https://doi.org/10.1016/J.MATDES.2022.110497.
[15] N. Artrith, A. Urban, and G. Ceder, *Constructing first-principles phase diagrams of amorphous LixSi using machine-learning-assisted sampling with an evolutionary algorithm*. J. Chem. Phys 148 (2018), pp. 241711. https://doi.org/10.1063/1.5017661.
[16] T. Aoyagi, *Deep learning model for predicting phase diagrams of block copolymers*. Comput. Mater. Sci 188 (2021), pp. 110224. https://doi.org/10.1016/J.COMMATSCI.2020.110224.
[17] J. He, X. Su, C. Wang, J. Li, Y. Hou, Z. Li, C. Liu, D. Xue, J. Cao, Y. Su, L. Qiao, T. Lookman, and Y. Bai, *Machine learning assisted predictions of multi-component phase diagrams and fine boundary information*. Acta Mater. 240 (2022), pp. 118341. https://doi.org/10.1016/J.ACTAMAT.2022.118341.
[18] J. Lund, H. Wang, R.D. Braatz, and R.E. García, *Machine learning of phase diagrams*. Mater. Adv 3 (2022), pp. 8485–8497. https://doi.org/10.1039/D2MA00524G.
[19] A.T. Dinsdale, *Sgte data for pure elements*. Calphad 15 (1991), pp. 317–425.
[20] J. Malcolm and W. Chase, *NIST-JANAF Thermochemical Tables, Fourth Edition*, American Chemical Society, Washington, DC, 1998, New York : American Institute of Physics for the National Institute of Standards and Technology. https://search.library.wisc.edu/catalog/999842910902121.
[21] M. Caffrey and J. Hogan, *LIPIDAT: A database of lipid phase transition temperatures and enthalpy changes. DMPC data subset analysis*. Chem. Phys. Lipids 61 (1992), pp. 1–109. https://doi.org/10.1016/0009-3084(92)90002-7.
[22] A. Jain, S.P. Ong, G. Hautier, W. Chen, W.D. Richards, S. Dacek, S. Cholia, D. Gunter, D. Skinner, G. Ceder, and K.A. Persson, *Commentary: The materials project: A materials genome approach to accelerating materials innovation*. APL Mater. 1 (2013), pp. 11002. https://doi.org/10.1063/1.4812323.
[23] J.E. Saal, S. Kirklin, M. Aykol, B. Meredig, and C. Wolverton, *Materials design and discovery with high-throughput density functional theory : The open quantum materials database (OQMD)*. JOM 65 (2013), pp. 1501–1509. https://doi.org/10.1007/s11837-013-0755-4.
[24] S. Kirklin, J.E. Saal, B. Meredig, A. Thompson, J.W. Doak, M. Aykol, S. Rühl, and C. Wolverton, The Open Quantum Materials Database (OQMD): assessing the accuracy of DFT formation energies. npj Comput Mater 1 (2015), pp. 15010. https://doi.org/10.1038/npjcompumats.2015.10.
[25] S. Curtarolo, W. Setyawan, G.L.W. Hart, M. Jahnatek, R.V. Chepulskii, R.H. Taylor, S. Wang, J. Xue, K. Yang, O. Levy, M.J. Mehl, H.T. Stokes, D.O. Demchenko, and D. Morgan, *AFLOW: An automatic framework for high-throughput materials discovery*. Comput. Mater. Sci 58 (2012), pp. 218–226. https://doi.org/10.1016/J.COMMATSCI.2012.02.005.
[26] R.T. Downs and M. Hall-Wallace, *The American mineralogist crystal structure database*. Am. Mineral 88 (2003), pp. 247–250.
[27] J.J. Bernal, P. Haenecour, J. Howe, T.J. Zega, S. Amari, and L.M. Ziurys, *Formation of interstellar C 60 from silicon carbide circumstellar grains*. Astrophys. J 883 (2019), pp. L43. https://doi.org/10.3847/2041-8213/ab4206.
[28] S. Kumar and G.S. Mahobia, *The features of metal dusting process in the extremely low nickel austenitic stainless steel (18Cr-21Mn-0.65N-Fe)*. Corros. Sci 176 (2020), pp. 108926. https://doi.org/10.1016/J.CORSCI.2020.108926.

[29] A.K. Thakur, R.P. Gorrey, V. Jindal, and K. Muralidharan, *A data-driven approach to approximate the correlation functions in cluster variation method*. Model. Simul. Mater. Sci. Eng 30 (2022), pp. 015001. https://doi.org/10.1088/1361-651X/ac3a16.
[30] V. Jindal, B.N. Sarma, and S. Lele, *A thermodynamic assessment of the Cr–Mo system using CE-CVM*. Calphad 43 (2013), pp. 80–85. https://doi.org/10.1016/J.CALPHAD.2013.10.003.
[31] A. Blázquez-Garc\'\ia, A. Conde, U. Mori, and J.A. Lozano, *A review on outlier/anomaly detection in time series data*. ACM Comput. Surv 54 (2021), 1–33. https://doi.org/10.1145/3444690.
[32] S. Kumari, C. Prabha, A. Karim, M.M. Hassan, and S. Azam, *A comprehensive investigation of anomaly detection methods in deep learning and machine learning: 2019–2023*. IET Inf. Secur. 2024 (2024), pp. 8821891. https://doi.org/10.1049/2024/8821891.
[33] A.K. Thakur, V.K. Pandey, and V. Jindal, *Calculation of existence domains and optimized phase diagram for the Nb-Ti binary alloy system using computational methods*. J. Phase Equilibria Diffus. 41 (2020), pp. 846–858. https://doi.org/10.1007/s11669-020-00843-z.
[34] A.R.G. Brown and K.S. Jepson, *Métallurgie physique et charactéristiques mécaniques des alliages titane-niobium*. Mem. Etud. Sci. Rev. Met. 63 (1966), pp. 575–584.
[35] R.H. Kane, B.C. Giessen, and N.J. Grant, *New metastable phases in binary tin alloy systems*. Acta Metall. 14 (1966), pp. 605–609. https://doi.org/10.1016/0001-6160(66)90068-X.
[36] B. Huang, K.N. Ishihara, and P.H. Shingu, *Metastable phases of Al–Fe system by mechanical alloying*. Mater. Sci. Eng. A 231 (1997), pp. 72–79. https://doi.org/10.1016/S0921-5093(97)00041-5.
[37] C.D. Cao, Z. Sun, X.J. Bai, L.B. Duan, J.B. Zheng, and F. Wang, *Metastable phase diagrams of Cu-based alloy systems with a miscibility gap in undercooled state*. J. Mater. Sci 46 (2011), pp. 6203–6212. https://doi.org/10.1007/s10853-011-5612-7.
[38] Z. Yan, H. Liang, J. Wang, H. Zhang, A.K. da Silva, S. Liang, Z. Rao, and X. Zeng, *PDGPT: A large language model for acquiring phase diagram information in magnesium alloys*. Mater. Genome Eng. Adv 2 (2024), pp. e77. https://doi.org/10.1002/mgea.77.
[39] G.R. Schleder, A.C.M. Padilha, C.M. Acosta, M. Costa, and A. Fazzio, *From DFT to machine learning: Recent approaches to materials science–a review*. J. Phys. Mater 2 (2019), pp. 032001. https://doi.org/10.1088/2515-7639/ab084b.
[40] R. Cohn and E. Holm, *Unsupervised machine learning via transfer learning and k-means clustering to classify materials image data*. Integr. Mater. Manuf. Innov 10 (2021), pp. 231–244.
[41] A. Zhitenev, M. Salynova, A. Shamshurin, S. Ryaboshuk, and V. Kolnyshenko, *Database clustering after automatic feature analysis of nonmetallic inclusions in steel*. Metals 11 (2021), 1650. https://doi.org/10.3390/met11101650.
[42] X. Telleria-Allika, J.M. Mercero, X. Lopez, and J.M. Matxain, *Building machine learning assisted phase diagrams: Three chemically relevant examples*. AIP Adv. 12 (2022), pp. 75206. https://doi.org/10.1063/5.0088784.
[43] K. Rajan, C. Suh, and P.F. Mendez, *Principal component analysis and dimensional analysis as materials informatics tools to reduce dimensionality in materials science and engineering*. Stat. Anal. Data Min. ASA Data Sci. J 1 (2009), pp. 361–371. https://doi.org/10.1002/sam.10031.
[44] M.S. Islam and S. Alam, *Principal component and multiple regression analysis for steel fiber reinforced concrete (SFRC) beams*. Int. J. Concr. Struct. Mater 7 (2013), pp. 303–317. https://doi.org/10.1007/s40069-013-0059-7.
[45] M. Alamin, G.Y. Tian, A. Andrews, and P. Jackson, *Principal component analysis of pulsed eddy current response from corrosion in mild steel*. IEEE Sens. J 12 (2012), pp. 2548–2553. https://doi.org/10.1109/JSEN.2012.2195308.
[46] M.R. Azim and M. Gül, *Data-driven damage identification technique for steel truss railroad bridges utilizing principal component analysis of strain response*. Struct. Infrastruct. Eng 17 (2021), pp. 1019–1035. https://doi.org/10.1080/15732479.2020.1785512.
[47] V. Nasteski, *An overview of the supervised machine learning methods*. Horizons. B 4 (2017), pp. 56–62.

[48] J. Greasley and P. Hosein, *Exploring supervised machine learning for multi-phase identification and quantification from powder X-ray diffraction spectra*. J. Mater. Sci 58 (2023), pp. 5334–5348. https://doi.org/10.1007/s10853-023-08343-4.
[49] T.L. Tepla, I.V. Izonin, Z.A. Duriagina, R.O. Tkachenko, A.M. Trostianchyn, I.A. Lemishka, and V.V. Kulyk, *Alloys selection based on the supervised learning technique for design of biocompatible medical materials*. Arch. Mater. Sci. Eng 93 (2018), pp. 32–40. https://doi.org/10.5604/01.3001.0012.6944.
[50] V. Revi, S. Kasodariya, A. Talapatra, G. Pilania, and A. Alankar, *Machine learning elastic constants of multi-component alloys*. Comput. Mater. Sci 198 (2021), pp. 110671. https://doi.org/10.1016/j.commatsci.2021.110671.
[51] A. Choudhury, T. Konnur, P.P. Chattopadhyay, and S. Pal, *Structure prediction of multi-principal element alloys using ensemble learning*. Eng. Comput. 37 (2020), pp. 1003–1022. https://doi.org/10.1108/EC-04-2019-0151.
[52] J.E. van Engelen and H.H. Hoos, *A survey on semi-supervised learning*. Mach. Learn. 109 (2020), pp. 373–440. https://doi.org/10.1007/s10994-019-05855-6.
[53] Y. Matsuo, Y. LeCun, M. Sahani, D. Precup, D. Silver, M. Sugiyama, E. Uchibe, and J. Morimoto, *Deep learning, reinforcement learning, and world models*. Neural Netw. 152 (2022), pp. 267–275. https://doi.org/10.1016/j.neunet.2022.03.037.
[54] A. Paszke, S. Gross, F. Massa, A. Lerer, J. Bradbury, G. Chanan, T. Killeen, Z. Lin, N. Gimelshein, L. Antiga, A. Desmaison, A. Köpf, E. Yang, Z. DeVito, M. Raison, A. Tejani, S. Chilamkurthy, B. Steiner, L. Fang, J. Bai, and S. Chintala, *Pytorch: An imperative style, high-performance deep learning library*. Advances in Neural Information Processing Systems 32 (2019), pp. 8024–8035.
[55] A. Martín, A. Ashish, B. Paul, B. Eugene, C. Zhifeng, C. Craig, C. Greg S, D. Andy, D. Jeffrey, D. Matthieu, G. Sanjay, G. Ian, H. Andrew, I. Geoffrey, I. Michael, Y. Jia, J. Rafal, K. Lukasz, K. Manjunath, L. Josh, M. Dandelion, M. Rajat, M. Sherry, M. Derek, O. Chris, S. Mike, S. Jonathon, S. Benoit, S. Ilya, T. Kunal, T. Paul, V. Vincent, V. Vijay, V. Fernanda, V. Oriol, W. Pete, W. Martin, W. Martin, Y. Yuan, and Z. Xiaoqiang. {TensorFlow}: Large-scale machine learning on heterogeneous systems, (2015). https://www.tensorflow.org/.
[56] W.H. Chen, S.H. Hsu, and H.P. Shen, *Application of SVM and ANN for intrusion detection*. Comput. Oper. Res 32 (2005), pp. 2617–2634. https://doi.org/10.1016/J.COR.2004.03.019.
[57] R. Kikuchi, *A theory of cooperative phenomena*. Phys. Rev 81 (1951), pp. 988–1003.
[58] A. Zunger, S.-H. Wei, L.G. Ferreira, and J.E. Bernard, *Special quasirandom structures*. Phys. Rev. Lett. 65 (1990), pp. 353–356. https://doi.org/10.1103/PhysRevLett.65.353.
[59] J. Miao and L. Niu, *A survey on feature selection*. Procedia Comput. Sci 91 (2016), pp. 919–926. https://doi.org/10.1016/J.PROCS.2016.07.111.
[60] M.C. Barbieri, B.I. Grisci, and M. Dorn, *Analysis and comparison of feature selection methods towards performance and stability*. Expert Syst. Appl 249 (2024), pp. 123667. https://doi.org/10.1016/J.ESWA.2024.123667.
[61] X. Ying, *An overview of overfitting and its solutions*. J. Phys. Conf. Ser 1168 (2019), pp. 22022. https://doi.org/10.1088/1742-6596/1168/2/022022.
[62] M. Stone, *Cross-Validatory choice and assessment of statistical predictions*. J. R. Stat. Soc. Ser. B 36 (1974), pp. 111–147. http://www.jstor.org/stable/2984809.
[63] J. Ding, B. Chen, H. Liu, and M. Huang, *Convolutional neural network With data augmentation for SAR target recognition*. IEEE Geosci. Remote Sens. Lett 13 (2016), pp. 364–368. https://doi.org/10.1109/LGRS.2015.2513754.
[64] L. Taylor and G. Nitschke, *Improving deep learning with generic data augmentation,* in *2018 IEEE Symposium Series on Computational Intelligence (SSCI)*, Bangalore, India, IEEE, 2018, pp. 1542–1547. https://doi.org/10.1109/SSCI.2018.8628742.
[65] O. Balabanov and M. Granath, *Unsupervised learning using topological data augmentation*. Phys. Rev. Res 2 (2020), pp. 13354. https://doi.org/10.1103/PhysRevResearch.2.013354.
[66] A. Nguyen, J. Clune, Y. Bengio, A. Dosovitskiy, and J. Yosinski. Plug & play generative networks: conditional iterative generation of images in latent space, (2016).

[67] B. Ma, X. Wei, C. Liu, X. Ban, H. Huang, H. Wang, W. Xue, S. Wu, M. Gao, Q. Shen, M. Mukeshimana, A.O. Abuassba, H. Shen, and Y. Su, *Data augmentation in microscopic images for material data mining*. Npj Comput. Mater 6 (2020), pp. 125. https://doi.org/10.1038/s41524-020-00392-6.

[68] H. Ohno, *Auto-encoder-based generative models for data augmentation on regression problems*. Soft. Comput. 24 (2020), pp. 7999–8009. https://doi.org/10.1007/s00500-019-04094-0.

[69] I. Izonin, R. Tkachenko, N. Horbal, M. Greguš, V. Verhun, and Y. Tolstyak, *An approach toward numerical data augmentation and regression modeling using polynomial-kernel-based SVR*, in *Proceedings of International Conference on Data Science and Application*, M. Saraswat, S. Roy, C. Chowdhury, and A.H. Gandomi, eds., Springer Singapore, Singapore, 2022. pp. 771–781.

[70] J. Kuha, *Estimation by data augmentation in regression models with continuous and discrete covariates measured with error*. Stat. Med 16 (1997), pp. 189–201. https://doi.org/10.1002/(SICI)1097-0258(19970130)16:2<189::AID-SIM479>3.0.CO;2-H.

[71] C. Shorten and T.M. Khoshgoftaar, *A survey on image data augmentation for deep learning*. J. Big Data 6 (2019), pp. 60. https://doi.org/10.1186/s40537-019-0197-0.

[72] N.V. Chawla, K.W. Bowyer, L.O. Hall, and W.P. Kegelmeyer, SMOTE: Synthetic minority over-sampling technique. J. Artif. Intell. Res. 16 (2002), pp. 321–357. https://doi.org/10.1613/jair.953.

[73] K. Terayama, K. Han, R. Katsube, I. Ohnuma, T. Abe, Y. Nose, and R. Tamura, *Acceleration of phase diagram construction by machine learning incorporating Gibbs' phase rule*. Scr. Mater 208 (2022), pp. 114335. https://doi.org/10.1016/J.SCRIPTAMAT.2021.114335.

[74] R. Tamura, G. Deffrennes, K. Han, T. Abe, H. Morito, Y. Nakamura, M. Naito, R. Katsube, N. Yoshitaro, and K. Terayama, *Machine-Learning-Based phase diagram construction for high-throughput batch experiments*. Sci. Technol. Adv. Mater. Methods 2 (2022), pp. 153–161. https://doi.org/10.1080/27660400.2022.2076548.

[75] I.A. Kruglov, A. Yanilkin, A.R. Oganov, and P. Korotaev, *Phase diagram of uranium from ab initio calculations and machine learning*. Phys. Rev. B 100 (2019), pp. 174104. https://doi.org/10.1103/PhysRevB.100.174104.

[76] Z.W. Ulissi, A.R. Singh, C. Tsai, and J.K. Nørskov, *Automated discovery and construction of surface phase diagrams using machine learning*. J. Phys. Chem. Lett 7 (2016), pp. 3931–3935. https://doi.org/10.1021/acs.jpclett.6b01254.

[77] K. Lee, Y. Park, and S. Han, *Ab initio construction of full phase diagram of MgO-CaO eutectic system using neural network interatomic potentials*. Phys. Rev. Mater 6 (2022), pp. 113802. https://doi.org/10.1103/PhysRevMaterials.6.113802.

[78] C.W. Rosenbrock, K. Gubaev, A.V. Shapeev, L.B. Pártay, N. Bernstein, G. Csányi, and G.L.W. Hart, *Machine-learned interatomic potentials for alloys and alloy phase diagrams*. Npj Comput. Mater 7 (2021), pp. 24. https://doi.org/10.1038/s41524-020-00477-2.

[79] F. Zipoli, V. Viterbo, O. Schilter, L. Kahle, and T. Laino, *Prediction of phase diagrams and associated phase structural properties*. Ind. & Eng. Chem. Res 61 (2022), pp. 8378–8389. https://doi.org/10.1021/acs.iecr.2c00355.

[80] S.D.M. Kundu, S. Ganguly, and P.P. Chattopadhyay, *Simulating time temperature transformation diagram of steel using artificial neural network*. Mater. Manuf. Process 24 (2009), pp. 169–173. https://doi.org/10.1080/10426910802612239.

[81] N. Pillai and R. Karthikeyan, *Prediction of ttt curves of cold working tool steels using support vector machine model*. IOP Conf. Ser. Mater. Sci. Eng 346 (2018), pp. 12067. https://doi.org/10.1088/1757-899X/346/1/012067.

[82] X. Huang, B. Zhang, Q. Tian, H. Wu, B. Gan, Z. Bi, W. Xue, A. Ullah, and H. Wang, *Machine learning study on time–temperature–transformation diagram of carbon and low-alloy steel*. J. Iron Steel Res. Int 30 (2023), pp. 1032–1041. https://doi.org/10.1007/s42243-023-00932-6.

[83] X. Huang, H. Wang, W. Xue, A. Ullah, S. Xiang, H. Huang, L. Meng, G. Ma, and G. Zhang, *A combined machine learning model for the prediction of time-temperature-transformation*

diagrams of high-alloy steels. J. Alloys Compd 823 (2020), pp. 153694. https://doi.org/10.1016/J.JALLCOM.2020.153694.

[84] X. Geng, H. Wang, W. Xue, S. Xiang, H. Huang, L. Meng, and G. Ma, *Modeling of CCT diagrams for tool steels using different machine learning techniques*. Comput. Mater. Sci 171 (2020), pp. 109235. https://doi.org/10.1016/J.COMMATSCI.2019.109235.

[85] S. Acevedo, M. Arlego, and C.A. Lamas, *Phase diagram study of a two-dimensional frustrated antiferromagnet via unsupervised machine learning*. Phys. Rev. B 103 (2021), pp. 134422. https://doi.org/10.1103/PhysRevB.103.134422.

[86] J. Heger, G. Desai, and M. Zein El Abdine, *Anomaly detection in formed sheet metals using convolutional autoencoders*. Procedia CIRP 93 (2020), pp. 1281–1285. https://doi.org/10.1016/J.PROCIR.2020.04.106.

[87] Y.-X. Guo, Y.-B. Zhuang, J. Shi, and J. Cheng, *Checmate: A workflow package to automatically generate machine learning potentials and phase diagrams for semiconductor alloys*. J. Chem. Phys 159 (2023), pp. 94801. https://doi.org/10.1063/5.0166858.

[88] S. Srinivasan, R. Batra, D. Luo, T. Loeffler, S. Manna, H. Chan, L. Yang, W. Yang, J. Wen, P. Darancet, and S.K.R.S. Sankaranarayanan, *Machine learning the metastable phase diagram of covalently bonded carbon*. Nat. Commun 13 (2022), pp. 3251. https://doi.org/10.1038/s41467-022-30820-8.

[89] K. Lee, D. Yoo, W. Jeong, and S. Han, *SIMPLE-NN: An efficient package for training and executing neural-network interatomic potentials*. Comput. Phys. Commun 242 (2019), pp. 95–103. https://doi.org/https://doi.org/10.1016j.cpc.2019.04.014.

[90] A. Khorshidi and A.A. Peterson, *Amp: A modular approach to machine learning in atomistic simulations*. Comput. Phys. Commun 207 (2016), pp. 310–324. https://doi.org/10.1016/J.CPC.2016.05.010.

[91] A. Singraber, mpbircher, S. Reeve, D.W.H. Swenson, and J. Lauret. philippedavid, CompPhysVienna/n2p2: Version 2.1.4, (2021).

[92] S. Hajinazar, A. Thorn, E.D. Sandoval, S. Kharabadze, and A.N. Kolmogorov, *MAISE: Construction of neural network interatomic models and evolutionary structure optimization*. Comput. Phys. Commun 259 (2021), pp. 107679. https://doi.org/10.1016/J.CPC.2020.107679.

[93] N. Artrith, A. Urban, and G. Ceder, *Efficient and accurate machine-learning interpolation of atomic energies in compositions with many species*. Phys. Rev. B 96 (2017), pp. 014112. 1–5. https://doi.org/10.1103/PhysRevB.96.014112.

[94] A.M. Cooper, J. Kästner, A. Urban, and N. Artrith, *Efficient training of ANN potentials by including atomic forces via Taylor expansion and application to water and a transition-metal oxide*. Npj Comput. Mater 6 (2020), pp. 54. https://doi.org/10.1038/s41524-020-0323-8.

[95] J. Behler, *Atom-centered symmetry functions for constructing high-dimensional neural network potentials*. J. Chem. Phys 134 (2011), pp. 074106. https://doi.org/10.1063/1.3553717.

[96] J. Roberts, B. Rijal, S. Divilov, J.-P. Maria, W.G. Fahrenholtz, D.E. Wolfe, D.W. Brenner, S. Curtarolo, and E. Zurek. Machine learned interatomic potentials for ternary carbides trained on the AFLOW database, ArXiv Prepr. ArXiv2401.01852. (2024). https://arxiv.org/abs/2401.01852.

[97] H. Zong, H. Wiebe, and G.J. Ackland, *Understanding high pressure molecular hydrogen with a hierarchical machine-learned potential*. Nat. Commun 11 (2020), pp. 5014. https://doi.org/10.1038/s41467-020-18788-9.

[98] T.T. Htet, Z. Yan, and Z. Li, *Study on hydrogen smelting reduction behaviour in synthetic molten HIsarna slag*. Ironmak. & Steelmak 50 (2023), pp. 1590–1600. https://doi.org/10.1080/03019233.2023.2204267.

[99] S. Zhu, D. Sarıtürk, and R. Arróyave, *Accelerating CALPHAD-based phase diagram predictions in complex alloys using universal machine learning potentials: Opportunities and challenges*. Acta Mater. 286 (2025), pp. 120747. https://doi.org/10.1016/J.ACTAMAT.2025.120747.

[100] G. Vazquez, D. Sauceda, and R. Arróyave, *Deciphering chemical ordering in high entropy materials: A machine learning-accelerated high-throughput cluster expansion approach*. Acta Mater. 276 (2024), pp. 120137. https://doi.org/10.1016/J.ACTAMAT.2024.120137.

[101] S. Lotfi, Z. Zhang, G. Viswanathan, K. Fortenberry, A. Mansouri Tehrani, and J. Brgoch, *Targeting productive composition space through machine-learning-directed inorganic synthesis*. Matter 3 (2020), pp. 261–272. https://doi.org/10.1016/j.matt.2020.05.002.

[102] K.G. Yang, *Isothermal Transformation Curve of Steel*, Heilongjiang People's Publ. House, Heilongjiang, China, 1981.

[103] G.F. Vander Voort, *Atlas of Time-Temperature Diagrams for Irons and Steels*. Third Edition. ASM International, United States Steel Corporation, Pittsburgh, 1991. www.asminternational.org.

[104] X. Huang, H. Wang, W. Xue, S. Xiang, H. Huang, L. Meng, G. Ma, A. Ullah, and G. Zhang, *Study on time-temperature-transformation diagrams of stainless steel using machine-learning approach*. Comput. Mater. Sci 171 (2020), pp. 109282. https://doi.org/10.1016/j.commatsci.2019.109282.

[105] A. Bazgir and Y. Zhang, *Machine learning approaches for heat treatment in thermal manufacturing processes: A review*. ASME J. Heat Mass Transf. 148 (2025), pp. 1–123. https://doi.org/10.1115/1.4069270.

[106] S. Wang, J. Li, X. Zuo, N. Chen, and Y. Rong, *An optimized machine-learning model for mechanical properties prediction and domain knowledge clarification in quenched and tempered steels*. J. Mater. Res. Technol 24 (2023), pp. 3352–3362. https://doi.org/10.1016/J.JMRT.2023.03.215.

Taylor & Francis
Taylor & Francis Group

Philosophical Magazine

ISSN: 1478-6435 (Print) 1478-6443 (Online) Journal homepage: www.tandfonline.com/journals/tphm20

Prediction of impact damage to Fe-based amorphous coatings via interpretable machine learning

Hui Guo, Wenhai Sun, Mingsheng Wang, Xingxing Zhou, Weiyan Lu & Limin Xu

To cite this article: Hui Guo, Wenhai Sun, Mingsheng Wang, Xingxing Zhou, Weiyan Lu & Limin Xu (21 Jan 2026): Prediction of impact damage to Fe-based amorphous coatings via interpretable machine learning, Philosophical Magazine, DOI: 10.1080/14786435.2026.2617019

To link to this article: https://doi.org/10.1080/14786435.2026.2617019

PHILOSOPHICAL MAGAZINE
https://doi.org/10.1080/14786435.2026.2617019

Prediction of impact damage to Fe-based amorphous coatings via interpretable machine learning

Hui Guo [a], Wenhai Sun[b], Mingsheng Wang[c], Xingxing Zhou[a], Weiyan Lu[b] and Limin Xu[d]

[a]Institute of Applied Physics, Jiangxi Academy of Sciences, Nanchang, People's Republic of China; [b]Shenyang National Laboratory for Materials Science, Institute of Metal Research, Chinese Academy of Sciences, Shenyang, People's Republic of China; [c]Institute of Metal Research, Chinese Academy of Sciences, Shenyang, People's Republic of China; [d]Key Laboratory of Photonic Technology for Integrated Sensing and Communication, Ministry of Education, Guangdong University of Technology, Guangzhou, People's Republic of China

ABSTRACT

Predicting the impact damage of Fe-based amorphous coatings remains a significant challenge due to the complex, nonlinear effects of key coating properties. This study develops an interpretable machine learning (ML) framework to accurately predict impact performance and elucidate the governing physical mechanisms. Twelve regression models were systematically evaluated. The Multilayer Perceptron (MLP) demonstrating superior performance with the highest determination coefficient (R^2) of 0.968 and the lowest error metrics (MSE: 0.066 mm^2, RMSE: 0.257 mm, MAE: 0.150 mm) on the testing set. Interpretability analysis via Shapley additive explanations (SHAP) quantified the global importance of input features, revealing the following hierarchy: shear stress depth ratio (γ) > residual stress (σ) > through-porosity rate (p) > maximum shear stress (τ). This ranking provides a critical, data-driven design insight: optimising the through-thickness distribution of shear stress (γ) is more crucial for mitigating interfacial delamination than merely increasing compressive residual stress. Further, an explicit, quantitative formula was derived from the MLP model, enabling rapid prediction of impact damage. This work establishes a robust ML-SHAP paradigm that not only deliver a high-accuracy predictive tool but also translates complex model outputs into actionable physical understanding and design priorities for advanced coating engineering.

ARTICLE HISTORY
Received 16 July 2025
Accepted 11 January 2026

KEYWORDS
Coatings; impact damage; machine learning; residual stress; model interpretation

1. Introduction

Fe-based amorphous coatings have attracted worldwide interest owing to their high corrosion resistance [1–5], excellent wear resistance [6–8] and superior thermal neutron

CONTACT Hui Guo guohui@jxas.ac.cn Institute of Applied Physics, Jiangxi Academy of Sciences, Nanchang 330096, People's Republic of China; Weiyan Lu wylv@imr.ac.cn Shenyang National Laboratory for Materials Science, Institute of Metal Research, Chinese Academy of Sciences, Shenyang 110016, People's Republic of China; Limin Xu xulimin@gdut.edu.cn Key Laboratory of Photonic Technology for Integrated Sensing and Communication, Ministry of Education, Guangdong University of Technology, Guangzhou 510006, People's Republic of China
Supplemental data for this article can be accessed online at https://doi.org/10.1080/14786435.2026.2617019.

absorption capability [9]. For practical applications of coatings as structural materials, impact resistance is an important property that would affect the effectiveness and lifetime of the amorphous coatings. The impact behaviour of Fe-based amorphous coatings is influenced primarily by the residual stress, maximum shear stress, variation in the depth of the maximum shear stress with respect to the coating thickness, and through-porosity rate [10,11]. These factors produce complex nonlinear effects on the impact behaviour, making it challenging to develop a constitutive model for describing the impact damage to Fe-based amorphous coatings.

Intelligent machine learning (ML), an advanced data-driven approach, can comprehensively solve bottleneck problems in statistics and materials science [12–15]. In the field of bulk metallic glasses (BMGs), the critical applications of ML are glass forming ability (GFA) [16–21], neutron absorption [22], elastic modulus [17,23,24], soft magnetism [25–32], hardness [33], fracture toughness [34]. Liu et al. [18] developed ML models for predicting the GFA of BMGs from elemental features. Li et al. [23] established and interpreted the elastic predictive models of BMGs via various ML approaches. Guo et al. [34] utilised ML to predict the fracture toughness of BMGs based on chemical composition. However, there is a lack of information on predicting the impact behaviour of Fe-based amorphous coatings. This study develops a predictive model for the impact damage of Fe-based amorphous coatings.

This study employed ML to develop a predictive model for predicting impact damage. First, the correlations among the input features and output impact damage were determined via the Pearson correlation coefficient (PCC), and twelve ML regression models were compared and evaluated. Second, the importance of each feature and the impact on the target impact damage was determined via the Shapley additive explanations (SHAP) method. Third, an explicit expression with significant prediction accuracy for the high impact resistance of Fe-based amorphous coatings was proposed.

2. Datasets and methodology

2.1. Data collection

The dataset for this study was constructed from experimental results previously reported in [10,11], as shown in Figure 1, which were briefly summarised here for completeness and reproducibility. The Fe-based amorphous coatings with nominal chemical compositions of $Fe_{49.7}Cr_{18}Mn_{1.9}Mo_{7.4}W_{1.6}B_{15.2}C_{3.8}Si_{2.4}$ (at.%) were synthesised via a commercially available High-Velocity Oxygen Fuel (HVOF) thermal spray system. The feedstock powder with particle size of 22-53 μm was thermally sprayed onto mild steel plates. Coatings with different thicknesses of 200-800 μm were fabricated by controlling the spraying time. These sources provided measured values for key coating properties that are mechanistically linked to impact failure. Based on this physical understanding (as detailed in Section 2.2), four parameters were selected as input features for the ML models: residual stress (σ), maximum shear stress (τ), shear stress depth ratio (γ), and through-porosity rate (p), as summarised in Table 1. The impact damage was determined by interfacial coating/substrate delamination failure [10,35]. The corresponding delamination length (L) under impact energy of 21.6 J was then regarded as the output parameter. For each coating sample, the L was measured from cross-sectional

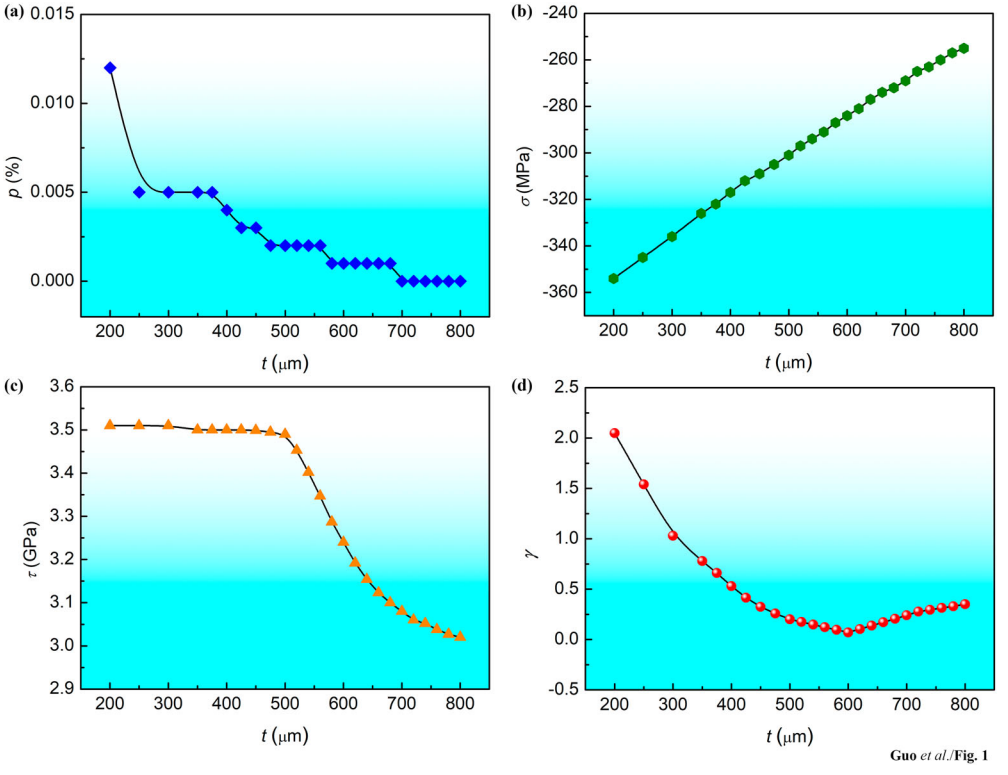

Figure 1. The experimental data on the Fe-based amorphous coatings were obtained from published literature [10,11].

Table 1. Structural features used in building ML models.

Feature name	Description	Refs.
$\sigma = \sigma_{depo} + \sigma_{cool}$	Residual stress	[10]
$\tau = 0.458P_m$	Maximum shear stress	[10]
$\gamma = \lvert z/t_c - 1 \rvert$	The variation in depth of maximum shear stress to coating thickness	[10]
p	Through-porosity rate	[11]

where σ_{depo} is the quenching stress, σ_{cool} is the cooling stress, P_m is the mean contact pressure, z is the corresponding depth of maximum shear stress, t_c is the coating thicknes.

micrographs obtained via Quanta 600 scanning electron microscope (SEM). Under each given condition, at least four samples were tested to ensure repeatability. The data were provided in the Supplementary Materials (Table S1).

2.2. Rationale for feature selection

The selection of the four input features – residual stress (σ), maximum shear stress (τ), shear stress depth ratio (γ), and through-porosity rate (p)—was grounded in both established materials science principles and empirical evidence from prior studies on coating failure mechanics.

Residual stress (σ): Compressive residual stress is widely recognised to enhance a coating's resistance to crack initiation and propagation by effectively closing micro-cracks.

Conversely, tensile residual stress promotes delamination and spallation under impact loading.

Maximum shear stress (τ): Shear stress is a primary driver for the nucleation and growth of shear bands, which are the dominant deformation and failure mechanism in amorphous metallic materials. The magnitude of the maximum shear stress directly influences the propensity for localised plastic flow and subsequent fracture.

Shear stress depth ratio (γ): This dimensionless parameter, γ, indicates the position of the critical stress concentration relative to the coating-substrate interface. A higher γ (stress peak closer to the surface) may lead to surface cracking, while a lower γ (stress peak near the interface) significantly elevates the risk of interfacial delamination, which is the primary failure mode under impact in this study.

Through-porosity rate (p): Porosity acts as intrinsic defects that serve as stress concentrators and preferential sites for crack nucleation. Through-pores, in particular, provide direct pathways for crack propagation, severely compromising the coating's structural integrity and impact resistance.

These four parameters collectively capture the key intrinsic (porosity) and extrinsic (stress state) factors that govern the mechanical response of the coating system under dynamic loading. Their selection ensures the model is based on physically meaningful features, moving beyond a purely black-box correlation to a more interpretable prediction of impact damage (L).

2.3. Feature construction

Prior to model training, all input features (σ, τ, γ, p) were standardised using Equation (1). The target variable L was used in its raw form (mm). No other transformations were applied, and there were no missing values.

$$x = \frac{X\text{-}X_{\text{ave}}}{X_{\text{std}}} \tag{1}$$

where X and x refer to the original and normalised value, respectively; and X_{ave} and X_{std} refer to the average and standard deviation, respectively.

For the input features, the PCC has been extensively employed to identify and analysing key features [36]. The PCC describes the bivariate linear correlation between covariance and standard deviations of two continuous variables, given by Equation (2),

$$\text{PCC} = \frac{\sum_{k=1}^{m}(x_k - \overline{x_k})(y_k - \overline{y_k})}{\sqrt{\sum_{k=1}^{m}(x_k - \overline{x_k})^2 \sum_{k=1}^{m}(y_k - \overline{y_k})^2}} \tag{2}$$

where m is the number of samples ($m = 25$), and x_k and y_k are the values of two normalised variables in the k-th sample ($k = 1, 2, \ldots, 25$). $\overline{x_k}$ and $\overline{y_k}$ are the average values of x_k and y_k, respectively. The PCC values ranges between -1 and 1, whereby -1 indicates that the two normalised variables are absolutely negative correlation, 0 indicates that they are no correlation, and 1 indicates that they are completely positive correlation. A $|\text{PCC}| \geq 0.95$ indicates that two normalised variables are strongly correlated [37], and one of the two normalised variables is removed.

2.4. Machine learning models

In this study, the ML algorithm was implemented via the open source Scikit-Learn [38] and TensorFlow [39] in the Python 3.9.0 environment. The ML algorithms are often categorised into dimensionality reduction, clustering, classification, and regression. In our work, the purpose is to predict a continuous variable, namely, L, which fits into the regression analysis category. We proposed twelve commonly-used ML models, including Ridge Regression (Ridge) [40], Elastic Net Regression (ElasticNet) [41], Support Vector Regression (SVR) [42], k-Nearest Neighbours Regression (KNN) [43], Decision Tree Regression (DT) [44], Extremely Randomised Trees Regression (ETR) [45], Gaussian Process Regression (GPR) [46], Bootstrap Aggregating Regression (Bagging) [47], AdaBoost Regression (AdaBoost) [48], Multilayer Perceptron (MLP) [49], XGBoost Regression (XGBoost) [50], and Gradient Boosting Regression (GBR) [51]. All the forementioned ML models were employed to compare their performance in L prediction and identify the optimal predictive model.

In general, an excellent ML model requires favourable hyper-parameters optimisation to achieve optimal performance. The grid search method over these hyper-parameters with cross validation was conducted to find the best model configuration. In this approach, the preprocessed dataset is randomly divided into training (80%) and testing (20%) subsets. For each set of hyper-parameters, the model is trained on 4 folds and evaluated on the remaining fold. We repeated this procedure 5 times, then reported the average results to obtain the final model performance. The grid search and cross validation (GridSearchCV) can offer reliable and unbiased estimation without much computational cost when the amount of data is small.

To assess the predictive performance of twelve ML regression models, the determination coefficient (R^2), mean square error (MSE), root mean square error (RMSE), and mean absolute error (MAE) are commonly considered quantitative metrics [52], which are described as:

$$R^2 = 1 - \frac{\sum_{k=1}^{m} (L_k - \widehat{L_k})^2}{\sum_{k=1}^{m} (L_k - \overline{L_k})^2} \tag{3}$$

$$\mathrm{MSE} = \frac{1}{m} \sum_{k=1}^{m} (L_k - \widehat{L_k})^2 \tag{4}$$

$$\mathrm{RMSE} = \left(\frac{1}{m} \sum_{k=1}^{m} (L_k - \widehat{L_k})^2 \right)^{0.5} \tag{5}$$

$$\mathrm{MAE} = \frac{1}{m} \sum_{k=1}^{m} |L_k - \widehat{L_k}| \tag{6}$$

where m is the number of samples ($m = 25$). L_k, $\overline{L_k}$ and $\widehat{L_k}$ denote the actual, average and predicted k-th L values ($k = 1, 2, \ldots, 25$), respectively. The R^2 value ranges from -∞ to 1, where a value closer to 1 indicates a strong ability of the model to capture the underlying patterns and explain the data variability. All MSE, RMSE, and MAE values range from 0 to ∞, where values closer to 0 reflecting a better accuracy and robustness of the model.

3. Results and discussion

3.1. Model prediction

Figure 2 displays the PCC heatmap, which shows the relationship among the input features (σ, τ, γ, and p) and the targeted property L. Figure 2 shows that L has a strong correlation with a σ of 0.76, τ of −0.58, γ of −0.79, and p of −0.74. The delamination length L increases with increasing σ. L was highly negatively correlated with γ, p and τ. With increasing γ, p and τ, the crack length L decreases.

To construct the optimal model for predicting L, twelve widely used ML models, Ridge, ElasticNet, SVR, KNN, DT, ETR, GPR, Bagging, AdaBoost, MLP, XGBoost and GBR, were employed and compared. In the ML algorithm, several hyper-parameters can have a significant effect on the model's ability in order to avoid over-fitting and under-fitting. To optimise the twelve models, the hyper-parameters were tuned in GridSearchCV. The parameter space and optimal hyper-parameters are listed in Table 2.

Figure 3 displays the performance metrics, R^2, MSE, RMSE and MAE values of the twelve ML models after hyper-parameters optimisation, which are presented in Table 3. The prediction accuracies of the models are in the order of MLP > GBR > KNN > ETR > AdaBoost > SVR > DT > GPR > XGBoost > Bagging > Ridge > ElasticNet. Among the twelve algorithms, the MLP model yields the highest R^2 value of 0.968 and the lowest MSE, RMSE, and MAE values of 0.066 mm^2, 0.257, and 0.150 mm, respectively, on the testing set, indicating superior prediction accuracy and stronger generalizability.

The wide range of predictive accuracy observed across these models can be understood through the lens of bias-variance trade-off and model capacity. Simple linear models (Ridge, ElasticNet) exhibited underfitting, as their intrinsic bias prevented them from capturing the essential nonlinear relationship between coating properties

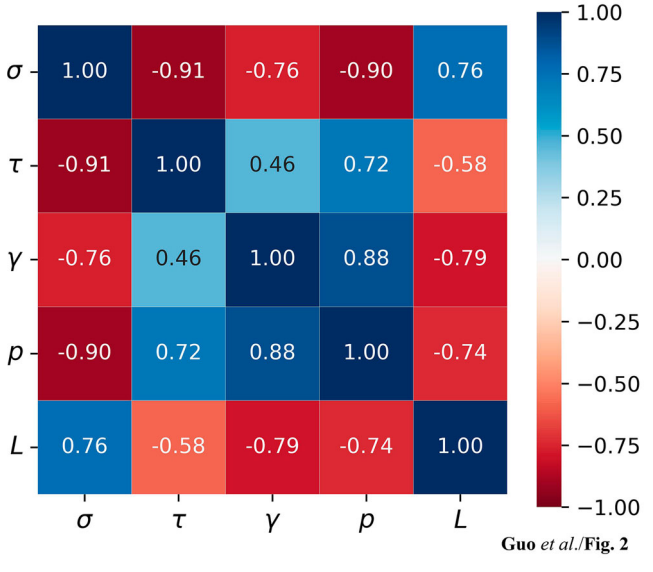

Figure 2. Pearson correlation heatmap of four input features (σ, τ, γ, and p) and the output feature L.

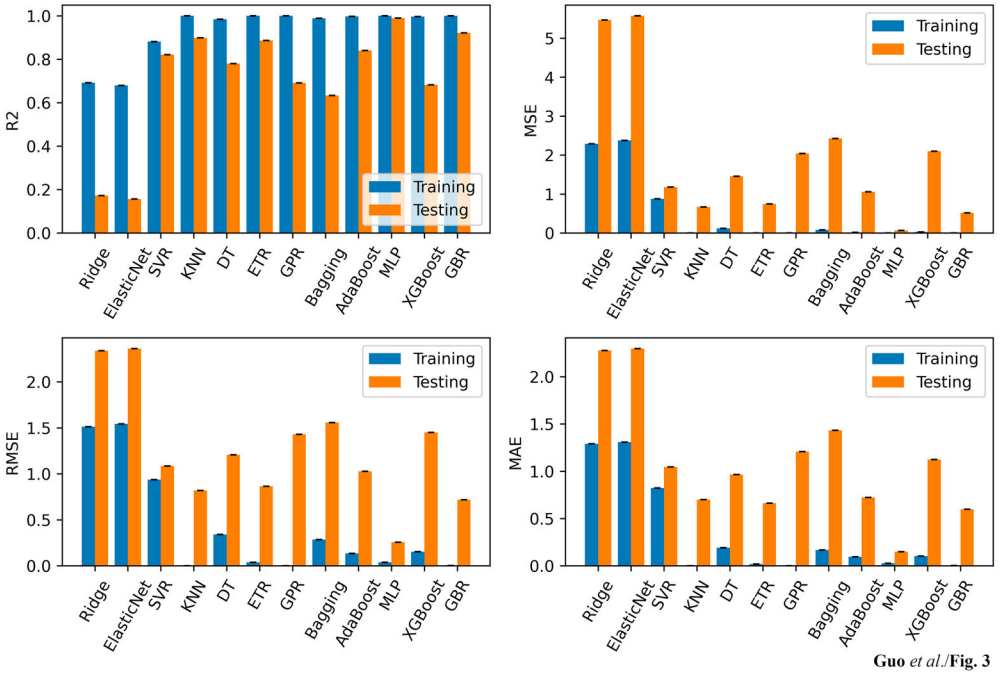

Figure 3. The R^2, MSE, RMSE, and MAE of both the training and testing sets for the twelve individual models.

impact damage. In contrast, highly flexible models like an unconstrained DT are prone to overfitting on small datasets; they can memorise noise in the limited training set ($m = 25$), leading to poor generalisation. The superior performance of the MLP model is a direct result of its appropriate architectural complexity-enabled by its nonlinear activation functions-coupled with effective regularisation (via L2 penalty alpha and a constrained hidden layer). This configuration, identified through hyperparameter tuning and cross-validation, allowed the MLP to learn the generalisable physical principles without adhering to the noise, as confirmed by its high R^2 and low error metrics on the independent testing set. Thus, the MLP model was chosen as the suitable model for predicting the L value of Fe-based amorphous coatings in this study.

Figure 4 depicts the predictive performance of twelve optimised ML models for predicting L. The x-axis expresses the measured L values, whereas the y-axis shows the predicted L values. The red diagonal line $y = x$ indicates perfect fitting. Each point corresponds to the predicted and measured values of a unique coating. The data points form a distribution along this red diagonal line, demonstrating that the ML model equipped with selected important features and optimised hyper-parameters performance reasonably well in predicting the L of Fe-based coatings. The diagonal distribution suggests that the predicted values align well with the measured values, confirming the effectiveness of the model in this context.

Figure 4 clearly shows that the MLP model achieves the best predictive performance in current study. The sparsity of small sample datasets increases the difficulty of ML modelling. The comprehensive performance index of the MLP model has significantly more

Table 2. The utilised hyper-parameters in the twelve models.

Model	Hyper-parameters	Parameter space	Optimal hyper-parameters	Model	Hyper-parameters	Parameter space	Optimal Hyper-parameters
Ridge	alpha	[1, 50]	14	GPR	alpha	[1e-10, 1]	1e-10
	random_state	[1, 50]	1		n_restarts_optimizer	[1, 10]	1
					random_state	[1, 50]	1
ElasticNet	alpha	[0, 1.5]	0.9	Bagging	n_estimators	[0, 20]	7
	l1-ratio	[0, 1]	0		max_samples	[0, 30]	16
	random_state	[1, 50]	1		max_features	[0, 10]	4
					random_state	[1, 35]	19
SVR	degree	[1, 5]	1	AdaBoost	n_estimators	[1, 100]	9
	C	[1, 10]	1		learning_rate	[0.01, 1]	0.01
	gamma	[1, 10]	2		random_state	[1, 50]	4
	epsilon	[1, 10]	1		loss	['linear', 'exponential', 'square']	square
	kernel	['linear', 'poly', 'rbf', 'sigmoid']	sigmoid				
KNN	n_neighbours	[1, 20]	4	MLP	hidden_layer_sizes	[(2,), (3,), (4,), (5,), (6,), (7,), (8,), (9,)]	(6,)
	weights	['uniform', 'distance']	distance		max_iter	[1, 100]	52
	leaf_size	[1, 40]	1		alpha	[1e-10, 1]	1e-10
	p	[1, 5]	1		verbose	[True]	True
	algorithm	['auto', 'kd_tree', 'brute', 'ball_tree']	auto		random_state	[1, 50]	39
					activation	['relu', 'tanh', 'logistic']	tanh
					solver	['sgd', 'lbfgs', 'adam']	lbfgs
DT	max_depth	[1, 20]	6	XGBoost	min_child_weight	[1, 15]	1
	min_samples_leaf	[1, 10]	1		n_estimators	[1, 60]	5
	min_samples_split	[2, 10]	3		max_depth	[1, 12]	4
	max_features	[1, 20]	1		learning_rate	[0.01, 1]	1
	random_state	[1, 40]	9		colsample_bytree	[0.01, 1]	1
	splitter	['best','random']	random		colsample_bylevel	[0.01, 1]	1
					random_state	[1, 30]	26
ETR	n_estimators	[1, 15]	7	GBR	n_estimators	[1, 250]	241
	max_depth	[1, 15]	7		learning_rate	[0.01, 1]	0.06
	min_samples_split	[2, 6]	2		max_depth	[1, 10]	3
	min_samples_leaf	[1, 5]	1		subsample	[0.01, 1]	0.7
	max_features	[1, 10]	1		min_samples_split	[1, 6]	4
	random_state	[1, 40]	22		min_samples_leaf	[1, 3]	1
					random_state	[1, 16]	9
					loss	['huber', 'absolute_error', 'squared_error', 'quantile']	squared_error

Table 3. The R^2, MSE, RMSE and MAE of both the training and testing sets for the twelve individual models.

	Training set				Testing set			
Model	R^2	MSE	RMSE	MAE	R^2	MSE	RMSE	MAE
Ridge	0.692	2.288	1.513	1.291	0.173	5.466	2.338	2.278
ElasticNet	0.680	2.378	1.542	1.309	0.157	5.572	2.361	2.297
SVR	0.882	0.877	0.936	0.822	0.822	1.179	1.086	1.045
KNN	1.000	0.000	0.000	0.000	0.899	0.670	0.819	0.700
DT	0.984	0.116	0.341	0.191	0.780	1.454	1.206	0.965
ETR	1.000	0.001	0.039	0.018	0.887	0.746	0.864	0.663
GPR	1.000	0.000	0.000	0.000	0.691	2.043	1.429	1.208
Bagging	0.989	0.081	0.284	0.167	0.633	2.423	1.557	1.433
AdaBoost	0.998	0.018	0.135	0.096	0.840	1.055	1.027	0.723
MLP	1.000	0.001	0.037	0.026	0.968	0.066	0.257	0.150
XGBoost	0.997	0.024	0.153	0.102	0.682	2.100	1.450	1.124
GBR	1.000	0.000	0.002	0.002	0.922	0.516	0.719	0.598

advantages than other models do, indicating that the neural network can facilitate the generalizability on small samples and sparse datasets. The Ridge and ElasticNet models cannot provide satisfactory predictive capabilities due to the complex nonlinear interactions among the features. In addition, the Bagging, XGBoost, GPR, DT, SVR, AdaBoost, ETR, KNN and GBR models could to some extent consider the effects of nonlinear relationships on L. Moreover, the MLP model considers these interactions more

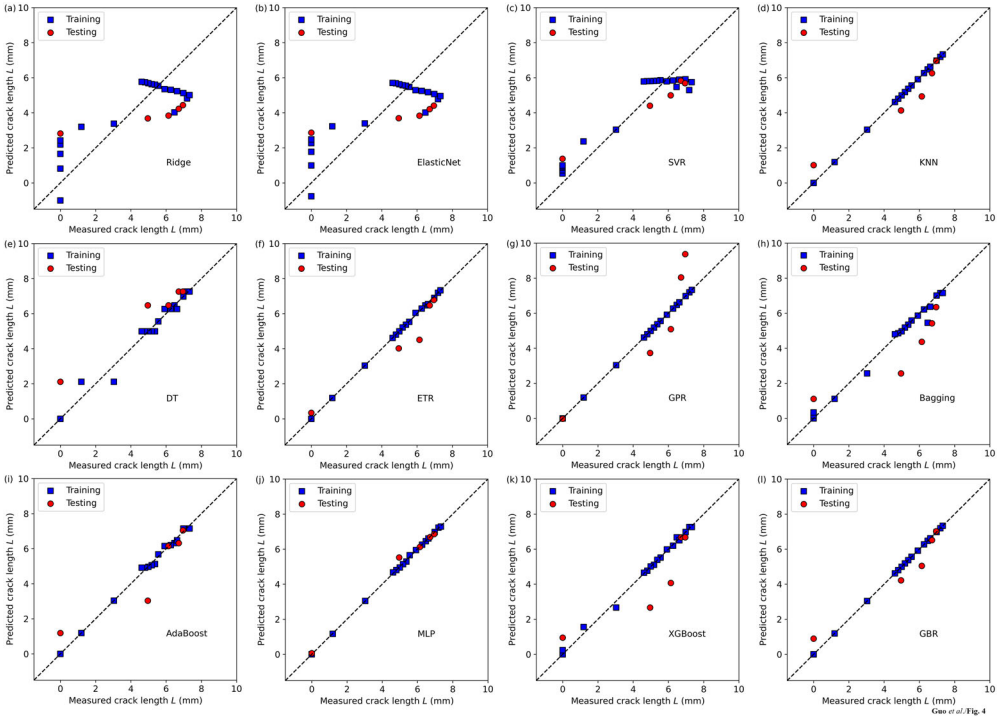

Figure 4. Measured L versus predicted L of models on the training dataset and testing dataset by (a) Ridge, (b) ElasticNet, (c) SVR, (d) KNN, (e) DT, (f) ETR, (g) GPR, (h) Bagging, (i) AdaBoost, (j) MLP, (k) XGBoost, (l) GBR.

comprehensively. Hence, it is unsurprising that the MLP model exhibits the best performance in predicting L, even with a small training dataset among the twelve ML models developed in this study.

3.2. Model interpretation

The effect of each input variable on L remained indeterminate for the key features. To clarify the influence and importance of the features on the predicted L, SHAP is applied to interpret the forwards MLP model. Although the model has high prediction accuracy, it suffers from low interpretability due to its 'black-box' nature [30]. SHAP is a new interpretable method based on game theory that partitions prediction into contribution of each feature [53]. The SHAP value is calculated as follows:

$$\hat{L} = \hat{L}_0 + \sum_{i=1}^{n} \varphi_i \tag{7}$$

$$\varphi_i = \sum_{S \subseteq F \backslash \{i\}} \frac{|S|!(|F| - |S| - 1)!}{|F|!} [f_{S \cup \{i\}}(x_{S \cup \{i\}}) - f_S(x_S)] \tag{8}$$

where $\hat{L}$ is the predicted value, $\hat{L}_0$ is the prediction without any features, φ_i is the SHAP value of the i-th feature, n is the number of input features ($n = 4$), F denotes the set of all features, S denotes the subset of F, $S \cup \{i\}$ denotes the union of S and i-th feature, x_S denotes input features in S, $x_{S \cup \{i\}}$ denotes input features in $S \cup \{i\}$, $f_{S \cup \{i\}}(x_{S \cup \{i\}})$ denotes the prediction of the model trained with the i-th feature, and $f_S(x_S)$ denotes the prediction of the model trained without the i-th feature. The SHAP value can be computed on the MLP model to assess the importance of individual input features in the prediction process and evaluate the impact on the targeted property.

Figure 5(a) illustrates the feature importance ranked by mean absolute SHAP values. The y-axis (ordinate) expresses the importance rankings of different features. The x-axis (abscissa) shows the mean absolute SHAP value. The larger the SHAP value, the greater the feature importance. The importance order of input features affecting L is as follows: $\gamma > \sigma > p > \tau$. Among these features, γ ranks as the most important feature responsible for predicting impact damage, which is consistent with the research results of Wang et al. [10]. The summary plot not only estimates the importance of features but also evaluates how each feature affects impact resistance, as displays in Figure 5(b). The abscissa represents the SHAP values, which indicate the contribution to the impact damage of

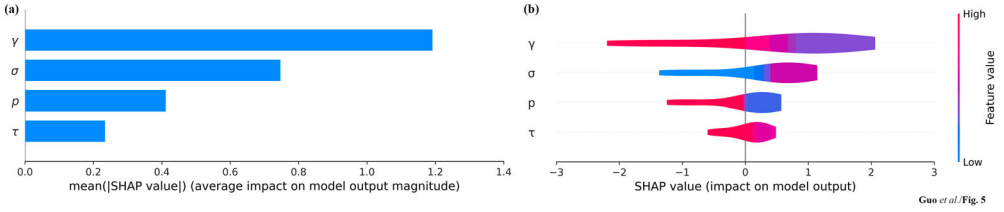

Figure 5. (a) The feature importance of the MLP model. (b) The global interpretation of the MLP model.

individual features. The ordinate represents different features. The colour represents the magnitude of the feature value, ranging from blue to red indicating the feature value from low to high. A positive or negative SHAP value represents favourable or adverse impacts on impact damage. SHAP analysis revealed that γ is the most important feature influencing impact resistance. A higher γ is mainly concentrated in the region of a negative SHAP value. The higher value γ, the smaller SHAP value, suggesting better impact resistance. This negative tendency is also supported by a previous study.

The SHAP analysis revealing the shear stress depth ratio (γ) and maximum shear stress (τ) as critical factors, with residual normal stress (σ) being secondary, offers a nuanced and physically consistent insight into the specific failure mode studied.

While it is well-established that Mode I (tensile/opening) crack growth driven by normal stress is dominant in bulk material fracture, the primary failure mechanism in our impacted coatings is interfacial delamination. For such biomaterial interfaces under impact loading, the stress state is complex. The shear stress parallel to the interface is a primary driver for sliding and debonding at coating-substrate interface. The importance of γ further refines this understanding: it indicates whether the maximum shear driving force for delamination is located perilously close to the interface or safely within the coating bulk. A low γ signifies that the peak shear stress is located dangerously close to the weak coating-substrate interface, greatly amplifying the risk of interfacial failure rather than inducing cracking within the coating bulk. The significant but secondary role of compressive σ is also explicable. Its primary beneficial effect is to 'clamp' the interface shut, thereby increasing the friction and resistance to shear-driven sliding. It mitigates the effect of but does not eliminate the shear driving force itself. Therefore, in the context of interfacial shear-driven delamination-the target failure mode-the model correctly identifies the shear-related parameters (τ and its distribution γ) as the most direct and influential features. The residual stress (σ) act as a crucial, supportive modulator.

This interpretation does not contradict classical fracture mechanics but rather captures the context-specific physics governing interfacial failure under impact. The ranking $\gamma > \sigma > p > \tau$ provides a quantitative, data-validated hierarchy for coating design: prioritise shifting the shear stress profile (γ), then utilise compressive stress (σ) to clamp the interface, while simultaneously minimising porosity (p).

3.3. Model expression

In this work, the finely tuned configuration of the MLP model was created with the following optimal hyper-parameters: the 'Tanh' activation function, an alpha value of 1e-10, a single hidden layer containing 6 neurons, a max_iter value of 52, a random_state value of 39, and 'lbfgs' as the solver, as listed in Table 2. As shown in Figure 6, the MLP model structure is determined as '4-6-1' with the input layer consisting of 4 input features ($x_i|x_1$, x_2, x_3, and x_4), the single hidden layer formed form 6 neurons ($h_j|h_1$, h_2, h_3, h_4, h_5, and h_6), and the output layer representing a single output L. The complex nonlinear relationship is connected through weights (w_{ij} and v_j) and biases (b_j and c) between neurons in each layer including inner product and addition, and the activation functions between layers [54]. The input layer receives features from the dataset and passes them down to the hidden layer [55]. The hidden value

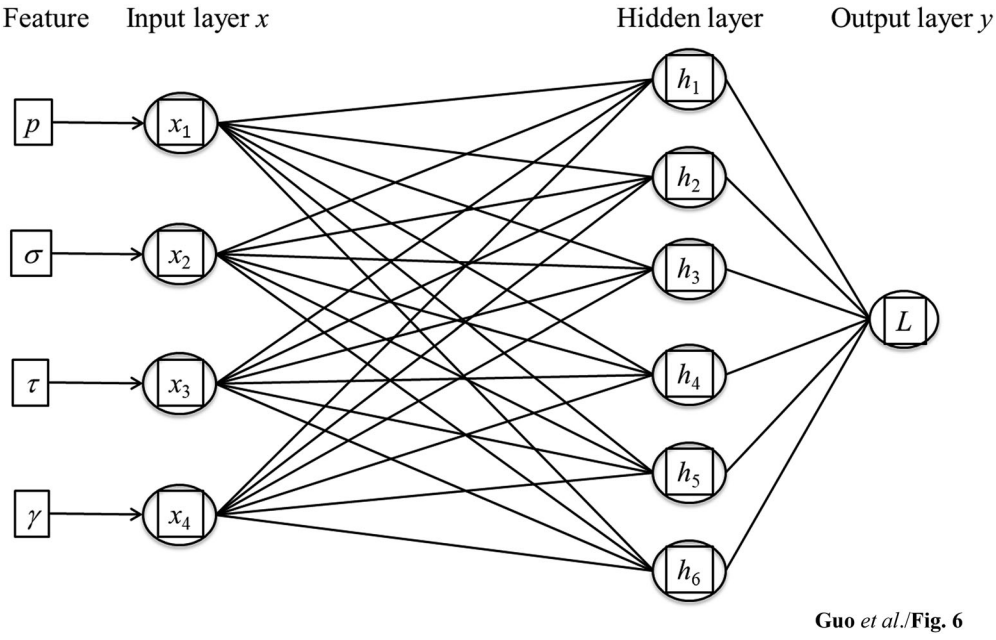

Figure 6. The schematic representation of the MLP algorithm.

h_j can be expressed from the input layer:

$$h_j = \sum_{i=1}^{4} x_i w_{ij} + b_j \tag{9}$$

where x_i represents the i-th normalised input variable ($x_1 = p$, $x_2 = \sigma$, $x_3 = \tau$, $x_4 = \gamma$), h_j denotes the j-th neuron value in the hidden layer ($j = 1, 2, 3, 4, 5, 6$), w_{ij} represents the synaptic weight connecting neuron j in the hidden layer to neuron i in the input layer, and b_j signifies the bias associated with neuron j in the hidden layer.

Each neuron in the hidden layer sums all the weight parameters v_j and bias terms c, and is processed by the nonlinear activation function $f(h_j)$ to produce the output. The output value L can be calculated from the hidden layer:

$$L = \sum_{j=1}^{6} f(h_j) v_j + c \tag{10}$$

where v_j is the synaptic weight connecting the output layer to the neuron j in the hidden layer, and c is the bias associated with the output. $f(h_j)$ represents the activation function in the hidden layer, and the Hyperbolic Tangent function is employed in the current study. Compared with other common activation functions such as the ReLU and Sigmoid functions, the Tanh function results in more steep gradient, thereby accelerating the convergence and optimisation of the model [54,56]. The Tanh specific expression form is $f(h_j) = \tanh(h_j) = \dfrac{e^{h_j} - e^{-h_j}}{e^{h_j} + e^{-h_j}}$. In addition, the Linear activation function is often employed in the output layer as desired for predicting problems.

Finally, the output L of each feature can be expressed as:

$$\begin{aligned} L = {} & v_1 tanh(pw_{11} + sw_{21} + tw_{31} + gw_{41} + b_1) + v_2 tanh(pw_{12} + sw_{22} + tw_{32} + gw_{42} + b_2) \\ & + v_3 tanh(pw_{13} + sw_{23} + tw_{33} + gw_{43} + b_3) + v_4 tanh(pw_{14} + sw_{24} + tw_{34} + gw_{44} + b_4) \\ & + v_5 tanh(pw_{15} + sw_{25} + tw_{35} + gw_{45} + b_5) + v_6 tanh(pw_{16} + sw_{26} + tw_{36} + gw_{46} + b_6) + c \end{aligned} \tag{11}$$

In Equation (11), the weights w_{ij} and v_j, the biases b_j and c, were obtained via an algorithm that is based on a Python code.

$$w_{ij} = \begin{bmatrix} w_{11} & w_{12} & w_{13} & w_{14} & w_{15} & w_{16} \\ w_{21} & w_{22} & w_{23} & w_{24} & w_{25} & w_{26} \\ w_{31} & w_{32} & w_{33} & w_{34} & w_{35} & w_{36} \\ w_{41} & w_{42} & w_{43} & w_{44} & w_{45} & w_{46} \end{bmatrix} = \begin{bmatrix} 0.8671 & 0.2087 & -0.9397 & -1.9308 & -0.4313 & 0.4753 \\ -0.3464 & -0.5614 & 0.8664 & 0.7335 & 0.3775 & -0.1662 \\ 0.0705 & 1.1466 & 2.4206 & 3.0748 & 2.2313 & -1.2721 \\ -0.4178 & 1.1353 & 0.8186 & 1.7296 & 1.4025 & -0.5771 \end{bmatrix}$$

,

$$v_j = \begin{bmatrix} v_1 \\ v_2 \\ v_3 \\ v_4 \\ v_5 \\ v_6 \end{bmatrix} = \begin{bmatrix} -2.3772 \\ -0.0014 \\ -0.7770 \\ -2.4525 \\ 0.1854 \\ 1.9779 \end{bmatrix}, \; b_j = [b_1 \; b_2 \; b_3 \; b_4 \; b_5 \; b_6] = [-1.0558 \; 0.9941 \; -0.4588 \; -1.5168 \; -0.4296 \; -1.3195],$$ and $c = 2.6573$. Therefore, we could obtain an expression of L, which may offer us an advantage in analysing and predicting the impact properties of Fe-based amorphous coatings in the future.

The explicit formula given in Equation (11) is mathematically equivalent to the optimised MLP model. Therefore, it inherits the model's superior predictive accuracy, as evidenced by the testing set performance ($R^2 = 0.968$, MAE = 0.150 mm, RMSE = 0.257 mm). This represents a significant advantage over traditional analytical or finite element methods for this specific problem in several key aspects: (1) It inherently captures complex, nonlinear interactions among the input features without relying on simplified physical assumptions; (2) It provides instantaneous predictions at negligible computational cost once derived, enabling rapid design iteration; and (3) Coupled with the SHAP analysis, it moves beyond a 'black-box' to offer quantifiable, rankable design insights (e.g. prioritising control of γ over τ). While its direct application is validated within the studied parameter space, the formula serves as an efficient and insightful tool for the analysis and design of Fe-based amorphous coatings with targeted impact resistance.

A limitation of this study is the dataset size ($m = 25$), which is typical for experimental studies involving complex material synthesis and testing. While our rigorous validation framework ensures the reliability of the presented model and insights within this scope, future work should aim to expand the dataset. This would allow for the investigation of

higher-order feature interactions and the refinement of the quantitative predictive formula for broader parameter spaces.

3.4. Applicability domain and quantitative model scope

The constants (weights and biases) in Equation (11) are point estimates from a single optimisation. To quantify the statistical stability, a non-parametric bootstrap analysis was performed, as shown in Table 4. The table reports the mean estimate, bootstrap standard error (SE), and 95% confidence interval (CI) for a subset of key parameters. All weights (w_{ij}, v_j) and biases (b_j) are dimensionless, except for the output bias c, which carries the unit of the target (mm). The relatively narrow confidence intervals for influential parameters support the robustness of the identified relationship.

The leverage-based approach is employed to statistically define the Applicability Domain (AD) and flag unreliable predictions. The leverage h_{kk} for a sample k measures its distance from the centroid of the training set in the multi-dimensional feature space. The critical leverage threshold (h^*) is calculated as $h^* = 3(n+1)/t$, where $n = 4$ is the number of features and $t = 19$ is the training set size, yielding $h^* = 0.79$. Any new prediction request where the input feature vector yields a leverage value exceeding this threshold lies far outside the sampled parameter space, and its prediction should be treated with extreme caution or disregarded.

3.5. Robustness and validation analysis

To obtain an unbiased estimate of generalisation error and eliminate any risk of data leakage from hyperparameter tuning, we performed nested leave-one-out cross-validation (LOO-CV). This rigorous procedure yielded R^2 of 0.996 and MAE of 0.102 mm across all folds. These metrics confirm that the MLP model retains exceptional predictive performance even under the most stringent validation protocol.

The learning curves (Figure 7) show that both the training and cross-validation scores rapidly increase and converge as the training set size approaches the full 25 samples. The minimal final gap between the curves indicates that the model is not suffering from high variance (overfitting) and that the available data, while limited, is sufficient to train a stable model for this specific experimental domain.

Residual diagnostics (Figure 8(a)) were performed to validate the regression assumptions. The residuals are randomly scattered around zero with no discernible pattern, indicating homoscedasticity. The Q-Q plot (Figure 8(b)) shows that the residuals closely follow the theoretical normal distribution line, with minor deviations in the extremes. This supports the appropriateness of using least-squares-based error metrics and confirms that the model's errors are well-behaved.

Table 4. Bootstrap uncertainty estimates for selected parameters in Equation (11).

Parameter	Description	Mean Estimate	Bootstrap SE	95% Confidence Interval	Unit
w_{11}	Weight: $p \rightarrow h_1$	0.867	± 0.148	[0.578, 1.162]	–
b_1	Bias for neuron h_1	−1.056	± 0.224	[−1.502, −0.623]	–
v_1	Weight: $h_1 \rightarrow L$	−2.377	± 0.332	[−3.032, −1.735]	–
c	Output layer bias	2.657	± 0.420	[1.842, 3.496]	mm

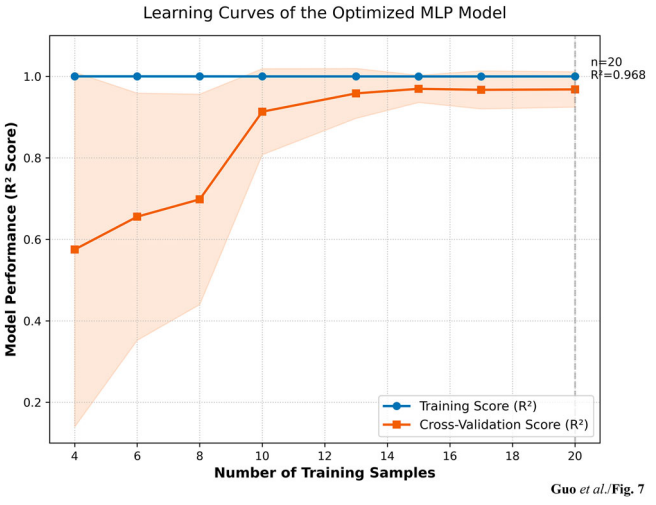

Figure 7. The learning curves of the MLP algorithm.

The combination of nested cross-validation, learning curves, and residual analysis provides a multi-faceted validation of the MLP model. The consistently high performance across these stringent tests strongly suggests that the reported $R^2 = 0.968$ is a credible indicator of the model's predictive power for Fe-based amorphous coatings within the studied parameter space, rather than a statistical artifact of overfitting or data leakage.

3.6. Limitations and pathway for broader deployment

The validity of the model is contingent upon several foundational assumptions. The empirical dataset was generated from coatings fabricated via single thermal process (HVOF), using a specific gas-atomized $Fe_{49.7}Cr_{18}Mn_{1.9}Mo_{7.4}W_{1.6}B_{15.2}C_{3.8}Si_{2.4}$ (at.%) amorphous powder, and deposited on grit-blasted mild steel substrates. The physical

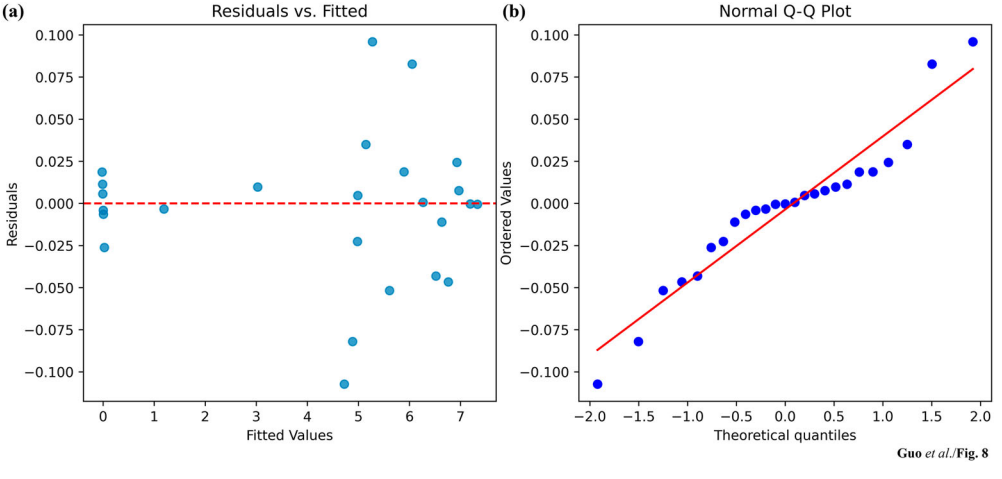

Figure 8. The (a) residual vs. fitted value plots and (b) Q-Q plots of the MLP algorithm.

relationships captured-most notably the dominance of the shear stress depth ratio (γ)-are intrinsically linked to the microstructural characteristics inherent to this specific material-manufacturing combination. The model does not inherently account for variations introduced by alternative deposition techniques (e.g. cold spray, plasma spray), different amorphous alloy compositions (e.g. Zr- or Al-based), or other substrate materials and geometries. The model assumes that the four selected features (σ, τ, γ, p) are necessary and collectively sufficient descriptors of the impact damage mechanics for this system. The features themselves are subject to experimental measurement noise. While the model exhibits robustness to moderate stochastic noise, significant systematic bias in these measurement protocols would degrade its predictive fidelity.

The current model is not a universal predictor. Its application to a distinctly different amorphous coating system necessitates re-calibration or complete re-training. However, the established ML-SHAP framework provides a structured and efficient pathway for this adaptation, significantly lowering the barrier to developing new, high-accuracy models. The neural network developed in this study (Equation (11)) has learned generalised representations of how mechanical stresses, geometry, and defects relate to coating failure. This model can serve as an excellent pre-trained foundation. By using this model as a starting point and fine-tuning its weights on a relatively small, targeted dataset from the new coating process, the model can rapidly adapt to the new system's specific characteristics. This approach leverages prior knowledge and can reduce the required experimental data by an order of magnitude compared to training from random initialisation.

4. Conclusions

This study established an interpretable ML framework to predict and decipher the impact damage of Fe-based amorphous coatings. The main findings and their practical implications are summarised as follows:

(1) A predictive tool for quantitative design

The developed MLP model serves as a high-accuracy predictive tool, achieving a prediction accuracy of $R^2 = 0.968$ and low prediction errors (MAE = 0.150 mm, RMSE = 0.257 mm) on independent testing data. More importantly, the derived explicit expression (Equation (11)) provides a ready-to-use formula for designers. By inputting measurable coating parameters-σ, τ, γ, and p-within the validated ranges, the L can be calculated instantaneously, enabling rapid performance screening and design iteration.

(2) Quantitative design priority from mechanism insight

Beyond prediction, the SHAP-based interpretation delivers a clear, quantitative hierarchy of influence for the key parameters: $\gamma > \sigma > p > \tau$. This ranking translates directly into a design action priority:

- Primary focus (γ): Optimise the coating thickness and deposition process to maximise the shear stress depth ratio (increase γ), thereby moving the critical stress concentration away from the weak interface.

- Secondary lever (σ): Induce and control moderate compressive residual stress to enhance interfacial clamping and resistance to shear-driven delamination.
- Critical constraint (p): Strictly minimise through-porosity, as it consistently acts as a stress concentrator that degrades impact resistance.

This insight shifts the design paradigm from a trial-and-error approach to a targeted, physics-informed optimisation strategy.

(3) Validation of a data-driven discovery paradigm

This work validates an ML-SHAP discovery pipeline that is particularly valuable for data-scarce experimental fields. The pipeline successfully transformed a limited dataset into a robust predictive model and quantitative design rules. This methodology is not limited to Fe-based coatings, it provides a generalisable blueprint for uncovering property–structure-process relationships in other complex material systems.

Credit authorship contribution statement

H. Guo: Methodology, formal analysis, software, validation, investigation, data curation, conceptualisation, writing – original draft, writing – review & editing, funding acquisition, supervision. **W.H. Sun:** Methodology, data curation. **M.S. Wang:** Methodology, data curation. **X.X. Zhou:** Methodology, data curation. **W.Y. Lu:** Methodology, data curation, investigation. **L.M. Xu:** Methodology, data curation, software, writing – review & editing.

Disclosure statement

No potential conflict of interest was reported by the author(s).

Funding

This work was supported by National Natural Science Foundation of China [grant number 52001148]; Jiangxi Provincial Natural Science Foundation [grant number 20232BAB214012]; Ganpo Promising Talents Supporting Plan: Talent Development Project of Leading Academic and Technological Researchers in Key Disciplines [grant number 20232BCJ23099].

ORCID

Hui Guo http://orcid.org/0000-0001-9538-3312

References

[1] L.Y. Zhang, Z.R. Zhang, Q. Chen, C. Zhang, and L. Liu, *Microbe-induced pitting of Fe-based amorphous coating*. Intermetallics 154 (2023), pp. 107824–107834.
[2] T.J. Lin, H.H. Sheu, C.Y. Lee, and H.B. Lee, *The study of mechanical properties and corrosion behavior of the Fe-based amorphous alloy coatings using high velocity oxygen fuel spraying*. J. Alloys Compd. 867 (2021), pp. 159132–159141.

[3] L. Qiao, Y.P. Wu, S. Hong, J. Cheng, and Z. Wei, *Influence of the high-velocity oxygen-fuel spray parameters on the porosity and corrosion resistance of iron-based amorphous coatings*. Surf. Coat. Technol. 366 (2019), pp. 296–302.
[4] J. Wu, J.P. Cui, Q.J. Zheng, S.D. Zhang, W.H. Sun, B.J. Yang, and J.Q. Wang, *Insight into the corrosion evolution of Fe-based amorphous coatings under wet-dry cyclic conditions*. Electrochim. Acta 319 (2019), pp. 966–980.
[5] J. Farmer, J.S. Choi, C. Saw, J. Haslam, D. Day, P. Hailey, T. Lian, R. Rebak, J. Perepezko, J. Payer, D. Branagan, B. Beardsley, A. D'amato, and L. Aprigliano, *Iron-based amorphous metals: High-performance corrosion-resistant material development*. Metall. Mater. Trans. A 40 (2009), pp. 1289–1305.
[6] H. Guo, S.D. Zhang, W.H. Sun, and J.Q. Wang, *Differences in dry sliding wear behavior between HVAF-sprayed amorphous steel and crystalline stainless steel coatings*. J. Mater. Sci. Technol. 35 (2019), pp. 865–874.
[7] J.B. Cheng, S. Zhao, D. Liu, Y. Feng, and X.B. Liang, *Microstructure and fracture toughness of the FePSiB-based amorphous/nanocrystalline coatings*. Mat. Sci. Eng: A 696 (2017), pp. 341–347.
[8] Y. Wang, M.Y. Li, L.L. Sun, X.Y. Zhang, and J. Shen, *Environmentally assisted fracture behavior of Fe-based amorphous coatings in chloride-containing solutions*. J. Alloys Compd. 738 (2018), pp. 37–48.
[9] D.B. Wang, J. Wu, Q. Wang, L. Wan, W. Emori, S.D. Zhang, and J.Q. Wang, *Temperature-dependent corrosion behaviour of the amorphous steel in simulated wet storage environment of spent nuclear fuels*. Corros. Sci. 188 (2021), pp. 109529–109542.
[10] H. Guo, N.C. Wu, Y.L. Zhang, S.D. Zhang, W.H. Sun, and J.Q. Wang, *Influence of coating thickness on the impact damage mode in Fe-based amorphous coatings*. Surf. Coat. Technol. 390 (2020), pp. 125650–125665.
[11] S.D. Zhang, W.L. Zhang, S.G. Wang, X.J. Gu, and J.Q. Wang, *Characterisation of three-dimensional porosity in an Fe-based amorphous coating and its correlation with corrosion behaviour*. Corros. Sci. 93 (2015), pp. 211–221.
[12] D. Sivan, K. Satheesh Kumar, A. Abdullah, V. Raj, I.I. Misnon, S. Ramakrishna, and R. Jose, *Advances in materials informatics: A review*. J. Mater. Sci. 59 (2024), pp. 2602–2643.
[13] Y.X. Tang, C. Zhou, W.W. Wang, W.T. Zhang, and Y. Cheng, *Machine learning driven bond performance prediction between FRP bars and coral aggregate concrete*. Constr. Build. Mater. 442 (2024), pp. 137684–137699.
[14] Y.X. Tang, W.W. Wang, Q.D. Huang, Y. Cheng, and C. Zhou, *Shear performance prediction of RC beams shear-strengthened with FRP sheet: A machine learning driven design-oriented method*. Eng. Struct. 334 (2025), pp. 120240–120254.
[15] W.T. Zhang, W.W. Wang, Y.X. Tang, K. Sun, and C. Zhou, *Explainable machine learning driven strength degradation investigation of BFRP bar in seawater and sea sand concrete environment*. Structures 71 (2025), pp. 108205–108215.
[16] Y.T. Sun, H.Y. Bai, M.Z. Li, and W.H. Wang, *Machine learning approach for prediction and understanding of glass-forming ability*. J. Phys. Chem. Lett. 8 (2017), pp. 3434–3439.
[17] J. Xiong, S.Q. Shi, and T.Y. Zhang, *A machine-learning approach to predicting and understanding the properties of amorphous metallic alloys*. Mater. Design 187 (2020), pp. 108378–108392.
[18] G.N. Liu, S. Sohn, S.A. Kube, A. Raj, A. Mertz, A. Nawano, A. Gilbert, M.D. Shattuck, C.S. O'Hern, and J. Schroers, *Machine learning versus human learning in predicting glass-forming ability of metallic glasses*. Acta Mater. 243 (2023), pp. 118497–118507.
[19] X.W. Liu, Z.L. Long, L.M. Yang, W. Zhang, and Z. Li, *Prediction of glass forming ability in amorphous alloys based on different machine learning algorithms*. J. Non-Cryst. Solids 570 (2021), pp. 121000–121005.
[20] T. Long, Z. Long, and Z. Peng, *Rational design and glass-forming ability prediction of bulk metallic glasses via interpretable machine learning*. J. Mater. Sci. 58 (2023), pp. 8833–8844.
[21] Y. Zeng, Z. Tian, Q. Zheng, A. Bu, and Q. Xie, *Identifying key features for predicting glass-forming ability of bulk metallic glasses via interpretable machine learning*. J. Mater. Sci. 59 (2024), pp. 8318–8337.

[22] J. Gao, J.X. Hou, Y.T. Wu, B.T. Ji, D.B. Wang, K.Q. Qiu, J.H. You, and J.Q. Wang, *Machine learning-enabled design of Fe-based bulk metallic glasses for superior thermal neutron absorption properties*. J. Alloys Compd. 1010 (2025), pp. 177595–177604.
[23] Z. Li, Z.L. Long, S. Lei, and Y.L. Tang, *Machine learning driven rationally design of amorphous alloy with improved elastic models*. Mater. Design 220 (2022), pp. 110881–110892.
[24] S. Park, J.H. Fonseca, K.P. Marimuthu, C. Jeong, S. Lee, and H. Lee, *Determination of material properties of bulk metallic glass using nanoindentation and artificial neural network*. Intermetallics 144 (2022), pp. 107492–107502.
[25] Z. Li, Z.L. Long, S. Lei, L.M. Yang, W. Zhang, and T. Zhang, *Explicit expressions of the saturation flux density and thermal stability in Fe-based metallic glasses based on Lasso regression*. Intermetallics 139 (2021), pp. 107361–107372.
[26] X. Li, G.C. Shan, and C.H. Shek, *Machine learning prediction of magnetic properties of Fe-based metallic glasses considering glass forming ability*. J. Mater. Sci. Technol. 103 (2022), pp. 113–120.
[27] Y. Wang, Y.F. Tian, T. Kirk, O. Laris, J.H. Ross, R.D. Noebe, V. Keylin, and R. Arróyave, *Accelerated design of Fe-based soft magnetic materials using machine learning and stochastic optimization*. Acta Mater. 194 (2020), pp. 144–155.
[28] Z.C. Lu, X. Chen, X.J. Liu, D.Y. Lin, Y. Wu, Y.B. Zhang, H. Wang, S.H. Jiang, H.X. Li, X.Z. Wang, and Z.P. Lu, *Interpretable machine-learning strategy for soft-magnetic property and thermal stability in Fe-based metallic glasses*. npj Comput. Mater. 6 (2020), pp. 187–195.
[29] N. Zhang, A.N. He, G. Zhang, P. Cai, B.J. Zhang, Y.F. Ling, Y.Q. Dong, J.W. Li, Q.K. Man, and B.G. Shen, *Interpretable machine learning-assisted design of Fe-based nanocrystalline alloys with high saturation magnetic induction and low coercivity*. J. Mater. Sci. Technol. 188 (2024), pp. 73–83.
[30] C.C. Liu, X.D. Wang, W.D. Cai, and H. Su, *Prediction of magnetocaloric properties of Fe-based amorphous alloys based on interpretable machine learning*. J. Non-Cryst. Solids 625 (2024), pp. 122749–122757.
[31] Y.X. Zhang, S.J. Xie, W. Guo, J. Ding, L.H. Poh, and Z.D. Sha, *Multi-objective optimization for high-performance Fe-based metallic glasses via machine learning approach*. J. Alloys Compd. 960 (2023), pp. 170793–170803.
[32] C. Nam, *Convolutional neural network guided prediction of saturation magnetic flux density of Fe-based metallic glasses*. Comp. Mater. Sci. 225 (2023), pp. 112198–112207.
[33] X.W. Liu, Z.L. Long, and L. Peng, *Prediction of Vickers hardness of amorphous alloys based on interpretable machine learning*. J. Non-Cryst. Solids 602 (2023), pp. 122095–122103.
[34] H. Guo, W.H. Sun, W.Y. Lu, Q.H. Sun, M.S. Wang, and L.M. Xu, *Machine learning approach for predicting the fracture toughness of bulk metallic glasses*. Philos. Mag. 105 (2025), pp. 991–1005.
[35] C. Zhang, H. Zhou, and L. Liu, *Laminar Fe-based amorphous composite coatings with enhanced bonding strength and impact resistance*. Acta Mater. 72 (2014), pp. 239–251.
[36] J. Benesty, J.D. Chen, Y.T. Huang, and I. Cohen, *Noise Reduction in Speech Processing*, Springer, Berlin Heidelberg, 2009.
[37] X.Z. Jin, H. Luo, X.F. Wang, H.X. Cheng, C.H. Fan, X.G. Li, and X.B. Yan, *Data mining accelerated the design strategy of high-entropy alloys with the largest hardness based on genetic algorithm optimization*. MGE Adv. 2 (2024), pp. e49–e66.
[38] J.G. Hao and T.K. Ho, *Machine Learning Made Easy: A Review of Scikit-learn Package in Python Programming Language*. J. Educ. Behav. Stat. 44 (2019), pp. 348–361.
[39] B. Pang, E. Nijkamp, and Y.N. Wu, *Deep Learning With TensorFlow: A Review*. J. Educ. Behav. Stat. 45 (2019), pp. 227–248.
[40] H. Zou, *Comment: Ridge regression—still inspiring after 50 years*. Technometrics 62 (2020), pp. 456–458.
[41] J.O. Ogutu, T. Schulz-Streeck, and H.P. Piepho, *Genomic selection using regularized linear regression models ridge regression, lasso, elastic net and their extensions*. BMC Proc. 6 (2012), pp. S10–S15.
[42] M.A. Hearst, S.T. Dumais, E. Osuna, J. Platt, and B. Scholkopf, *Support vector machines*. IEEE Intell. Syst. Appl. 13 (1998), pp. 18–28.

[43] Y.Q. Zhang, G. Cao, B.S. Wang, and X.S. Li, *A novel ensemble method for k-nearest neighbor*. Pattern Recogn. 85 (2019), pp. 13–25.
[44] M. Xu, P. Watanachaturaporn, P.K. Varshney, and M.K. Arora, *Decision tree regression for soft classification of remote sensing data*. Remote Sens. Environ. 97 (2005), pp. 322–336.
[45] P. Geurts, D. Ernst, and L. Wehenkel, *Extremely randomized trees*. Mach. Learn. 63 (2006), pp. 3–42.
[46] V.L. Deringer, A.P. Bartók, N. Bernstein, D.M. Wilkins, M. Ceriotti, and G. Csányi, *Gaussian process regression for materials and molecules*. Chem. Rev. 121 (2021), pp. 10073–10141.
[47] L. Breiman, *Bagging predictors*. Mach. Learn. 24 (1996), pp. 123–140.
[48] N. Duffy and D. Helmbold, *Boosting methods for regression*. Mach. Learn. 47 (2002), pp. 153–200.
[49] M.W. Gardner and S.R. Dorling, *Artificial neural networks (the multilayer perceptron)—A review of applications in the atmospheric sciences*. Atmo. Senviron. 32 (1998), pp. 2627–2636.
[50] L.J. Wu, X. Li, J.D. Yuan, and S.J. Wang, *Real-time prediction of tunnel face conditions using XGBoost Random Forest algorithm*. Front. Struct. Civ. Eng. 17 (2024), pp. 1777–1795.
[51] A. Natekin and A. Knoll, *Gradient boosting machines, a tutorial*. Front. Neurorobot. 7 (2013), pp. 1–21.
[52] J.O. Rawlings, S.G. Pantula, and D.A. Dickey, *Applied Regression Analysis a Research Tool*, Springer, New York, 1998.
[53] J. Xiong, S.Q. Shi, and T.Y. Zhang, *Machine learning of phases and mechanical properties in complex concentrated alloys*. J. Mater. Sci. Technol. 87 (2021), pp. 133–142.
[54] P. Gong, Z. Wang, M.J. Li, G.Q. Yu, L. Deng, X.F. Tang, and X. Wang, *A machine learning framework to predict thermoplastic deformation behavior and rheological regime transition in bulk metallic glass composites*. Intermetallics 181 (2025), pp. 108727–108735.
[55] M.W. Hu, Q.Y. Tan, R. Knibbe, M. Xu, B. Jiang, S. Wang, X. Li, and M.X. Zhang, *Recent applications of machine learning in alloy design: A review*. Mat. Sci. Eng: R 155 (2023), pp. 100746–100774.
[56] W. Muhammad, A.P. Brahme, O. Ibragimova, J.D. Kang, and K. Inal, *A machine learning framework to predict local strain distribution and the evolution of plastic anisotropy & fracture in additively manufactured alloys*. Int. J. Plastic. 136 (2021), pp. 102867–102895.

Philosophical Magazine

ISSN: 1478-6435 (Print) 1478-6443 (Online) Journal homepage: www.tandfonline.com/journals/tphm20

An intelligent screening for rare earth in Ni alloy based on machine learning and multi-objective optimisation

Zengyi Zhong, Xianggang Wu, Yongzhi Huang, Lan Luo & Yong Liu

To cite this article: Zengyi Zhong, Xianggang Wu, Yongzhi Huang, Lan Luo & Yong Liu (2025) An intelligent screening for rare earth in Ni alloy based on machine learning and multi-objective optimisation, Philosophical Magazine, 105:17, 973-990, DOI: 10.1080/14786435.2025.2467873

To link to this article: https://doi.org/10.1080/14786435.2025.2467873

PHILOSOPHICAL MAGAZINE
2025, VOL. 105, NO. 17, 973–990
https://doi.org/10.1080/14786435.2025.2467873

Taylor & Francis
Taylor & Francis Group

An intelligent screening for rare earth in Ni alloy based on machine learning and multi-objective optimisation

Zengyi Zhong[a], Xianggang Wu[a], Yongzhi Huang[a], Lan Luo[a,b] and Yong Liu[b]

[a]School of Physics and Materials Science, Nanchang University, Nanchang, People's Republic of China; [b]Jiangxi Key Laboratory of Light Alloy, Nanchang University, Nanchang, People's Republic of China

ABSTRACT

Rare earth (abbreviated as ***RE, RE = Sc, Y, La∼Lu***) doped Nickel alloy is a new candidate for its good neutron shielding applications. This new alloy still requires a systemic understanding of RE role in Ni alloy mechanical properties. Neural network model (CNN) machine learning was then performed to quantitatively assess the material paraments of Ni-RE solid solution in this work. The obtained composition-dependent lattice (***a***), shear moduli (***G***) and average misfit factor (ε) were employed to analyze the solid solution strengthening (SSS) effect based on Labusch model (τ_{CRSS}). While, solid-solution toughening was evaluated by shear moduli (***G***) and Poisson ratio (***v***) with the help of Peierls-Nabbaro model ($\tau_{P\text{-}N}$). It is found Ni-RE solid solution would leads strengthening and toughening effects. Furthermore, strengthening and toughening effect are both more obvious when RE concentration (***RE%***) is larger or RE atomic radius (r_{1RE}) is larger ($\tau_{CRSS}\uparrow$and $\tau_{P\text{-}N}\downarrow$ as ***RE%***$\uparrow$ or $r_{1RE}\uparrow$). Considering the both objective optimisation and comparing with the other elements in periodic table, RE should been used as minor alloying element in Ni-based alloy and ***La, Ce, Gd, Tb*** would been chosen out among RE. The work makes a more complete understanding and less computational cost of the solid solution effect of alloying element on Ni alloy. The work also suggests a consistent and efficient material discovery by a new theorical strategy.

ARTICLE HISTORY
Received 4 July 2024
Accepted 11 February 2025

KEYWORDS
Rare earth doped nickel alloy; solid-solution; machine learning; strengthen; toughen

1. Introduction

The nuclear industry demands a lot for spent fuel storage materials [1,2]. Rare earth (abbreviated as RE, RE = Sc, Y, La ∼ Lu) doped nickel alloys is presently proposed as a good candidate [3–6] for the excellent neutron shielding property [7,8]. The alloy also has a high strength [9] by the full use of precipitation strengthening and solid solution strengthening (SSS). Nuclear Regulatory

CONTACT Lan Luo luolan1190@163.com School of Physics and Materials Science, Nanchang University, Nanchang 330031, People's Republic of China; Jiangxi Key Laboratory of Light Alloy, Nanchang University, Nanchang 330031, People's Republic of China

Commission had authorised its usage in the Yucca Mountain Nuclear Waste Project [10,11].

RE-intermetallic precipitation influence has been exploited a lot [12–14]. While, the strength enhancement relying on RE solid should also be done. The SSS effect has been revealed as hindering dislocation motion due to the lattice misfit or modulus misfit between the solute and the matrix [15–18]. The solute atoms in the glide plane are considered as independent point obstacles pinning the dislocations in the strong-pinning model for moderately dilute alloy at 0 K proposed by Friedel [19] and Fleischer [20]. The weak pinning model, considered ambient temperatures (T > 78 K) at real solute concentrations ($c > 10^{-4}$), is presented by Labusch [21] with certain material parameters as inputs to make quantitative prediction of SSS effect, such as the lattice constant ($\boldsymbol{a}$), shear modulus ($\boldsymbol{G}$), misfit factor ($\boldsymbol{\varepsilon}$). Furthermore, the toughening ability could be assessed with Peierls-Nabarro model [22] by shear modulus ($\boldsymbol{G}$) and Poisson ratio ($\boldsymbol{\nu}$) as inputs. Although, High-throughput first principal calculation makes it possible to obtain the solid solution material parameters more efficiently by the assumption for material parament is as the linear function of the concentration [15]. It is still difficult to get the exactly material parameter when at every concertation point considering computing workload. Now machine learning (ML) [23–28] could substantially facilitate the DFT computations and active learning as the optimal design, and the active learning means that a surrogate model is trained from a given dataset (either from experiments or from calculation) and the obtained data is added to the original dataset and then the surrogate model is updated. The process is repeated iteratively so that the predictive performance is improved quickly and the result would be more accurate at arbitral customer rang.

In this paper, the most suitable solid-solution RE in *fcc*-Ni alloy is selected by considering strengthening and toughening effect. The needed material parameter inputs (as $\boldsymbol{a}$, $\boldsymbol{G}$, $\boldsymbol{\nu}$, $\boldsymbol{\varepsilon}$) are obtained by machine learning with the sample dataset made by high throughput first principal calculation. RE solid solution effect were further compared with the other elements in periodic table. The work makes a more complete understanding of the solid solution effect of alloying element in Ni alloy. It also provides an automated, unified, systematical, and powerful method for materials screening and discovery.

2. Machine learning procedure

2.1. Sample dataset

High-throughput first-principal calculations were carried out by our former work [29] to make the sample dataset. The equilibrium lattice constants ($\boldsymbol{a}$) were evaluated by adopting the workflow that computes and then fits the energy-volume relation of the solid solution models to the Birch–Murnaghan

equation of state (EOS) [30]. The elastic constants [31] were gotten by the computed energy-strain relation to polynomial functions and the average shear modulus (***G***) and Poisson's ratio (***v***) were estimated by the Voigt-Reuss-Hill (VRH) scheme [32]. The first-principles calculation was done by Vienna ab initio simulation package (VASP) [33] based on density functional theory (DFT) [34] with the projector augmented wave (PAW) [35] The spin-polarised generalised gradient approximation (GGA) in the form of Perdew–Burke–Ernzerhof (PBE) [36] was employed for the exchange–correlation energy. ***Ni*** $(3d^8 4s^2)$, ***Sc*** $(3d^1 4s^2)$, ***Y*** $(4d^1 5s^2)$, ***La ∼ Lu*** $(4f^n 5d^{0/1} 6s^2,\ n = 0 \sim 14)$ [37,38] were treated as valence electrons. The special GGA potential were supplied for ***Ce ∼ Lu*** just as Ref. [39], in which ***f***-electrons are kept frozen in the core. The Brillouin zone was sampled with Monkhorst–Pack scheme [40] using the K-points grid of $7 \times 7 \times 7$ for solid solution supercells. The cut-off energy for plane waves was *500 eV*. The convergence criteria of self-consistence were 10^{-7} *eV/atom* for the total energy and *0.01 eV/Å* for the atomic forces. The supercell containing 32 atoms (Ni31RE) was adopted to model the fcc-Ni based solid solution. The data other than those for Ni31RE were coming from Ref. [15] (The substitution was realised by the recipes of Monte Carlo special quasi-random structure (MCSQS) within the ATAT codes and 4 different concentrations were considered, and namely Ni31RE (1/32), Ni30RE2 (2/32), Ni29RE3 (3/32), and Ni28RE4 (4/32), respectively). The sample datasets were as list in Table 1.

2.2. Machine learning algorithm

Adaptive Boosting (Adaboost), Support Vector Machine (SVM), Random Forest (RF), Bayesian Regression (BR) and Convolutional Neural Network (CNN) were recommended at the very beginning (Figure 1).

Table 1. Sample datasets for *G, v, a* of Ni-RE solid solution.

	G (Gpa)	*v*	*a* (Å)		*G* (Gpa)	*v*	*a* (Å)
Ni_{32}	93.25	0.297	3.5140	Ni31Tm	81.07	0.308	3.5550
Ni31Sc	86.88	0.301	3.5390	Ni31Yb	81.92	0.303	3.5440
Ni31Y	78.94	0.310	3.5600	Ni31Lu	81.68	0.306	3.5545
Ni31La	70.31	0.323	3.5700	Ni31Sc*	89.80	0.301	3.5479
Ni31Ce	69.05	0.326	3.5580	Ni31Y*	81.10	0.310	3.5694
Ni31Pr	71.10	0.323	3.5740	Ni31La*	74.30	0.324	3.5771
Ni31Nd	72.92	0.319	3.5715	Ni30Sc2*	80.70	0.305	3.5738
Ni31Pm	74.20	0.318	3.5690	Ni30Y2*	66.70	0.323	3.6158
Ni31Sm	75.04	0.316	3.5670	Ni30La2*	55.50	0.351	3.6343
Ni31Eu	77.85	0.309	3.5500	Ni29Sc3*	76.00	0.309	3.6012
Ni31Gd	77.16	0.313	3.5625	Ni29Y3*	56.50	0.336	3.6654
Ni31Tb	78.23	0.312	3.5610	Ni29La3*	31.60	0.377	3.6970
Ni31Dy	78.93	0.311	3.5590	Ni28Sc4*	66.50	0.313	3.6288
Ni31Ho	79.64	0.310	3.5580	Ni28Y4*	18.40	0.354	3.8229
Ni31Er	80.46	0.309	3.5565	Ni28La4*	44.60	0.394	3.8440

Data marked with * is from Ref. [15], and the other data are from our former work Ref. [29].

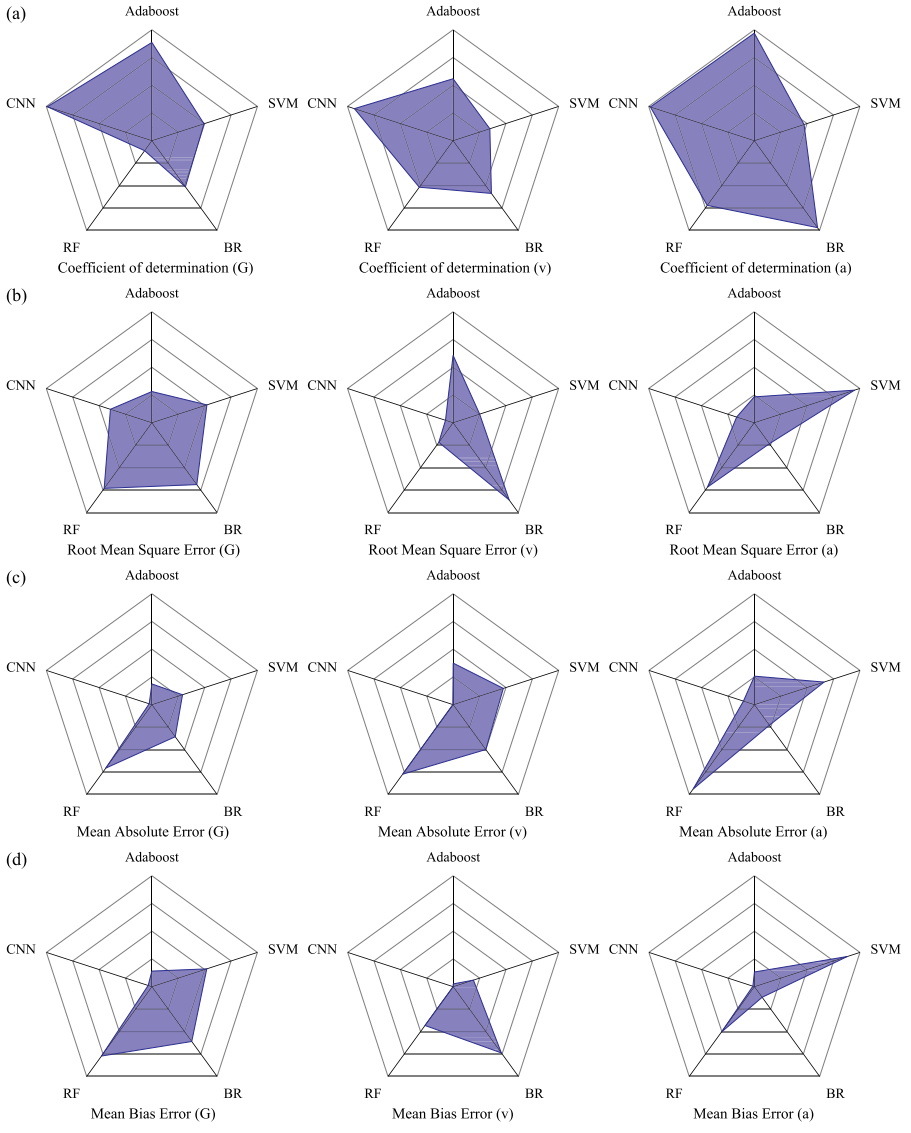

Figure 1. (a) Coefficient of determination (R^2) (b) Root Mean Square Error (RMSE) (c) Mean Absolute Error (MAE) (d) Mean Bias Error (MBE) for the different algorithmic models.

The performance function as Coefficient of determination (***R²***), Root Mean Square Error (***RMSE***), Mean Absolute Error (***MAE***) and Mean Bias Error (***MBE***) [41,42] were obtained from Equations (1)–(4).

$$R^2 = 1 - \frac{\sum_{i=1}^{N} (y_i - y_r)}{\sum_{i=1}^{N} (y_i - y_a)^2} \tag{1}$$

$$RMSE = \sqrt{\frac{1}{N} \sum_{i=1}^{N} \frac{(y_i - y_r)^2}{y_i^2}} \tag{2}$$

$$MAE = \frac{1}{N}\sum_{i=1}^{N}|y_i - y_r| \tag{3}$$

$$MBE = \frac{1}{N}\sum_{i=1}^{N}(y_i - y_r) \tag{4}$$

In which, $\boldsymbol{N}$ was the number of training/test sets, $\boldsymbol{y_i}$ was the actual value of the initial dataset, $\boldsymbol{y_r}$ was the predicted value, and $\boldsymbol{y_a}$ was the initial average value. The more nearby $\boldsymbol{R^2}$ value was to *1*, or the smaller ***RMSE/MAE/MBE*** value is, the better ML model was [43]. The data (in Table 1) were randomly divided into training-dataset and test-dataset with the ratio of *9:1*. The process was repeated *50* times, the average $\boldsymbol{R^2}$, ***RMSE***, ***MAE*** and ***MBE*** for above mentioned algorithm were shown in Figure 2. CNN had the best performance, for example exhibiting the lowest $\boldsymbol{R^2}$ for $\boldsymbol{G}$, $\boldsymbol{v}$, $\boldsymbol{a}$ comparing with Adaboost, SVM, BR, RF and CNN (*0.9542*, *0.7974*, *0.8056*, *0.6445* and *0.9961*; *0.8232*, *0.7392*, *0.8350*, *0.8073* and *0.9741*; *0.9879*, *0.7885*, *0.9875*, *0.8883* and *0.9939*). Therefore, CNN was chosen in the following work.

2.3. Feature engineering interpretability

A series of Feature would be considering their relevance. Features should be figured out when they have the Pearson high correlation coefficient ($\boldsymbol{p}$) [44],

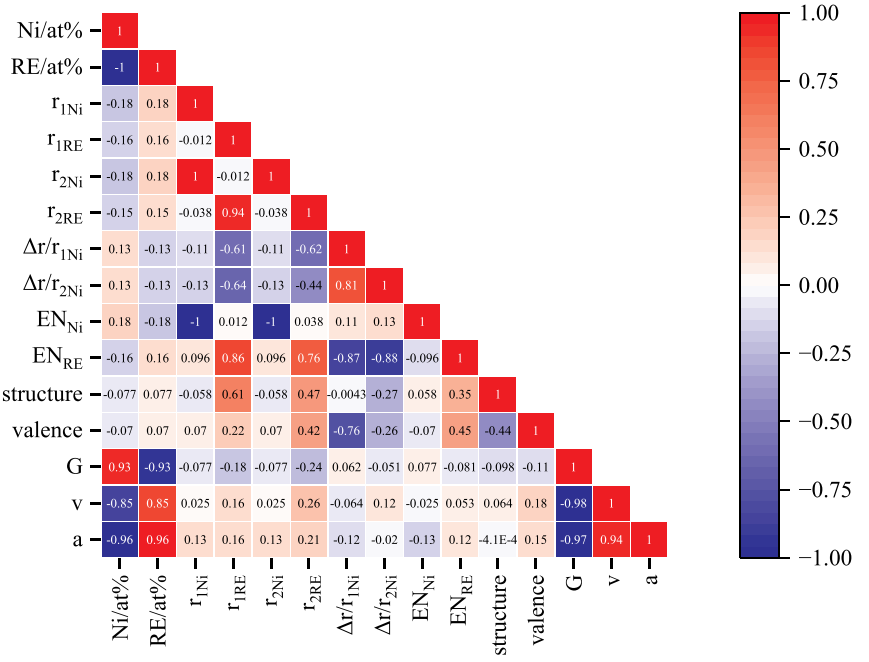

Figure 2. Pearson correlation coefficient heat map for the features of Ni-RE solid solutions.

just as Equation (5).

$$p_{X,Y} = \frac{Cov(X, Y)}{\sigma_X \sigma_Y} \tag{5}$$

In which, $\boldsymbol{\sigma_x}$ denoted the standard deviation of **X**, $\boldsymbol{\sigma_Y}$ was the standard deviation of Y, and ***Cov(X, Y)*** represented the covariance of the two. Nickel atomic percentage (***Ni%***), rare earth atomic percentage (***RE%***), nickel atom radius ($\boldsymbol{r_{1Ni}}$), nickel ion radius ($\boldsymbol{r_{2Ni}}$), rare earth atom radius ($\boldsymbol{r_{1RE}}$), rare earth ion radius ($\boldsymbol{r_{2RE}}$), atomic radius difference ($\boldsymbol{\Delta r/r_{1Ni}}$), ionic radius difference ($\boldsymbol{\Delta r/r_{2Ni}}$), RE electronegativity ($\mathbf{EN_{RE}}$), Ni electronegativity ($\mathbf{EN_{Ni}}$), crystal system for single phase (**structure**), Shear modulus for solid solution (***G***), Poisson's ratio for solid solution (***v***) and lattice constant for solid solution (***a***) were considered for the covariance in Figure 2. The correlations between the four input features (***Ni%***, ***RE%***, $\boldsymbol{r_{1Ni}}$, $\boldsymbol{r_{1RE}}$) and the three output features (***G***, ***v***, ***a***) were extremely high.

The above *4* input features (***Ni%, RE%,*** $\boldsymbol{r_{1Ni}}$, $\boldsymbol{r_{1RE}}$) were then chosen in CNN to predicting 3 out features (***G***, ***v***, ***a***). Figure 3 show the training results. $\boldsymbol{R^2}$ values for ***G***, ***v*** and ***a*** were *0.99963, 0.99935* and *0.99983,* respectively. ***RMSE*** values were *0.00189*, *0.000461* and 0.000067. ***MAE*** values were *0.15236*, *0.000061* and *0.000241*. ***MBE*** values were *0.04412*, *0.000009* and *0.000002*.

Then *4* input features (***Ni%, RE%,*** $\boldsymbol{r_{1Ni}}$, $\boldsymbol{r_{1RE}}$, Figure 2) were then chosen in CNN machine learning (Figure 1) to predicting 3 out features (***G***, ***v***, ***a***) for Ni-RE (RE = ***Sc, Y, La ~ Lu***) solid solution with the atomic percentage concertation range *0 ~ 3at%* at intervals of *0.1at%* based on high-throughput first-principal calculation sample dataset (Table 1).

3. Results and discussion

3.1. Material parameters (G, v, a, ε) of Ni-RE solid solutions

Figure 4 shows ML predicting results of ***G***, ***v***, ***a*** for Ni-RE (RE = **Sc, Y, La ~ Lu**) solid solution in RE concertation range *0 ~ 3at%* at intervals of *0.1at%*. Green–blue colour means the material parameter value at the right point for Ni-RE solid solution would be less than that for pure Ni. Orange-red colour means

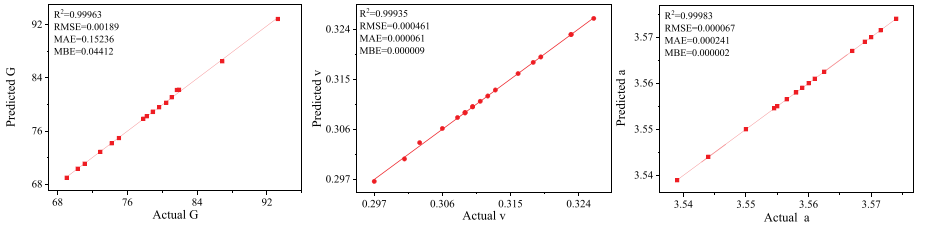

Figure 3. Machine learning training fittings for *G, v, a* of Ni-RE solid solutions.

the material parameter value at the right point for Ni-RE solid solution would be larger than that for pure Ni.

ML gives out the results as shear modulus ($G_{Ni\text{-}RE} = 70.5543 \sim 92.9821$ GPa, $G_{Ni} = 92.9834$ Gpa), Poisson's ratio ($\nu_{Ni\text{-}RE} = 0.2972 \sim 0.3243$, $\nu_{Ni} = 0.2971$) and lattice constant ($a_{Ni\text{-}RE} = 3.5097 \sim 3.5707$ Å, $a_{Ni} = 3.5148$ Å) for Ni-RE (RE = **Sc, Y, La ~ Lu**) solid solution in RE concertation range $0 \sim 3at\%$ at intervals of $0.1at\%$. G decrease but ν, and a increase as r_{1RE} roses (from ***La*** to ***Lu*** except ***Eu*** and ***Yb*** gradually changes from *187.9 pm to 173.5 pm*, except $r_{Eu} = 193.9\ pm$, $r_{Yb} = 204.2\ pm$ [45]**).** The trend ($G\downarrow\nu\uparrow a\uparrow$ *as* $r_{1RE}\uparrow$) is clearly shown by the upper strip in every plot, which represents for Ni31RE supper cell by high-though first principal calculation (*3.125at%*). While the trend at low RE concertation is not so obvious, as shown by the down strip in every plot (*0.1at%* RE concertation by machine learning). Furthermore, G decreases but ν, a increase as RE concertation roses in Ni-RE solid solution $G\downarrow\nu\uparrow a\uparrow$ *as* ***RE%***↑, Ni-**Gd** solid solution result for G, ν, a also proves it as showing in Figure 5.

The lattice misfit factor ε_b $\left(\varepsilon_b = \frac{1}{a_0}\left(\frac{da}{dc}\right)_{c=0}\right)$, modulus misfit factor ε_s $\left(\varepsilon_s = \frac{1}{G_0}\left(\frac{dG}{dc}\right)_{c=0}\right)$ could be gotten by tangent near RE concertation = 0 (RE % = 0) from Figure 5. Then misfit factor ε_i $\varepsilon_i = \left[\left(\frac{\varepsilon_s}{1+0.5|\varepsilon_s|}\right)^2 + (\beta_i\varepsilon_b)^2\right]^{\frac{1}{2}}$ [51] could finally be gotten (in which β_i is a constant related to the type of dislocation, with a value of 16 for edge dislocation and 3 for screw dislocation for Ni alloy [46]) The average ε would be obtained by considering both dislocations ($\varepsilon = \frac{\varepsilon_{edge} + \varepsilon_{screw}}{2}$).

As shown in Figure 6(a,b), ε_b changes in an opposite way as ε_S when RE atomic radius(r_{1RE}) changes. The average ε changes more like ε_b ($\varepsilon\downarrow\varepsilon_b\downarrow$as $r_{1RE}\downarrow$, Figure 6(c)) because contribution value $\beta(\varepsilon_b/\varepsilon)$ is greater than critics as $\frac{1}{\sqrt{2}} \approx 0{:}71$, in Figure 6(d).

3.2. Strengthening/toughening evaluation of Ni-RE solid solutions

Solid solution strengthening (SSS) is important for improving strength in alloys [47]. Labusch model would be generally adopted for showing good agreement with experimental observations [48–51], and it applies in this work. The excess strength ($\Delta\sigma_{SSS}$) gained by SSS depends on the misfit factor (ε, Table 2), solute concentration (c, ***0 ~ 0.3at%***) and Shear modulus for solid solution (G, Figure 4), just as Eq.6 [21].

$$\Delta\sigma_{sss} = 3ZG\varepsilon^{\frac{4}{3}}c^{\frac{2}{3}} \tag{6}$$

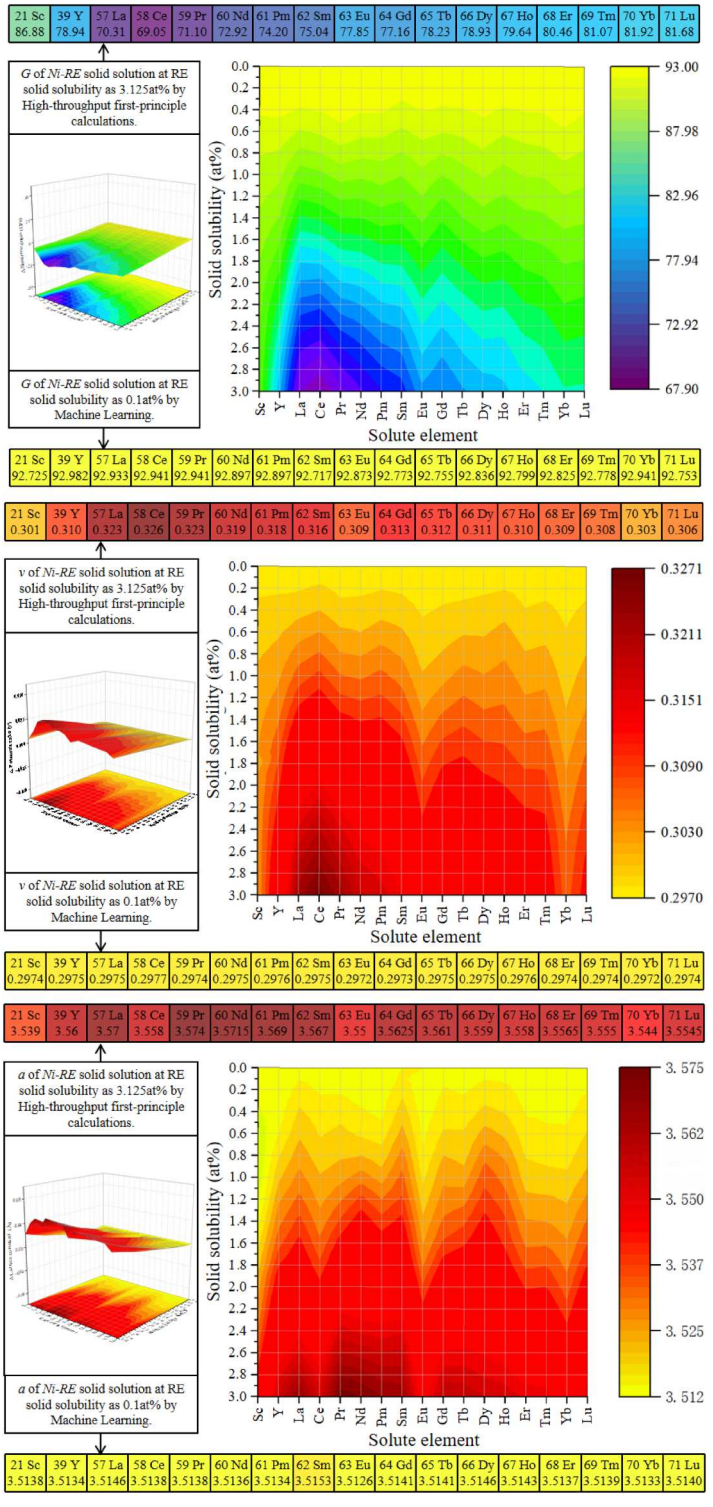

Figure 4. Material parameter *(G, v, a) plot* of Ni-RE (RE = *Sc, Y, La ~ Lu*) solid solutions with the atomic percentage concertation range 0~3% at intervals of 0.1% by ML.

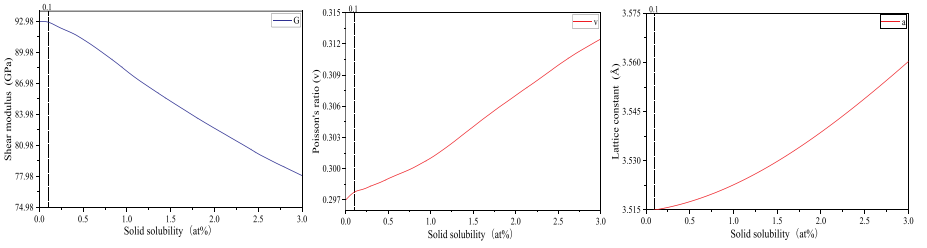

Figure 5. Material parameters (G, v, a) of Ni-Gd solid solution with different Gd concentration by ML (data draw from Figure 4).

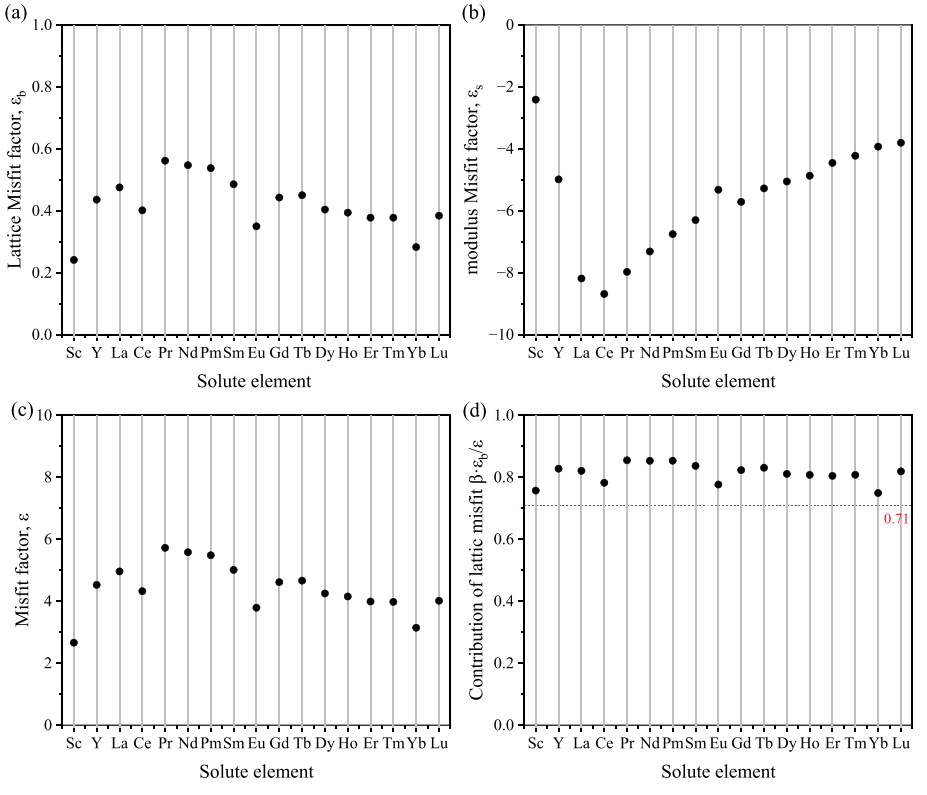

Figure 6. ε_b, ε_s, ε and $\beta\varepsilon_b/\varepsilon$ for Ni-RE solid solution based on ML result.

In which $\boldsymbol{Z}$ is a constant that depends on the solute element, assessing as 0.002 for Ni-RE solid solution [15].

A bigger $\boldsymbol{\varepsilon}$, a bigger $\boldsymbol{G}$, and a higher $\boldsymbol{c}$ would lead to a better solid solution strengthening ability. Figure 7 shows $\boldsymbol{\Delta\sigma sss}$ for ***Ni-RE*** solid solution with the atomic percentage concertation range $0 \sim 3at\%$ at intervals of $0.1at\%$. $\boldsymbol{\Delta\sigma sss}$ is about $20.528 \sim 57.1743$MPa at RE concentration = $0.1at\%$, which is about 1/10 time as that at high concentration ($3.125at\%$). Nonetheless, $\boldsymbol{\varepsilon}$ increase

Table 2. Misfit factors of Ni-RE solid solution by ML.

	ε_b	ε_s	ε_{edge}	ε_{screw}	ε	$\beta(\varepsilon_b/\varepsilon)$
Ni-Sc	0.241.	−2.413	4.013	1.311	2.662	0.757
Ni-Y	0.436	−4.987	7.120	1.936	4.528	0.828
Ni-La	0.475	−8.186	7.771	2.148	4.960	0.821
Ni-Ce	0.401	−8.687	6.625	2.023	4.324	0.782
Ni-Pr	0.561	−7.973	9.124	2.322	5.723	0.855
Ni-Nd	0.547	−7.315	8.890	2.271	5.581	0.853
Ni-Pm	0.538	−6.753	8.738	2.232	5.485	0.853
Ni-Sm	0.486	−6.300	7.918	2.104	5.011	0.837
Ni-Eu	0.350	−5.321	5.785	1.793	3.789	0.777
Ni-Gd	0.443	−5.713	7.239	1.990	4.614	0.823
Ni-Tb	0.450	−5.278	7.347	1.982	4.664	0.831
Ni-Dy	0.404	−5.056	6.621	1.877	4.249	0.811
Ni-Ho	0.394	−4.869	6.458	1.845	4.152	0.808
Ni-Er	0.377	−4.455	6.196	1.785	3.990	0.805
Ni-Tm	0.378	−4.225	6.192	1.768	3.980	0.808
Ni-Yb	0.283	−3.930	4.713	1.574	3.143	0.749
Ni-Lu	0.384	−3.806	6.286	1.746	4.016	0.819

but $\boldsymbol{G}$ decreases as $\boldsymbol{r_{1RE}}$ rosing (Figure 6(d) and Figure 4). $\boldsymbol{\Delta\sigma_{sss}}$ changing trend is more in the way as $\boldsymbol{\varepsilon}$. ($\boldsymbol{\Delta\sigma_{sss}}\uparrow$as $\boldsymbol{RE\%}\uparrow$or $\boldsymbol{r_{1RE}}\uparrow$).

When temperature effect is taken into account, critical resolved shear stress (τ_{CRSS}) is a better modification and could be given as Equation (7) [52]

$$\tau_{CRSS} = \Delta\sigma_{sss} e^{-mk_B T/w_0} \tag{7}$$

in which $\boldsymbol{m}$ is ***25***, $\boldsymbol{k_B}$ is Boltzmann constant, $\boldsymbol{T}$ is 1/3 of alloy melting temperature (T_{Ni} = 573 K), and $\boldsymbol{W_0}$ is the binding energy of the edge-localised segments

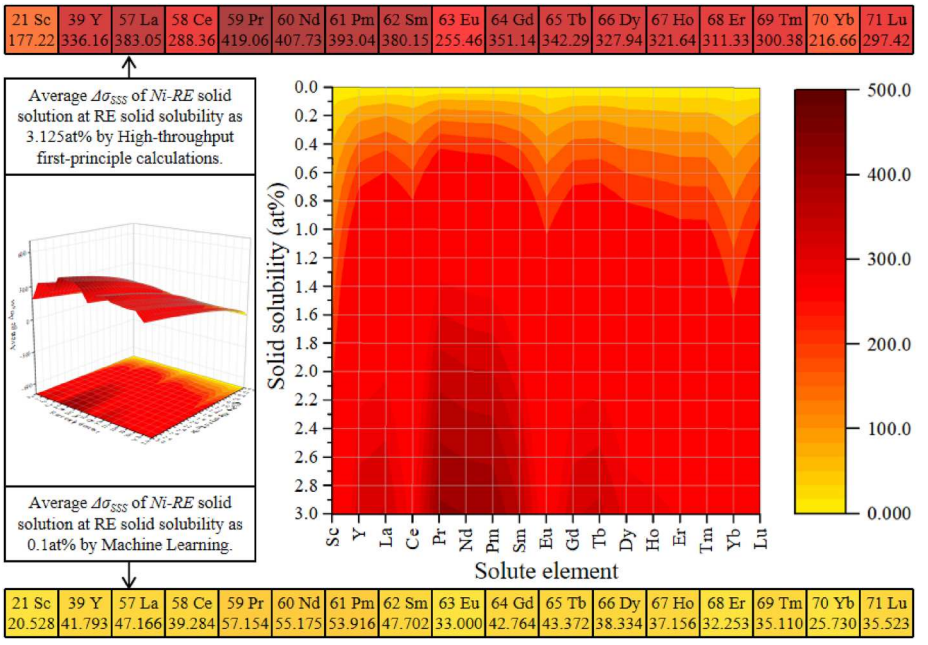

Figure 7. Solid-solution strengthening ability $\Delta\sigma_{sss}$ of Ni-RE solid solutions.

to the nearby solute atoms ($W_{0,573K,\ Ni} = 1.5\times10^{-19}$ J, according to Ref. [15]). $\boldsymbol{\tau_{CRSS}}$ increase as RE atomic radius $\boldsymbol{r_{1RE}}$ roses in Ni-RE solid solution (from ***La*** to ***Lu*** gradually changes except ***Eu*** and ***Yb).*** The trend ***(***$\boldsymbol{\tau_{CRSS}}\uparrow$ as $\boldsymbol{r_{1RE}}\uparrow$***)*** is clearly shown by the upper strip in every plot, which represents for Ni31RE supper cell by high-though first principal calculation*(3.125at%)*. While the trend at low *RE* atomic concentration ***RE%*** is not so obvious, as shown by the down strip *(0.1at%* RE concertation by machine learning). $\boldsymbol{\tau_{max}}$ varies from *5.4954* to *15.2997* MPa at ***RE%*** = *0.1at%*, which is about 1/10 time as that at high concentration (*3.125at%*) shown in Figure 8. The higher ***RE%*** is, the larger strengthening potentials, and the more strengthening effect is. $\boldsymbol{\tau_{CRSS}}$ changes in the same way as $\boldsymbol{\Delta\sigma_{sss}}$ ***(***$\boldsymbol{\tau_{CRSS}}\uparrow$as ***RE%***$\uparrow$or $\boldsymbol{r_{1RE}}\uparrow$***)***.

Deformation is usually realised by slipping, twinning, and rotating. Slipping is the most common mechanism. In the absence of thermal activation or quantum vibration of atoms, Peierls-Nabbaro stress ($\boldsymbol{\tau_{P\text{-}N}}$) is the maximum lattice resistance to rigid and irreversible dislocation glide in a specific slip system. So $\boldsymbol{\tau_{P\text{-}N}}$ could be used to determine the deformation easiness and described as Equation (8) [53].

$$\tau_{P-N} = \frac{2G}{1-\nu} exp\left(-\frac{2\pi}{1-\nu}\cdot\frac{d}{b}\right) \tag{8}$$

In which, ***G*** is the shear modulus, ***ν*** is the Poisson's ratio, and ***d*** is the interspacing between slip planes ($d = a_{Ni(111)} = 2.0288$ *Å*, according to Ref. [29]), ***b*** is the

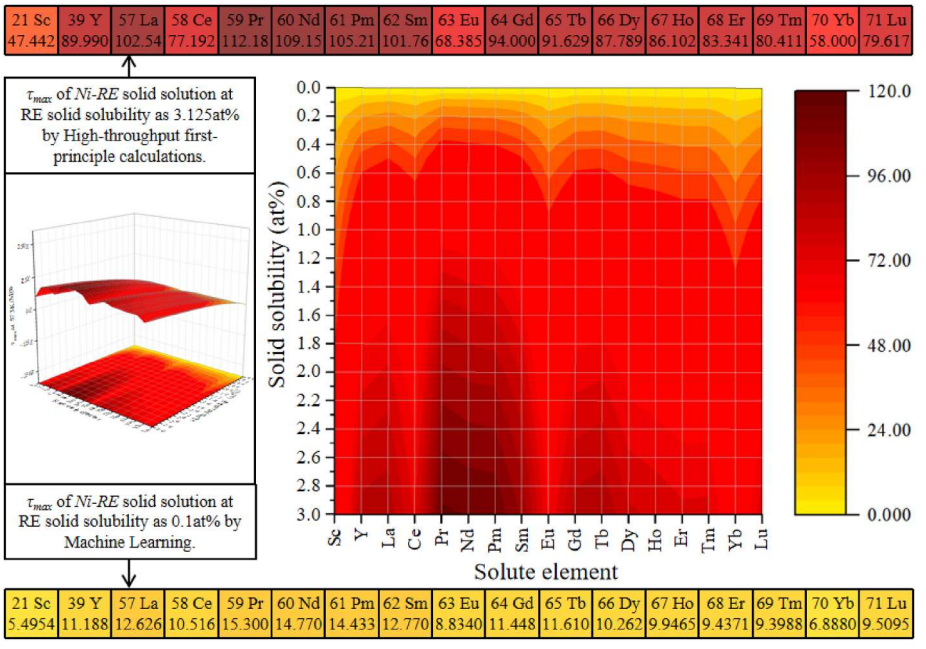

Figure 8. Strengthening effect (τ_{CRSS}) of Ni-RE solid solutions at 573 K.

length of the Burgers vector ($b = a/2_{\mathrm{Ni},(10\text{-}1)} = 1.4345$, according to Ref. [29]). Figure 9 shows toughening potential ($\boldsymbol{\tau_{P\text{-}N,\ Ni\text{-}RE}} = 0.40593 \sim 0.85551\ MPa$, $\boldsymbol{\tau_{P\text{-}N,Ni}} = 0.86104\ Mpa$). $\boldsymbol{\tau_{T-N}}$ decrease as RE atomic radius roses in Ni-RE solid solution (from ***La*** to ***Lu*** gradually changes except ***Eu*** and ***Yb).*** The trend ($\boldsymbol{\tau_{T-N}}\downarrow$ *as* $\boldsymbol{r_{1RE}}\uparrow$) is clearly shown by the upper strip in every plot, which represents for Ni31RE supper cell by high-though first principal calculation. While the trend at low RE concertation is not so obvious, as shown by the down strip (*0.1at%* RE concertation by machine learning). $\boldsymbol{\tau_{P\text{-}N}}$ varies from $0.84651 \sim 0.85551\ Mpa$ MPa at RE concentration = *0.1at%*, which is about 2 times as that at high concentration (*3.125at%*). The higher RE concentration is, the less $\boldsymbol{\tau_{P\text{-}N}}$ is and the better toughening effect is. It could be concluded that $\boldsymbol{\tau_{P\text{-}N}}$ decreases as RE% or $\boldsymbol{r_{1RE}}$ rosing ($\boldsymbol{\tau_{P\text{-}N}}\downarrow$as ***RE%***$\uparrow$or $\boldsymbol{r_{1RE}}\uparrow$).

Ni-RE solid solution could both strengthen and toughen Ni alloy, which could increase $\boldsymbol{\tau_{CRSS}}$ and decreases $\boldsymbol{\tau_{P\text{-}N}}$. Moreover, the trend as $\boldsymbol{\tau_{CRSS}}\uparrow$, $\boldsymbol{\tau_{P\text{-}N}}\downarrow$would be more obvious as RE% roses up the trend as $\boldsymbol{\tau_{CRSS}}\uparrow$, $\boldsymbol{\tau_{P\text{-}N}}\downarrow$would also be more obvious as $\boldsymbol{r_{1RE}}$ roses (from ***La*** to ***Lu*** except ***Eu*** and ***Y***). So, La, Ce, Gd, Tb would been chosen out as the most suitable elements among RE.

3.3. Comparison between Ni-M solid solution and Ni-RE solid solution

The composition-dependent shear modulus(***G***), Poisson's ratio (***ν***) and lattice constants (***a***) of Ni-RE solid solutions (RE = ***Sc, Y, La ∼ Lu***, with the atomic

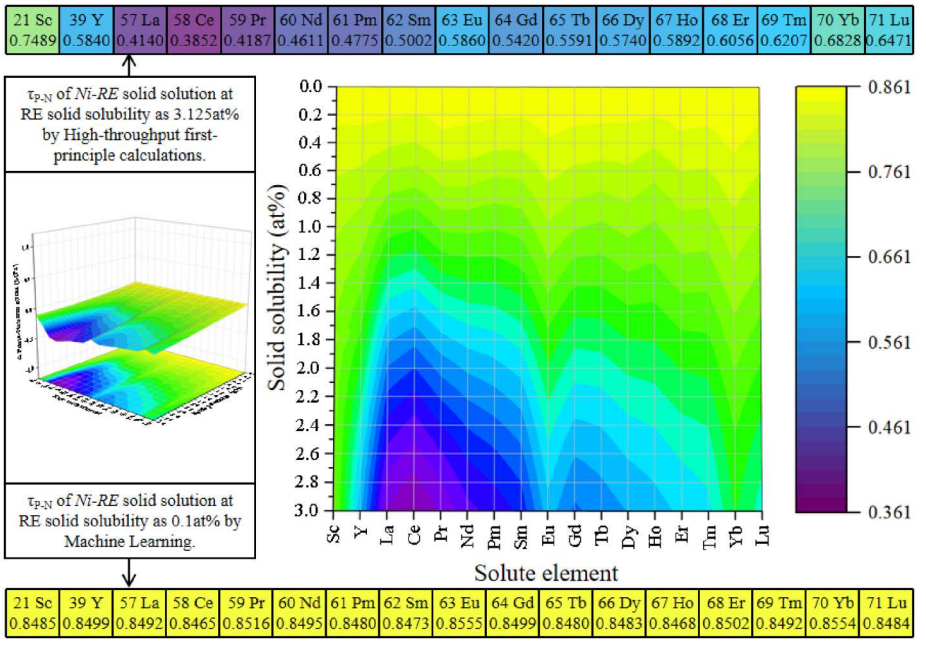

Figure 9. Toughening effect ($\tau_{P\text{-}N}$) of Ni-RE solid solutions.

percentage concertation range *0 ~ 3at%* at intervals of *0.1at%*) were obtained by machine learning (Figure 4). misfit factor ($\boldsymbol{\varepsilon}$) was then deduced based on ML results. (Figures 5 and 6, Table 2). Strengthening ($\boldsymbol{\tau_{CRSS}}$) and toughening ($\boldsymbol{\tau_{P\text{-}N}}$) effects of Ni-RE solid solution were evaluated according to Labusch model (Figure 8) and Peierls-Nabbaro model (Figure 9). As the RE solubility in Ni alloy is quite low, the saturate concentrations of RE in fcc-Ni is considered as experimental saturate concentration *0.1at%* [15]. Then Ni-RE solid solution effect could further assess in element periodic table, Figure 10 (element solubility are all confided by experimental saturate concentration).

Element in faraway or next vicinity to ***Ni*** in the periodic table tend to have a better strengthening ability than other elements. The faraway element series (such as ***Li, Be, Mg, Ca, Al, Si, and both end element in 5nd and 6th period***) are due to big average misfit factor ($\boldsymbol{\varepsilon}$) [15]. The next element series (such as ***Co, Cu***) are due to high solubility ($\boldsymbol{c}$) [48–50]. Furthermore, the elements in close vicinity to Ni in the periodic table (such as ***Cr, Fe, Mn, Zn, Rh, Pd, Ir)*** have best solid solution strengthening effect (increasing more than 10%) for rather higher $\boldsymbol{c}$ and an appreciable $\boldsymbol{\varepsilon}$**.** Furthermore, the faraway vicinity element to Ni (such as ***Li, Be, Mg, Ca, Al, Si, and both end element in 5nd and 6th period***) and ***Ir*** would toughen the alloy well**.** It is due to hybridisation strength and bonding strength decrease more as greater atomic radius difference $\boldsymbol{\Delta r/r_N}$ and make a more obvious change in shear module [29]. Considering the scarcity (such as ***Rh, Pd, Ir***), casting loss (such as ***Mg, Zn***) of the elements, ***Cr, Fe*** (rather higher $\boldsymbol{c}$ and an appreciable $\boldsymbol{\varepsilon}$**,** in close vicinity to Ni) always recommended as the main alloying element

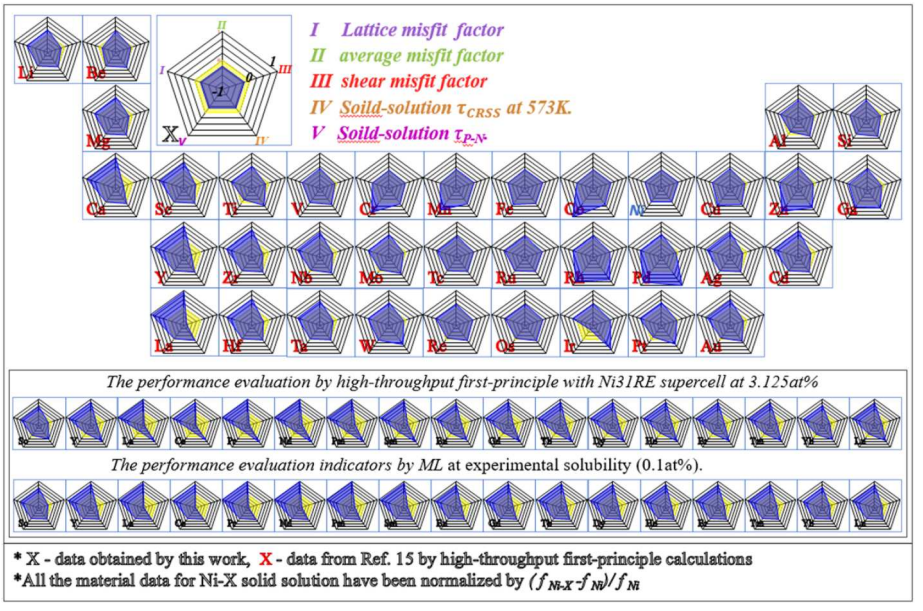

Figure 10. Solid-solution effects of binary Ni-based alloys.

(>10 wt%). Furthermore, ***RE, Al, Si*** (big ε, very low c, and good for toughness, faraway next vicinity to ***Ni***) always proposed as minor alloying element (≤1 wt %). This is quite coherent SSS-deformed Ni-based alloy design (GH3XXX) in ***China superalloy handbook*** [54].

From solid solution alloy design, ***RE*** should be used as minor alloying element. By high-throughput first principal calculation evaluation, it would get material paraments (G, ν, a) at high RE concentration. The paraments (such as G, a) at a certain concertation could be gotten by linear assumption for paraments as the function of the concentration. But the parament as ε_b, ε_s are the partial derivatisations of G, a at the point $C = 0$. So, there would be iterative calculation as mutual independent variables between (G, a) and (ε_b, ε_s). Machine learning (ML) techniques could substantially facilitate the DFT computations [55,56] and active learning [57] also known as the optimal design of experiments, could further decrease the computational cost. The active learning is that a surrogate model is trained from a given data set first, and then the model is applied to pick which data should be obtained in the next operation. After the experiment or computation, the obtained data is added to the original data set and then the surrogate model is updated. The process is repeated iteratively so that the predictive performance of the surrogate model is improved continuously. The results would be quicker and more accurate. It could be seen there are difference in the results between high-throughput first principal calculation and ML in Figure 10.

4. Conclusion

The composition-dependent shear modulus(G), Poisson's ratio (ν) and lattice constants (a) of Ni-RE solid solutions (RE = ***Sc, Y, La ~ Lu***, with the atomic percentage concertation range $0 \sim 3at\%$ at intervals of $0.1at\%$) were obtained by machine learning. misfit factor (ε) was then deduced based on ML results. Strengthening (τ_{CRSS}) and toughening ($\tau_{P\text{-}N}$) effects of Ni-RE solid solution were evaluated according to Labusch model and Peierls-Nabbaro model finally. The main conclusions could be as following:

(1) Shear modulus of Ni-RE solid solution(RE = **Sc, Y, La ~ Lu**) is higher than that of pure Ni ($G_{Ni\text{-}RE} = 70.5543 \sim 92.9821$ GPa (RE concentration rang is $0 \sim 3at\%$), $G_{Ni} = 92.9834$ Gpa) Poisson's ratio, lattice constant, misfit factor of Ni-RE are bigger than those of pure Ni($\nu_{Ni\text{-}RE} = 0.2972 \sim 0.3243$, $\nu_{Ni} = 0.2971$, $a_{Ni\text{-}RE} = 3.5097 \sim 3.5707$ Å, $a_{Ni} = 3.5148$ Å, $\varepsilon_{Ni\text{-}RE} = 2.662 \sim 5.723$, $\varepsilon_{Ni} = 0$). As RE concentration is larger, Shear modulus drops while Poisson's ratio and lattice constant rose ($G\downarrow\nu\uparrow a\uparrow as\ RE\%\uparrow$). As RE atomic radius is larger, Shear modulus drops while Poisson's ratio and lattice constant rose ($G\downarrow\nu\uparrow a\uparrow\varepsilon\uparrow as\ r_{1RE}\uparrow$).

(2) Ni-RE solid solution would leads strengthening and toughening effects. As RE concentration is larger or RE atomic radius is larger, strengthening and toughening are both more obvious ($\tau_{CRSS}\uparrow$ ***and*** $\tau_{P\text{-}N}\downarrow$as ***RE%***$\uparrow$or $r_{1RE}\uparrow$). Furthermore, ***La, Ce, Gd, Tb*** would be the most suitable solid solution ones in *fcc*-Ni among RE elements.

(3) The experimental saturate concentrations of RE in *fcc*-Ni is considered, and Ni-RE solid solution effect could further assess in element periodic table. ***RE*** should be used as minor alloying element in SSS-deformed Ni-based alloy.

Disclosure statement

No potential conflict of interest was reported by the author(s).

Funding

This work was supported by National Key Research and Development Program [grant number 2021YFB3501004], Key Research and Development Program of Jiangxi Province [grant number 20223BBE51021], Jiangxi Province Double Innovation and Scientific Research Training Project Fund [grant number YC2023-S085].

References

[1] S. Roh and D. Kim, *The relationship between public acceptance of nuclear power generation and spent nuclear fuel reuse: Implications for promotion of spent nuclear fuel reuse and public engagement*. Nucl. Eng. Technol. 54 (2022), pp. 2062–2066. doi:10.1016/j.net.2021.12.024.

[2] E. Mansouri, A. Mesbahi, R. Malekzadeh, A.G. Janghjoo, and M. Okutan, *A review on neutron shielding performance of nanocomposite materials*. Int. J. Radiat. Res. 18 (2020), pp. 611–622. doi:10.18869/acadpub.ijrr.18.4.611.

[3] W.Q. Sun, G. Hu, X.H. Yu, J. Shi, H. Xu, R.J. Wu, C. He, Q. Yi, and H.S. Hu, *Study on a high-boron-content stainless steel composite for nuclear radiation*. Materials 14 (2021), pp. 7004. doi:10.3390/ma14227004.

[4] N.H. Tariq, L. Gyansah, J.Q. Wang, X. Qiu, B. Feng, M.T. Siddique, and T.Y. Xiong, *Cold spray additive manufacturing: A viable strategy to fabricate thick B4C/Al composite coatings for neutron shielding applications*. Surf. Coat. Technol. 339 (2018), pp. 224–236. doi:10.1016/j.surfcoat.2018.02.007.

[5] M.E. Mahmoud, A.M. ElKhatib, M.S. Badawi, A.R. Rashad, R.M. Elsharkawy, and A.A. Thabet, *Recycled high-density polyethylene plastics added with lead oxide nanoparticles as sustainable radiation shielding materials*. J. Cleaner Prod. 176 (2018), pp. 276–287. doi:10.1016/j.jclepro.2017.12.100.

[6] Z. Zhu, H. Huang, O. Muránsky, J. Liu, Z. Zhu, and Y. Huang, *On the irradiation tolerance of nano-grained Ni-Mo-Cr alloy: 1 MeV He+ irradiation experiment*. J. Nucl. Mater. 544 (2021), pp. 152694. doi:10.1016/j.jnucmat.2020.152694.

[7] J. Dawidowski, J.R. Granada, J.R. Santisteban, F. Cantargi, and L.A.R. Palomino, *Appendix – Neutron scattering lengths and cross sections*. Exp. Meth. Phys. Sci. 44 (2013), pp. 471–528. doi:10.1016/B978-0-12-398374-9.09989-7.

[8] C. Hu, Q.Y. Huang, and Y.T. Zhai, *Thermal, mechanical investigation and neutron shielding analysis for Gd-MOF/polyimide materials*. RSC Adv. 11 (2021), pp. 40148–40158. doi:10.1039/d1ra07500d.

[9] K. Tsuchiya, A. Tsutsumi, H. Ohtsuka, and M. Umemoto, *Modification of Ni–Mn–Ga ferromagnetic shape memory alloy by addition of rare earth elements*. Mater. Sci. Eng., A 378 (2004), pp. 370–376. doi:10.1016/j.msea.2003.11.076.

[10] J.N. DuPont, C.V. Robino, and T.D. Anderson, *Influence of Gd and B on solidification behavior and weldability of Ni-Cr-Mo alloy*. Sci. Technol. Weld. Join. 13 (2008), pp. 550–565. doi:10.1179/174329308X345083.

[11] R.E. Mizia, T.E. Lister, P.J. Pinhero, T.L. Trowbridge, W.L. Hurt, C.V. Robino, J.J. Stephens, and J.N. Dupont, *Development and testing of an advanced neutron-absorbing gadolinium alloy for spent nuclear fuel storage*. Nucl. Technol. 155 (2006), pp. 133–148. doi:10.13182/NT06-A3752.

[12] X. Fu, Q.C. Zhu, L. Jiang, F. Liu, and Z.J. Li, *Influence of gadolinium on solidification behavior of Ni-Mo-Cr-Gd alloy*. J. Alloys Compd. 950 (2023), pp. 169904. doi:10.1016/j.jallcom.2023.169904.

[13] Z. Zhu, F. Han, Y. Jia, J. Wang, X. Wang, B. Leng, C. Liu, X. Li, and X. Zhou, *Effect of yttrium on intergranular embrittlement behavior of GH3535 alloy induced by tellurium*. Corros. Sci. 216 (2023), pp. 111091. doi:10.1016/j.corsci.2023.111091.

[14] X.L. Li, S.M. He, X.T. Zhou, Y. Zou, Z.J. Li, A.G. Li, and X.H. Yu, *Effects of rare earth yttrium on microstructure and properties of Ni-16Mo-7Cr-4Fe nickel-based superalloy*. Mater. Charact. 95 (2014), pp. 171–179. doi:10.1016/j.matchar.2014.06.016.

[15] M.X. Wang, H. Zhu, G.J. Yang, K. Liu, J.F. Li, and L.T. Kong, *Solid-solution strengthening effects in binary Ni-based alloys evaluated by high-throughput calculations*. Mater. Des. 198 (2021), pp. 109359. doi:10.1016/j.matdes.2020.109359.

[16] S.L. Shang, D.E. Kim, C.L. Zacherl, Y. Wang, Y. Du, and Z.K. Liu, *Effects of alloying elements and temperature on the elastic properties of dilute Ni-base superalloys from first-principles calculations*. J. Appl. Phys. 112 (2012), pp. 053515. doi:10.1063/1.4749406.

[17] S.L. Shang, W.Y. Wang, Y. Wang, Y. Du, X. Zhang J, A.D. Patel, and Z.K. Liu, *Temperature-dependent ideal strength and stacking fault energy of Fcc Ni: A first-principles study of shear deformation*. J. Phys. Condens. Matter. 24 (2012), pp. 155402. doi:10.1088/0953-8984/24/15/155402.

[18] X.X. Yu and C.Y. Wang, *The effect of alloying elements on the dislocation climbing velocity in Ni: A first-principles study*. Acta Mater. 57 (2009), pp. 5914–5920. doi:10.1016/j.actamat.2009.08.019.

[19] J. Friedel and R. Smoluchowski, *Les dislocations*. Phys. Today 10 (1957), pp. 36–39. doi:10.1063/1.3060437.

[20] R.L. Fleischer, *Substitutional solution hardening*. Acta Metall. 11(3) (1963), pp. 203–209. doi:10.1016/0001-6160(63)90213-X.

[21] R. Labusch, *A statistical theory of solid solution hardening*. Phys. Status Solidi 41 (1970), pp. 659–669. doi:10.1002/pssb.19700410221.

[22] D. Ma, M. Friák, J. von Pezold, J. Pezold, D. Raabe, and J. Neugebauer, *Computationally efficient and quantitatively accurate multiscale simulation of solid-solution strengthening by ab initio calculation*. Acta Mater. 85 (2015), pp. 53–66. doi:10.1016/j.actamat.2014.10.044.

[23] J.F. Durodola, *Machine learning for design, phase transformation and mechanical properties of alloys*. Prog. Mater. Sci. 123 (2022), pp. 100797. doi:10.1016/j.pmatsci.2021.100797.

[24] K. Guo, Z. Yang, C.H. Yu, and M.J. Buehler, *Artificial intelligence and machine learning in design of mechanical materials*. Mater. Horiz. 8 (2021), pp. 1153–1172. doi:10.1039/D0MH01451F.

[25] C. Wen, Y. Zhang, C. Wang, D. Xue, Y. Bai, S. Antonov, L. Dai, T. Lookman, and Y. Su, *Machine learning assisted design of high entropy alloys with desired property*. Acta Mater. 170 (2019), pp. 109–117. doi:10.1016/j.actamat.2019.03.010.

[26] C. Zou, J. Li, W.Y. Wang, Y. Zhang, D. Lin, R. Yuan, X. Wang, B. Tang, J. Wang, X. Gao, H. Kou, X. Hui, X. Zeng, M. Qian, H. Song, Z. Liu, and D. Xu, *Integrating data mining and machine learning to discover high-strength ductile titanium alloys*. Acta Mater. 202 (2021), pp. 211–221. doi:10.1016/j.actamat.2020.10.056.

[27] H. Zhang, H. Fu, Y. Shen, and J. Xie, *Rapid design of secondary deformation-aging parameters for ultra-low Co content Cu-Ni-Co-Si-X alloy via Bayesian optimization machine learning*. Int. J. Miner. Metall. Mater. 29 (2022), pp. 1197–1205. doi:10.1007/s12613-022-2479-3.

[28] R. Jaafreh, Y.S. Kang, and K. Hamad, *Brittle and ductile characteristics of intermetallic compounds in magnesium alloys: A large-scale screening guided by machine learning*. J. Magn. Alloys 11 (2023), pp. 392–404. doi:10.1016/j.jma.2022.05.006.

[29] X.G. Wu, Z.Y. Zhong, L. Luo, Y. Liu, Y. Zhou, and F. Zhou, *First-principal exploration for RE solid-solution influence on Ni mechanical properties*. Mater. Today Commun. 37 (2023), pp. 107008. doi:10.1016/j.mtcomm.2023.107008.

[30] F. Birch, *Finite elastic strain of cubic crystals*. Phys. Rev. 71 (1947), pp. 809. doi:10.1103/PhysRev.71.809.

[31] M.Z. Bouayed, A. Yakoubi, R. Ahmed, H. Khachai, R. Khenata, S.H. Naqib, M.M. Obeid, H.R. Jappor, S.J. Edrees, S.B. Omran, and X. Wang, *Insight view of mechanical, electronic and thermodynamic properties of the novel intermetallic REPt4In4 (RE = Eu, Gd, Tb, Dy, Ho) compounds via ab initio calculations*. Bull. Mater. Sci. 43 (2020), pp. 128. doi:10.1007/s12034-020-02095-6.

[32] R. Hill, *The elastic behaviour of a crystalline aggregate*. Proc. Phys. Soc. London Sect. A 65 (1952), pp. 349. doi:10.1088/0370-1298/65/5/307.

[33] G. Kresse and J. Furthmüller, *Efficiency of abinitio total energy calculations for metals and semiconductors using a plane-wave basis set*. Comput. Mater. Sci. 6 (1996), pp. 15–50. doi:10.1016/0927-0256(96)00008-0.

[34] N. Argaman and G. Makov, *Density functional theory: An introduction*. Am. J. Phys. 68 (2000), pp. 69–79. doi:10.1119/1.19375.

[35] P.E. Blöchl, C.J. Först, and J. Schimpl, *Projector augmented wave method: ab initio molecular dynamics with full wave functions*. Bull. Mater. Sci. 26 (2003), pp. 33–41. doi:10.1007/BF02712785.

[36] J.P. Perdew, K. Burke, and M. Ernzerhof, *Generalized gradient approximation made simple*. Phys. Rev. Lett. 77 (1996), pp. 3865. doi:10.1103/PhysRevLett.77.3865.

[37] G. Pari, A. Mookerjee, and A.K. Bhattacharya, *First-principles electronic structure calculations of R3Al5O12 (R being the rare-earth elements Ce-Lu)*. Phys. B 365 (2005), pp. 163–172. doi:10.1016/j.physb.2005.05.011.

[38] X. Wu, Y. Huang, D. Zha, Y. Liu, J. Chen, L. Luo, X. Zhang, and D. Luo, *Theoretical exploration on mechanical properties for Ni-RE intermetallic compounds in nickel alloy*. Mater. Today Commun. 33 (2022), pp. 104521. doi:10.1016/j.mtcomm.2022.104521.

[39] G. Kresse and D. Joubert, *From ultrasoft pseudopotentials to the projector augmented-wave method*. Phys. Rev. B 59 (1999), pp. 1758. doi:10.1103/PhysRevB.59.1758.

[40] H.J. Monkhorst and J.D. Pack, *Special points for Brillouin-zone integrations*. Phys. Rev. B 13 (1976), pp. 5188. doi:10.1103/PhysRevB.13.5188.

[41] B.T. Pham, T.A. Hoang, D.M. Nguyen, and D.T. Bui, *Prediction of shear strength of soft soil using machine learning methods*. Catena 166 (2018), pp. 181–191. doi:10.1016/j.catena.2018.04.004.

[42] D. Chicco, M.J. Warrens, and G. Jurman, *The coefficient of determination R-squared is more informative than SMAPE, MAE, MAPE, MSE and RMSE in regression analysis evaluation*. Peer J. Comp. Sci. 7 (2021), pp. 623. doi:10.7717/peerj-cs.623.

[43] C. Chen, Q. Wang, C. Dong, Y. Zhang, and H. Dong, *Composition rules of Ni-base single crystal superalloys and its influence on creep properties via a cluster formula approach*. Sci. Rep. 10 (2020), pp. 21621. doi:10.1038/s41598-020-78690-8.

[44] A. Moses, D. Chen, P. Wan, and S. Wang, *Prediction of electrochemical corrosion behavior of magnesium alloy using machine learning methods*. Mater. Today Commun. 37 (2023), pp. 107285. doi:10.1016/j.mtcomm.2023.107285.

[45] B.J. Beaudry and K.A. Gschneidner, *Preparation and basic properties of the rare earth metals*. Handb. Phys. Chem. Rare Earths 1 (1978), pp. 173–232. doi:10.1016/S0168-1273(78)01006-5.

[46] I. Toda-Caraballo and P.E.J. Rivera-Daz-del-Castillo, *Modelling solid solution hardening in high entropy alloys*. Acta Mater. 85 (2015), pp. 14–23. doi:10.1016/j.actamat.2014.11.014.

[47] R. Bullough and R.C. Newman, *The kinetics of migration of point defects to dislocations*. Rep. Prog. Phys. 33 (1970), pp. 101. doi:10.1088/0034-4885/33/1/303.

[48] L. Čižek, P. Kratochvíl, and B. Smola, *Solid solution hardening of copper crystals*. J. Mater. Sci. 9 (1974), pp. 1517–1520. doi:10.1007/BF00552938.

[49] C.H. Cáceres and D.M. Rovera, *Solid solution strengthening in concentrated Mg–Al alloys*. J. Light Met. 1(3) (2001), pp. 151–156. doi:10.1016/S1471-5317(01)00008-6.

[50] J. Zander, R. Sandström, and L. Vitos, *Modelling mechanical properties for non-hardenable aluminium alloys*. Comput. Mater. Sci. 41 (2007), pp. 86–95. doi:10.1016/j.commatsci.2007.03.013.

[51] C. Pöhl, J. Schatte, and H. Leitner, *Solid solution hardening of molybdenum–hafnium alloys: Experiments and modeling*. Mater. Sci. Eng. A 559 (2013), pp. 643–650. doi:10.1016/j.msea.2012.09.004.

[52] M.Z. Butt, *Investigation of the activation-parameters of low-temperature slip in cubic metals*. Czech J. Phys. 49 (1999), pp. 1177–1184. doi:10.1023/A:1021126232107.

[53] J.N. Wang, *A new modification of the formulation of Peierls stress*. Acta Mater. 44 (1996), pp. 1541–1546. doi:10.1016/1359-6454(95)00273-1.

[54] High Temperature Materials Division of Chinese Society for Metals, *China superalloy handbook*, Standards Press of China, Beijing, 2012. ISBN 978-7-5066-6237-6.

[55] Z.W. Ulissi, A.J. Medford, T. Bligaard, and J.K. Nørskov, *To address surface reaction network complexity using scaling relations machine learning and DFT calculations*. Nat. Commun. 8 (2017), pp. 14621. doi:10.1038/ncomms14621.

[56] P. Schindler, E.R. Antoniuk, G. Cheon, Y. Zhu, and E.J. Reed, *Discovery of stable surfaces with extreme work functions by high-throughput density functional theory and machine learning*. Adv. Funct. Mater. 34 (2024), pp. 2401764. doi:10.1002/adfm.202401764.

[57] L. Bassman, P. Rajak, R.K. Kalia, A. Nakano, F. Sha, J. Sun, D.J. Singh, M. Aykol, P. Huck, K. Persson, and P. Vashishta, *Active learning for accelerated design of layered materials*. NPJ Comp. Mater. 4 (2018), pp. 74. doi:10.1038/s41524-018-0129-0.

Philosophical Magazine

ISSN: 1478-6435 (Print) 1478-6443 (Online) Journal homepage: www.tandfonline.com/journals/tphm20

Development of a force-matched embedded-atom method (EAM) potential for rhodium-barium alloy system

Sankhasubhra Mukhopadhyay, Soumitra Kumar Dinda & Snehanshu Pal

To cite this article: Sankhasubhra Mukhopadhyay, Soumitra Kumar Dinda & Snehanshu Pal (2026) Development of a force-matched embedded-atom method (EAM) potential for rhodium-barium alloy system, Philosophical Magazine, 106:5, 467-488, DOI: 10.1080/14786435.2025.2570919

To link to this article: https://doi.org/10.1080/14786435.2025.2570919

PHILOSOPHICAL MAGAZINE
2026, VOL. 106, NO. 5, 467–488
https://doi.org/10.1080/14786435.2025.2570919

Taylor & Francis
Taylor & Francis Group

Development of a force-matched embedded-atom method (EAM) potential for rhodium-barium alloy system

Sankhasubhra Mukhopadhyay [a], Soumitra Kumar Dinda[a] and Snehanshu Pal [b]

[a]Metallurgical and Materials Engineering, National Institute of Technology Rourkela, Rourkela, India; [b]Metallurgy and Materials Engineering, Indian Institute of Engineering Science and Technology, Shibpur, India

ABSTRACT

An embedded-atom method (EAM) potential for the Rhodium-Barium (Rh-Ba) alloy system has been parameterised. Computational research on the C15 laves phase compound $BaRh_2$ has been carried out to shape it in critical functional and structural applications. This compound is a type-II superconductor with strong electron–phonon coupling strength. Firstly, the force-matching approach has been used to parameterise the EAM potential, and then the optimisation procedure on converged density-functional theory (DFT) data sets has been carried out to make an appropriate and reliable potential for the Rh-Ba alloy system. A list of fundamental properties, such as density, cohesive energy, elastic properties, thermal expansion coefficient, surface energy, and point defect formation energy, has been examined through molecular dynamics (MD) simulation using the developed EAM potential and validated with DFT-based analysis in order to investigate the accuracy and performance of the potential. A good match between MD and DFT analysis has been found. Thereafter, the EAM potential has been implemented in MD simulation in order to investigate lattice thermal conductivity and diffusional characteristics of the $BaRh_2$ crystal. Diffusion in the crystal lattice is governed by Rh atoms. Phase stability investigation at different temperatures reveals that the hexagonal BaRh phase is most stable. Besides this, the melting points of the above-mentioned alloy system at different compositions are calculated. Slight deviations in the determination of melting points have been reported. X-ray diffraction (XRD) spectra and radial distribution characteristics of the $BaRh_2$ crystal have been additionally presented here to provide further insights into the C15 crystal structure.

ARTICLE HISTORY
Received 25 April 2025
Accepted 29 September 2025

KEYWORDS
Embedded-atom method (EAM); Rh-Ba alloy; density-functional theory (DFT); force-matching approach; cohesive energy; molecular dynamics (MD)

CONTACT Snehanshu Pal snehanshu.pal@gmail.com Metallurgy and Materials Engineering, Indian Institute of Engineering Science and Technology, Shibpur, Howrah 711103, WB, India

Supplemental data for this article can be accessed online at https://doi.org/10.1080/14786435.2025.2570919.

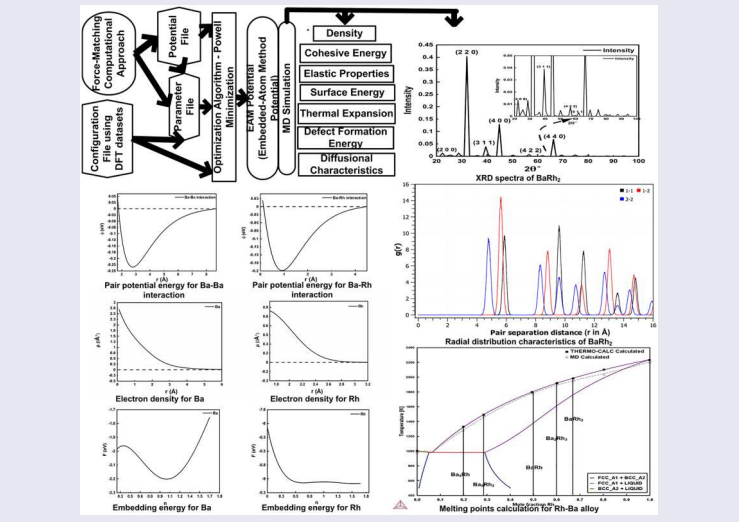

1. Introduction

Rhodium (Rh) is mainly used as a catalyst due to its unique chemical and physical properties [1,2]. Barium (Ba) has important applications in medical imaging technology [3]. Despite the lack of knowledge on the overall significance of the Rh-Ba alloy system, the importance of the $BaRh_2$ laves phase intermetallic compound has been found. Laves phases are of greatest interest in today's research because of their significant applications in the material industry [4,5]. They are used as hydrogen storage materials, superconducting materials, coatings in corrosive atmospheres, magnetic sensors, and a lot more [4,6]. Laves phases crystallise in three formats, C14, C15, and C36, among which C14 and C15 are promising candidates for superconductivity [6]. $BaRh_2$, one of the C15 type laves phase compounds (cubic structure), is defined in the space group Fd-3 m (N° 227) in Hermann-Mauguin notation and has 24 atoms per unit cell [7]. The detailed structural and superconducting properties of $SrRh_2$ and $BaRh_2$ were reported by Gong et al [5] experimentally. They proved the bulk nature of the superconductivity of these compounds, which ensures that the material can be reliably investigated and potentially employed in today's technology. $BaRh_2$ is a type-II superconductor with critical temperature (T_c) of around 5.6 K. This compound is known as an intermediately coupled BCS bulk superconductor due to its strong electron–phonon coupling strength and large specific heat jump [5]. Besides this, it has some remarkable properties like low density, high melting temperature, and high oxidation resistance, which are important for high-temperature structural applications [7,8]. The electronic structure, mechanical properties, and bonding characteristics of BaM_2 (M = Pd, Pt, Rh) compounds were studied by Yakoubi et al [7] using first-principles calculations, and they mentioned that this study is necessary for choosing these compounds in essential engineering applications. Overall, this Rh-Ba alloy system draws significant attention in order to explore the

unexamined phases in addition to the known C15 $BaRh_2$, which helps researchers to choose these compounds for a wide range of critical and advanced engineering applications.

Nowadays, computational algorithms are advancing to solve complex problems using atomistic simulations [9,10]. Atomistic simulation can explain phase transformation phenomena, atomistic diffusion mechanisms, the underlying physics of defects and deformation mechanisms, elastic properties, structural stability, high-temperature modelling, and much more. From this viewpoint, molecular dynamics simulation plays an important role. The interatomic potential is an essential part of MD simulation [10–13]. Atomistic simulation is essential here to study these types of laves phase compounds from scratch, as experimental data are very rare [14]. The performance and reliability of the simulation results are directly proportional to the accuracy of fitting of the developed potential, so selecting an appropriate potential is important for MD simulation [10,11,15]. In comparison with the simple pairwise potential, the embedded-atom method (EAM) [16–19] potential, which is widely used for metals and alloys, has some advantages, such as better representation of bond saturation and surface bonding, elimination of unphysical elastic constraint $C_{12} = C_{44}$ [9,20–22]. A couple of previous studies related to the implementation of EAM potential in laves phase compounds are included below. Vibrational properties of $MgZn_2$ were explained using an EAM potential by Brommer et al [23]. Thermo-mechanical aspects of the $NbCr_2$ were reported by Heaton et al [24].

EAM potential is unavailable for the Rh-Ba alloy system, and experimental data on this system are scarce to proceed with research on this alloy system. The fundamental computational research on the C15 laves phase compound $BaRh_2$, as well as on the Rh-Ba alloy system, with the help of an appropriate EAM potential, has been carried out, which will help researchers to choose this alloy system in critical engineering applications. In this paper, an EAM potential for the Rh-Ba system has been parameterised in order to investigate several aspects. Density, elastic properties, cohesive energy, thermal expansion coefficient, surface energy, and point defect formation energy have been determined using MD simulation with the help of the parameterised EAM potential. These properties have been verified with DFT analysis in order to examine the precision of the potential. A few properties among the above-mentioned ones have also been examined using a universal machine learning (ML) based interatomic potential in order to compare performance with the developed EAM potential. Lattice thermal conductivity of the $BaRh_2$ crystal has been reported in order to look into its thermoelectric property. The diffusional characteristics of the same have been studied, and the melting points calculation of the Rh-Ba alloy system has been carried out using MD simulation. Diffusion coefficients in the C15 $BaRh_2$ might be useful in the rational design of Rh-Ba alloys. Melting points at different compositions are important in order to locate the liquidus line on the phase diagram of the above-mentioned alloy system. Calculations of the Gibbs free energy of mixing (ΔG_{mix}) at various temperatures show that the hexagonal BaRh (Ba50Rh50) phase is the most stable among others. Additionally, X-ray diffraction (XRD) spectra and radial distribution characteristics of the $BaRh_2$ crystal have been reported in our paper to report some other crystal insights. QUANTUM ESPRESSO [25,26] has been used to

perform density functional theory (DFT) calculations. LAMMPS [27] has been used for MD simulation. THERMO-CALC [28] has been used to create the approximate phase diagram of the Rh-Ba alloy system.

2. Computational methodology for developing the EAM potential

In the EAM potential, the total potential energy is given by [9,29,30],

$$E = \sum_{i<j} \phi_{s_i s_j}(r_{ij}) + \sum_i F_{s_i}(n_i) \tag{1}$$

EAM formalism is based on DFT ideas [6]. The pair interaction energy is represented by the first part of Equation (1), which depends on the interatomic distance $r_{ij} = |i - j|$ between i^{th} and j^{th} atoms. Notations s_i & s_j represent different atom species. The other part of Equation (1) is termed as embedding energy, which depends on the host electron density n_i at the i^{th} atom's position due to all other atoms. Host electron density, which depends on the electron density function $\rho(r)$, is given by Equation (2),

$$n_i = \sum_{j \neq i} \rho_{s_j}(r_{ij}) \tag{2}$$

The DFT calculations have been performed using the plane-wave self-consistent field (PWscf) package in QUANTUM ESPRESSO [25,26]. The Perdew–Burke–Ernzerhof (PBE) functional [31] and the projector augmented-wave (PAW) pseudopotentials [32] generated by CORSO [33] have been used for this perspective. Convergence criteria have been achieved using a $4 \times 4 \times 4$ k-point mesh, kinetic energy cut-offs of about 476.20 and 1904.80 eV for plane-wave function and charge density, respectively, and ordinary Gaussian spreading of about 0.14 eV in the self-consistent field calculations. Nine unperturbed reference structures have been used, which are $BaRh_2$ (Fd-3 m), Ba_4Rh (C2/m), Ba_4Rh ($Cmc2_1$), BaRh ($P6_3/mmc$), Ba_5Rh_2 (C2/c), Ba_2Rh_3 (P-3m1), Ba_7Rh_3 ($P6_3mc$), Ba (Im-3 m), and finally Rh (Fm-3 m). Additionally, two defect structures have been incorporated; one is $BaRh_2$ (Fd-3 m) with Ba vacancy, and another is $BaRh_2$ (Fd-3 m) with Rh vacancy. The proportions of pure Ba and pure Rh in the compounds are given by $BaRh_2 \equiv Ba33.3Rh66.7$, $Ba_4Rh \equiv Ba80Rh20$, $BaRh \equiv Ba50Rh50$, $Ba_5Rh_2 \equiv Ba71.4Rh28.6$, $Ba_2Rh_3 \equiv Ba40Rh60$, $Ba_7Rh_3 \equiv Ba70Rh30$. The initial structures (space groups are given in brackets) have been selected from the OPEN QUANTUM MATERIALS DATABASE (OQMD) and MATERIALS PROJECT [34–36]. Thereafter, rigorous DFT calculations have been performed for structure relaxation purposes. During the phase stability calculation, two new structures (only for test purposes) – Ba_6Rh (Cc) $\equiv Ba85.7Rh14.3$, and $BaRh_3$ ($P6_3/mmc$) $\equiv Ba25Rh75$ are considered.

POTFIT [9,37–41] package, which is based on the force-matching method by ERCOLESSI and ADAMS [42], has been used to develop an EAM potential for the Rh-Ba alloy system using DFT datasets. The atomic coordinates of the relaxed structures and force components on atoms, as obtained through DFT calculations, in addition to unit cell dimensions, and cohesive energies [7,35,36] have been used to make the configuration file of the force-matching package.

The pair interaction energy ($\phi(r)$), electron density ($\rho(r)$), and embedding energy ($F(n)$) terms are given by Equations (3)–(5) [29,37,43], respectively.

$$\phi(r) = [E_1 M(r, r_0^{(1)}, \alpha_1) + E_2 M(r, r_0^{(2)}, \alpha_2) + \delta] \times \psi(r - r_{cutoff}^{\phi}/h_1) \tag{3}$$

$$\rho(r) = [a exp(-\beta_1 (r - r_0^{(3)})^2) + exp(-\beta_2 (r - r_0^{(4)}))] \times \psi(r - r_{cutoff}^{\rho}/h_2) \tag{4}$$

$$F(n) = F_0 + \frac{1}{2} F_2 (n-1)^2 + \sum_{s=1}^{3} q_s (n-1)^{s+2} \tag{5}$$

Here, $M(r, r_0, \alpha) = \exp(-2\alpha(r - r_0)) - 2\exp(-\alpha(r - r_0))$ is the Morse function and $\psi(x)$ is termed as the smooth cut-off function such that $\psi(x) = 0$ if $x \geq 0$ and $\psi(x) = x^4/(1 + x^4)$ if $x < 0$. The smooth cut-off function has been used to satisfy $\phi(r \geq r_{cutoff}^{\phi}) = 0$ & $\rho(r \geq r_{cutoff}^{\rho}) = 0$ [29,43,44]. The embedding energy data points are based on average host electron density. The ordering of the potential is represented as Ba-Ba, Ba-Rh, Rh-Rh, Ba, Rh, Ba, Rh. Cut-off radii (r_{cutoff}^{ϕ}) for ϕ_{Ba-Ba}, ϕ_{Ba-Rh}, and ϕ_{Rh-Rh} are around 8.38 Å, 4.44 Å, and 4.39 Å, respectively. r_{cutoff}^{ρ} for ρ_{Ba} and ρ_{Rh} are around 5.32 Å and 2.99 Å, respectively. The optimisation procedure is defined by the minimisation of the sum of squares of deviation between the EAM and DFT datasets [9]. The minimising function is given by $Z = Z_F + Z_C$.

Here,

$$Z_F = \sum_{q=1}^{N_A} u_q (F_q^{EAM} - F_q^{DFT})^2 \tag{6}$$

$$Z_C = \sum_{q=1}^{N_c} w_q (A_q^{EAM} - A_q^{DFT})^2 \tag{7}$$

The relative fluctuation of force and energy between EAM and DFT values is given by Equations (6) and (7), respectively. u_q and w_q are weights associated with the force part and the energy part, respectively. w_q is chosen as 80. On the other hand, the default value of $u_q = 1$, is used. Figure 1 represents the comparison between EAM and DFT energies and forces. Each point in the plots represents a structure mentioned in the caption of Figure 1.

The number of atoms in the configuration database and the number of energies per atom are represented by N_A and N_c, respectively [9,37,38]. Among different optimisation algorithms, the Powell minimisation technique has been used [37,45]. Root mean square errors, after the optimisation, for forces and energies are 252.62 meV/Å and 249.59 meV/atom, respectively. Distorted structures are not considered, and the data set is limited due to computational inefficiency. In this perspective, a literature study is mentioned below. Thermo-mechanical behaviour of the Nb-Cr system was described by Heaton et al [24] using a developed EAM potential where no Nb-Cr or other mixed structures were used for the training process. However, Figure 1 depicts an approximate good fit between EAM and DFT predictions. Structures 2 and 7 deviate more from the fitted lines in both plots. Values of optimised parameters for

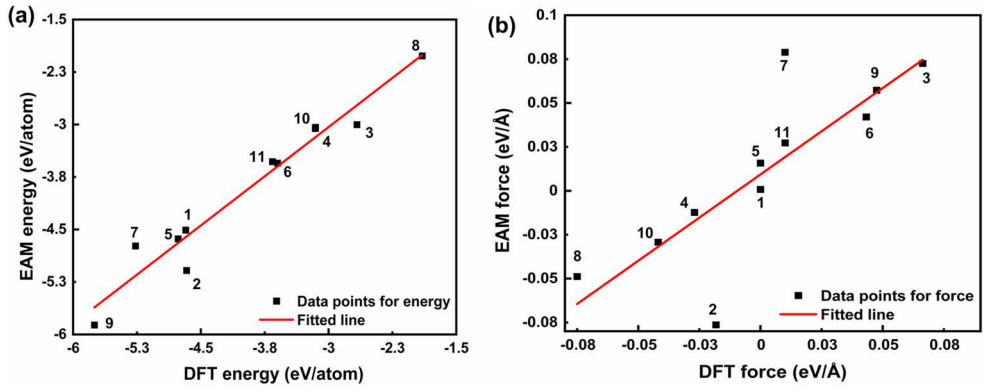

Figure 1. EAM versus DFT prediction for (a) energy, and (b) force. Structures are 1 – $BaRh_2$ (Fd-3 m), 2 – Ba_7Rh_3 ($P6_3mc$), 3 – Ba_4Rh ($Cmc2_1$), 4 – Ba_4Rh (C2/m), 5 – BaRh ($P6_3/mmc$), 6 – Ba_5Rh_2 (C2/c), 7 – Ba_2Rh_3 (P-3m1), 8 – Ba (Im-3 m), 9 – Rh (Fm-3 m), 10 – $BaRh_2$ (Fd-3 m) with Rh vacancy, 11 – $BaRh_2$ (Fd-3 m) with Ba vacancy.

Table 1. Optimised parameters of ϕ(r) for Ba-Ba, Ba-Rh, and Rh-Rh interactions.

Parameter (Unit)	Ba-Ba interaction	Ba-Rh interaction	Rh-Rh interaction
E_1 (eV)	0.242	1.623	−2.051
α_1 (Å^{-1})	0.680	1.262	2.616
$r_0^{(1)}$ (Å)	2.782	−0.008	−0.429
E_2 (eV)	2.239	−1.733	0.930
α_2 (Å^{-1})	−0.003	1.538	1.607
$r_0^{(2)}$ (Å)	1.083	−0.104	1.349
δ (Å)	2.247	0.008	0.008
h_1 (Å)	1.081	1.489	1.350

Table 2. Optimised parameters of ρ(r) for Ba, and Rh.

Parameter (Unit)	Ba	Rh
a	0.296	0.798
β_1 (Å^{-2})	0.662	
$r_0^{(3)}$ (Å)	1.200	1.633
β_2 (Å^{-1})	0.889	2.405
$r_0^{(4)}$ (Å)	1.153	0.517
h_2. (Å)	0.564	0.823

Table 3. Optimised parameters of F(n) for Ba, and Rh.

Parameter (Unit)	Ba	Rh
F_0 (eV)	−2.202	−9.054
F_2 (eV)	2.380	−0.504
q_1 (eV)	0.284	−0.001
q_2 (eV)	−0.888	0.761
q_3 (eV)	0.217	−0.481

$\phi(r)$, $\rho(r)$, and $F(n)$ are listed in Tables 1–3, respectively. Graphical representations of these fitting functions are depicted in Figures 2–4, respectively, as represented in different literatures [46,47].

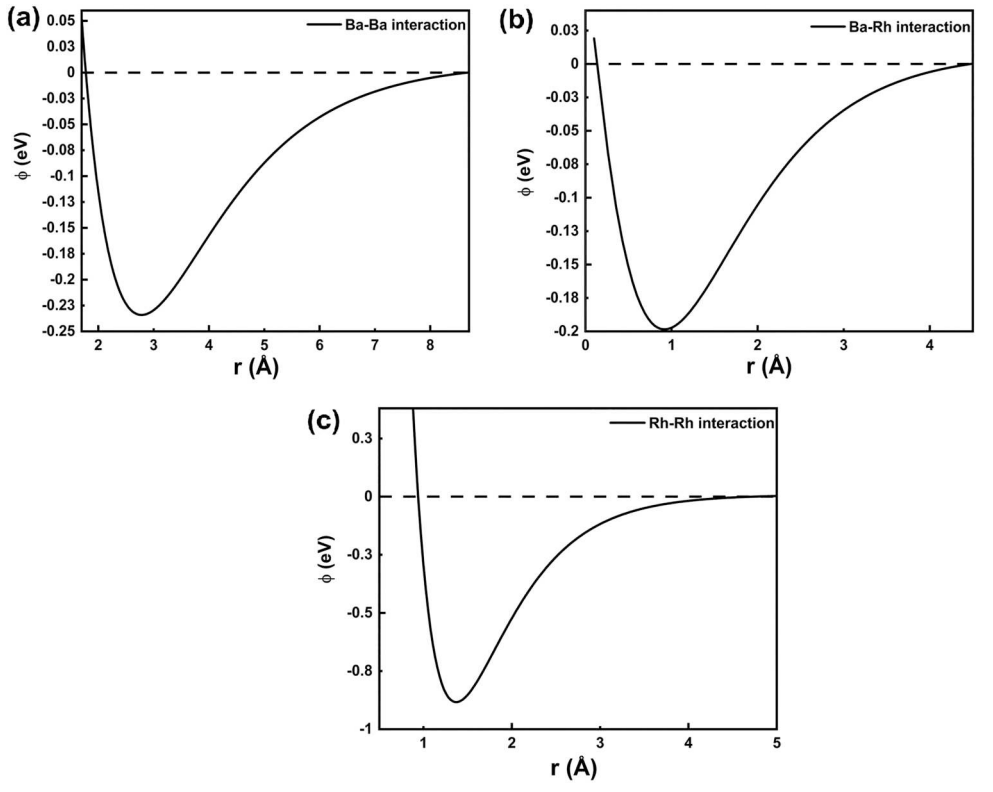

Figure 2. Pair potential energy (ϕ) as a function of interatomic distance (r) for (a) Ba-Ba, (b) Ba-Rh, and **(c)** Rh-Rh interactions.

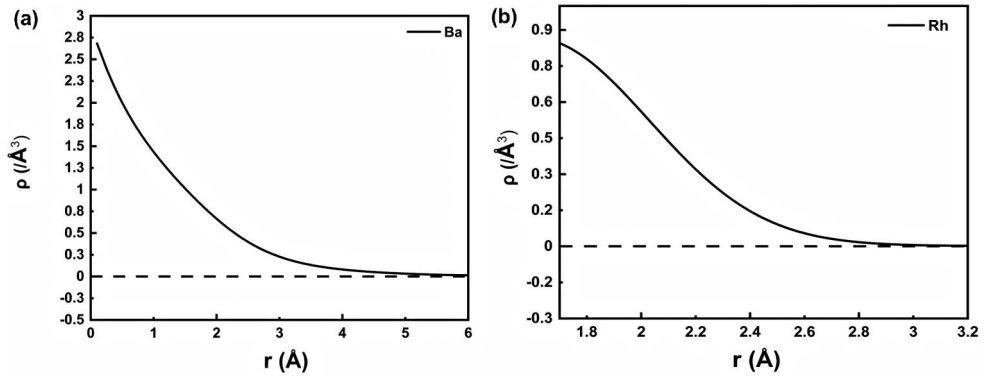

Figure 3. Electron density (ρ) as a function of interatomic distance (r) for (a) Ba, and (b) Rh.

3. Results & discussions

This section comprises three parts. In the first part, the developed EAM potential is utilised in MD simulation to calculate density, cohesive energy, thermal expansion coefficient, elastic properties, surface energy, and point defect formation energy. These properties are then validated with DFT results to verify the accuracy of the potential. In addition to that, a few of the

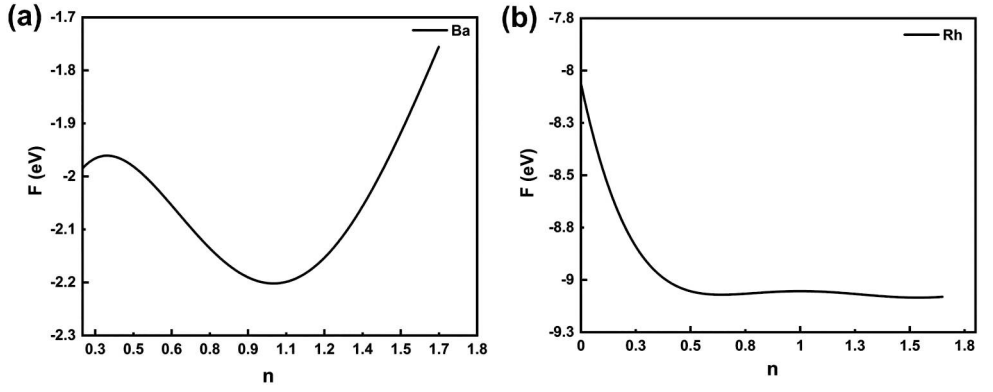

Figure 4. Embedding energy (*F*) as a function of host electron density (*n*) for (a) Ba, and (b) Rh.

aforementioned properties have also been calculated with a universal ML-based interatomic potential in order to compare performance with the parameterised EAM potential. This is included in the second part. Thereafter, lattice thermal conductivity, X-ray diffraction spectra, radial distribution characteristics, and diffusional phenomena of $BaRh_2$ crystal have been studied through MD simulation using the parameterised EAM potential. Additionally, the melting points calculation at different compositions, and the phase stability prediction at different temperatures of the Rh-Ba alloy system are described. These are reported in the third part. All MD simulations have been performed with a single crystal.

3.1. EAM potential verification

3.1.1. Density

$BaRh_2$ crystal structure has been made using the ATOMSK package [48]. Applying the NVT ensemble, the density of the $BaRh_2$ crystal as obtained from MD simulation is around 9.42 g/cc. Density as retrieved from the MATERIALS PROJECT [34] for $BaRh_2$ (mp-568430) from database version v2025.06.09 [49] is 9.19 g/cc, indicating that there is a good agreement between these results. The density of Ba and Rh has also been determined. Densities of Ba and Rh as obtained from MD simulations are around 3.65 and 12.16 g/cc, respectively. These results are also close to their actual densities, which are 3.62 and 12.41 g/cc [50] for Ba and Rh, respectively.

3.1.2. Cohesive energy

Cohesive energy of $BaRh_2$, as taken from DFT analysis [7], is 6.101 eV/atom. Cohesive energy, as obtained through MD simulation by calculating potential energy/atom, is around – 5.907 eV/atom. The negative sign indicates that energy is released when atoms come close together and make bonds. This implies the fact that $BaRh_2$ is stable. The magnitude of cohesive energy as obtained through MD simulation is in good agreement with DFT analysis.

3.1.3. Elastic properties

Various elastic properties of the $BaRh_2$ crystal have been determined by MD simulation using the simulation box deformation technique at $T = 0$K. The essential minimisation

parameter *dmax* has been selected within the range between 1.5×10^{-5} Å to 3×10^{-5} Å for performing this simulation. Firstly, the box has been deformed along a fixed direction for the calculation of C_{11} and C_{12}.. Then the box has been tilted in the xy-direction to include the shear effect in order to calculate C_{44}. MD results are not very far away from DFT results [51] except for C_{44}, which are lted in Table 4. Large deviation in the value of C_{44}, which may be due to the absence of angular forces in the potential [52] or limitations in the stress fitting weight [9], will be investigated further. Discrepancies for C_{44} are also observed in some other literatures [53,54]. C_{11}, C_{12}, and C_{44} characterises a cubic structure. MD results agree with the criteria, such as $C_{11} - C_{12} > 0$, $C_{11} > 0$, $C_{44} > 0$, and $(C_{11} + 2C_{12}) > 0$ [7], indicating that $BaRh_2$ is elastically stable. Equations for the bulk modulus and Poisson's ratio are $B = \frac{1}{3}(C_{11} + 2C_{12})$, $\nu = \frac{C_{12}}{C_{11} + C_{12}}$ [7,55]. Anisotropy parameter (A), defined by $A = 2C_{44}/(C_{11} - C_{12})$ [7], is around 0.87 as obtained from MD data. This fact clearly indicates that this crystal is anisotropic as $A \neq 1$.

3.1.4. Thermal expansion coefficient (α)

The volumetric thermal expansion coefficient of $BaRh_2$ has been calculated near room temperature using both DFT and MD-based simulations. DFT simulation has been carried out using the GIBBS2 [56] package. Initially, the THERMO_PW [57] package has been used to generate energy vs volume data. Then, this data has been implemented into the GIBBS2 script file to calculate different thermodynamic quantities. The value of α near room temperature, as obtained using DFT calculation, is around 4.6×10^{-5} /K. Initially, the NVT ensemble has been used in MD simulation for equilibration purposes. Then, a change in volume with respect to temperature (near room temperature range) has been observed using the NPT ensemble. Value of α, as obtained using $\alpha = \frac{1}{V}\left(\frac{\partial V}{\partial T}\right)_p$ is around 4.2×10^{-5} /K. The DFT result is not so far away from the MD result. This order of magnitude is also supported by a similar C15 compound, Cr_2Zr [58]. This is crucial in several engineering applications where dimensional stability is concerned.

3.1.5. Surface energy (γ)

The surface energy corresponding to the Miller index (1 1 1) for both Barium and Rhodium single crystals has been calculated using MD simulation via the 'surface_energy_static' code [59]. Starting with a unit cell, a transformed system has been created by rotating it such that the box vectors correspond to crystallographic

Table 4. Comparison of elastic stiffness coefficients (C_{ij}), bulk modulus (B), and Poisson's ratio (ν) of the $BaRh_2$ crystal between MD and DFT [51] analysis.

Property (Unit)	MD	DFT
C_{11} (GPa)	128.17	132
C_{12} (GPa)	76.55	76
C_{44} (GPa)	22.69	32
B (GPa)	93.76	95
ν	0.37	0.36

directions and the atoms have been arranged to maintain a perfect bulk structure with periodic boundaries. Then, a supercell has been created by duplicating the modified system. Two MD simulations (one with p p p, another with p p m boundary) have been carried out that apply energy/force minimisation on the system and calculate total energy (E_{total}) after relaxation. γ_{111} as obtained using MD simulation are 0.43, and 1.99 J/m^2 for Ba, and Rh respectively. DFT data for surface energy have been taken from the Crystalium [60] web application. γ_{111} as retrieved from DFT-based web application are 0.39, and 1.98 J/m^2 for Ba, and Rh respectively. The discrepancy for Barium may have been due to the differences in supercell size.

3.1.6. Point defect formation energy

Vacancy and octahedral site self-interstitial formation energies of Barium and Rhodium single crystals have been reported using both MD and DFT-based calculations/ab initio study-oriented literatures. Vacancy formation energy has been calculated using $E_v = E_f - [(N_0 - 1)/N_0] \times E_i$, where E_f is the final energy of the relaxed system after creation of one vacancy, E_i is the initial energy before the vacancy, and N_0 is the total number of atoms in the cell before vacancy [61]. Similarly, the interstitial formation energy has been calculated using $E_i = E_f - [(N + 1)/N] \times E_0$, where E_f is the final energy of the relaxed system after the injection of one atom into the interstitial position, E_0 is the initial energy, and N is the initial number of atoms [62]. Supercells in DFT calculations have been made using the PHONOPY [63] package. MD and DFT comparisons are shown in Table 5. Due to variations in supercell size and volume relaxing techniques, discrepancies have been found, as supported by literature [64]. A couple of studies reported some significant discrepancies in the octahedral site self-interstitial formation energy [65,66].

3.2. Comparison study with a universal ML potential

In order to compare the accuracy and speed of the developed EAM potential with a universal ML potential – PET-MAD, a generally applicable ML-based interatomic potential [68] has been used. PET refers to the point edge transformer graph neural network, and MAD refers to the massive atomistic diversity dataset. The MAD dataset contains 95595 structures of 85 elements (atomic numbers 1–86, except Astatine).

3.2.1. Accuracy

Table 6 reports the comparison study in terms of accuracy for the cohesive energy, point defect formation energy, and thermal expansion coefficient between the EAM potential and ML-based potential implemented results with DFT-based calculations/ab initio study-oriented literatures.

Table 5. MD and DFT comparison for point defect formation energy.

Point defect formation energy	Crystal	MD (eV)	DFT / Literature (eV)
Vacancy formation energy	Ba	1.30	1.19
	Rh	1.72	1.87 [67]
Octahedral site self-interstitial formation energy	Ba	4.04	6.47
	Rh	6.82	6.73 [67]

Table 6. Accuracy comparison between the EAM potential and ML-based potential with DFT.

Properties (Unit)		Crystal	EAM potential	ML potential	DFT/ Literature
Cohesive energy magnitude (eV/atom)		$BaRh_2$	5.907	5.529	6.101
Point defect formation energy	Vacancy formation energy (eV)	Ba	1.30	0.31	1.19
		Rh	1.72	2.08	1.87 [67]
	Octahedral site self-interstitial formation energy (eV)	Ba	4.04	3.39	6.47
		Rh	6.82	9.73	6.73 [67]
Thermal expansion coefficient (/K)		$BaRh_2$	4.2×10^{-5}	5.3×10^{-5}	4.6×10^{-5}

3.2.2. Speed

In order to compare speed, a single-point calculation with the serial version of LAMMPS has been performed with both the potential. For instance, with 192 atoms EAM potential takes around 1 s of CPU time, whereas the ML potential takes around 80 s of CPU time.

The above comparison states that the parameterised EAM potential is much more accurate than the universal ML potential in describing the fundamental properties of the reported system with respect to DFT results. Additionally, the EAM potential takes much less time than the ML potential. These facts clearly justify the need for the Rh-Ba EAM potential over the universal ML potential.

3.3. Implementation of EAM potential in MD simulation

3.3.1. Lattice thermal conductivity (κ_{ph})

Lattice thermal conductivity of $BaRh_2$ has been calculated using the Green-Kubo formalism [69,70] via MD simulation. This mechanism calculates heat flux from the per-atom fluctuation of potential energy, kinetic energy, and stress tensor in steady-state conditions. The NVT ensemble, timestep of 1 fs, and temperature $T = 300$K have been opted in order to perform this simulation. Output has been observed after every 200 time steps. Value of κ_{ph}, as obtained using MD simulation, is around 3.413 W/m/K. A low value of κ_{ph} for the crystal helps researchers to find its application in the thermoelectric materials domain. DFT calculation for κ_{ph} can be carried out in the future using the PHONO3PY [63] package.

3.3.2. X-ray diffraction (XRD) spectra

The virtual X-ray diffraction spectra of $BaRh_2$ crystal, as shown in Figure 5(a), is based on MD simulation, whereas the XRD spectra as regained from the MATERIALS PROJECT [34] for $BaRh_2$ (mp-568430) from database version v2025.06.09 is depicted in Figure 5(b) [49]. CuKα ($\lambda \sim 1.542$ Å) is used as a radiation source in both cases. MD simulation is carried out using the compute xrd command. No experimental observation has been found regarding the XRD spectra of the $BaRh_2$ crystal. In MD simulation, diffraction peaks are found corresponding to (h k l) values (2 0 0), (2 2 0), (3 1 1), (4 0 0), (4 2 2), and (4 4 0), which indicates that these planes are present in the $BaRh_2$ crystal. In addition to that, the (5 1 1) peak has also been reported while zooming into the intensity scale, as shown with an arrow. Some other intense peaks, which are observed in Figure 5(b) within the 100° coordinate value, can also be identified from Figure 5(a) in a similar fashion. Overall, the distortions in atomic positions may result from the approximations being made to optimise the structure and from the thermal noise in the MD simulation.

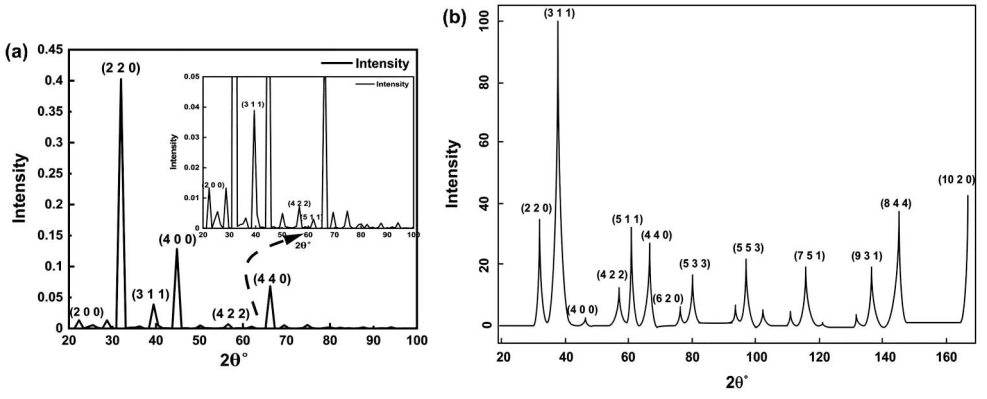

Figure 5. (a) XRD pattern of $BaRh_2$ crystal as obtained from MD simulation, and (b) XRD spectra as retrieved from the MATERIALS PROJECT [34] for $BaRh_2$ (mp-568430) from database version v2025.06.09 [49].

Additionally, intensity differences have also been observed between MD and DFT-based outcomes.

3.3.3. Radial distribution characteristics

Equilibrating the structure of the $BaRh_2$ crystal using the NPT ensemble at 300 K for around 50,000 time steps, OVITO [71] is used to visualise the radial distribution plot. 5000 histogram bins have been used for this calculation. The probability of finding a particle at a position r when there is another particle at $r = 0$ is given by the function $g(r)$, termed as radial distribution function. Variation of $g(r)$ with r is depicted in Figure 6. Ba-Ba, Ba-Rh, and Rh-Rh interactions are represented by 1-1, 1-2, and 2-2, respectively. Stronger Ba-Rh bonding than Ba-Ba, and Rh-Rh bonding within the first pair separation distance, is explained by the fact that the Ba-Rh peak is higher than the other two within that distance. This also explains that the population of Ba-Rh interaction is higher within that distance. Thereafter, the probability of finding a Ba atom near another Ba atom is sometimes greater than finding a Ba atom near a Rh atom, which may result from a fluctuation in local atomic arrangement. However, Ba-Rh interaction is overall higher because of the diamond-shaped arrangement [72].

3.3.4. Determination of diffusion coefficients (D)

Diffusion coefficients in $BaRh_2$ have been calculated using MD simulation via vacancy diffusion mechanism, as in these types of compounds, diffusion is mainly mediated by vacancies [73,74]. Mean-squared displacements (MSD) of atoms have been calculated to determine diffusion coefficients (D). D can be calculated as, $D = \lim_{t\to\infty} \frac{1}{6t}\Delta r(t)^2$ for a 3-dimensional system [75]. D can usually be obtained from the $\frac{1}{6}\times$slope of the linear fit of the MSD versus time curve [74,75]. Here, two different models have been made to calculate D – (i) sample with monovacancy in the Ba position and (ii) sample with monovacancy in the Rh position. Similar kinds of models for C15 Cr_2Ta have been found in the literature [74]. The variation of the diffusion coefficient with temperature

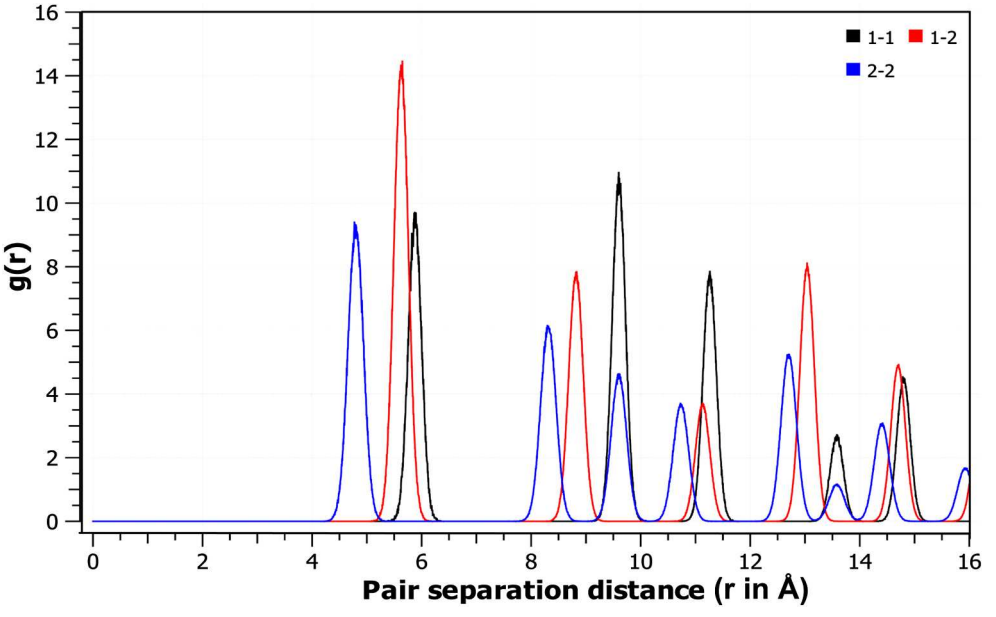

Figure 6. Plot of radial distribution function $g(r)$ with pair separation distance (r) for $BaRh_2$ crystal. Ba-Ba, Ba-Rh, and Rh-Rh interactions are denoted by 1-1, 1-2, and 2-2, respectively.

is shown in Figure 7. Diffusion coefficients as a function of temperature for both models are reported in Table 7. Enhancement in the movement of atoms due to an increment in temperature is satisfied by the increment in D with an increase in T, as reported in our paper. Thereafter, lnD is plotted against $1000/T$ to understand the effect of different vacancy models. These are depicted in Figure 8. It is seen clearly that the values of lnD_{Rh} and lnD_{Ba+Rh} are close, and the values of lnD_{Ba} are smaller in both cases. This signifies the fact that Ba atoms vary their initial mean positions less than Rh atoms with time. Therefore, diffusion is governed by Rh atoms in both the Ba monovacancy and the Rh monovacancy models.

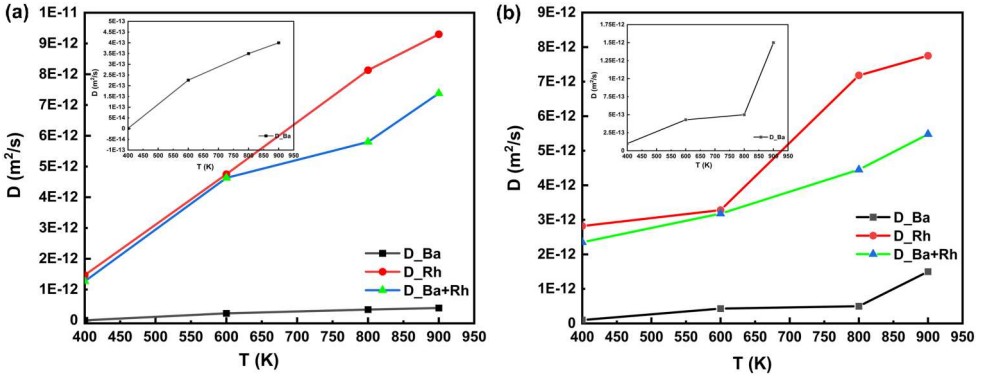

Figure 7. Plot of diffusion coefficients (D) as a function of temperatures (T) for (a) Ba monovacancy model, and (b) Rh monovacancy model. Zoomed figures are attached to visualise the variation of D for Ba clearly.

Table 7. Data of diffusion coefficients (D) with temperatures (T).

Model	T (K)	D_Ba (m^2/s)	D_Rh (m^2/s)	D_Ba + Rh (m^2/s)
Ba monovacancy	400	7.39×10^{-16}	1.47×10^{-12}	1.27×10^{-12}
	600	2.26×10^{-13}	4.75×10^{-12}	4.63×10^{-12}
	800	3.50×10^{-13}	8.13×10^{-12}	5.80×10^{-12}
	900	4.00×10^{-13}	9.30×10^{-12}	7.38×10^{-12}
Rh monovacancy	400	1.00×10^{-13}	2.82×10^{-12}	2.35×10^{-12}
	600	4.30×10^{-13}	3.28×10^{-12}	3.18×10^{-12}
	800	5.00×10^{-13}	7.18×10^{-12}	4.45×10^{-12}
	900	1.50×10^{-12}	7.75×10^{-12}	5.48×10^{-12}

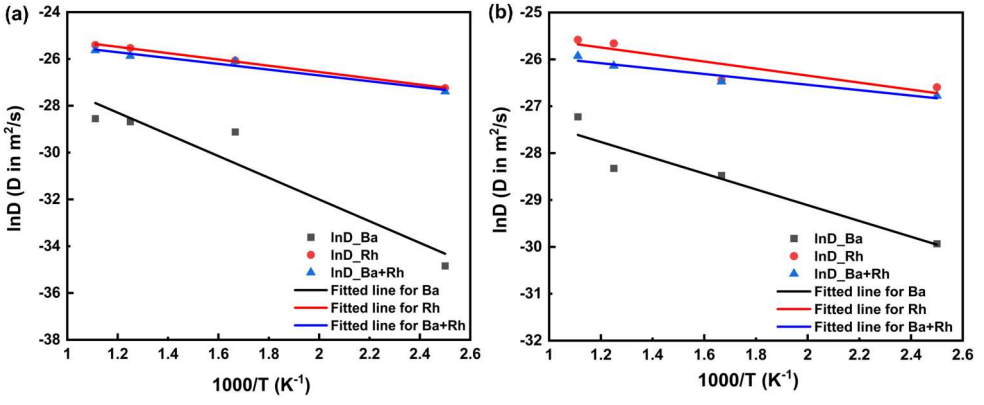

Figure 8. Plot of *lnD* versus 1000/*T* for (a) Ba monovacancy model, and (b) Rh monovacancy model.

3.3.5. Phase stability prediction at different temperatures

Free energies are essential because they shed light on the relative stability of different phases [76]. Understanding phase stability at different temperatures is crucial before applying the concerned alloy system in critical engineering applications. Here, the calculation of the Gibbs free energy of mixing (ΔG_{mix}) for the Rh-Ba alloy has been carried out using MD simulation for a temperature range of 300 K to 900 K. ΔG_{mix} is calculated as $\Delta G_{mix} = \Delta E_{form} - T\Delta S$ [77]. The formation energy of the alloy is represented as $\Delta E_{form} = E(Ba_{1-x}Rh_x) - \{(1-x)E(Ba)\} - \{xE(Rh)\}$. The configurational entropy of mixing is represented as $\Delta S = -R[\{xln(x)\} + \{(1-x)ln(1-x)\}]$ [77]. Here, E represents the total energy per atom of the composition specified in the bracket, x represents the mole fraction of *Rh* in $Ba_{1-x}Rh_x$, and R is the universal gas constant, which is nearly 8.62×10^{-5} eV/atom/K. The total energy of different compositions has been calculated using the NPT ensemble at standard atmospheric pressure and different temperatures ranging from 300 K to 900 K with a timestep of 1 fs. Figure 9 depicts the variation of ΔG_{mix} with x. It is clear from the figure that although all the mentioned phases are thermodynamically stable, the hexagonal BaRh (Ba50Rh50) phase is the most stable among the others. As of now, no experimental evidence regarding this phase has been found. Study on the superconducting properties of C15 $BaRh_2$ (Ba33.3Rh66.7) is found in literature [5], which is the only experimental evidence among all the phases in the concerned alloy system.

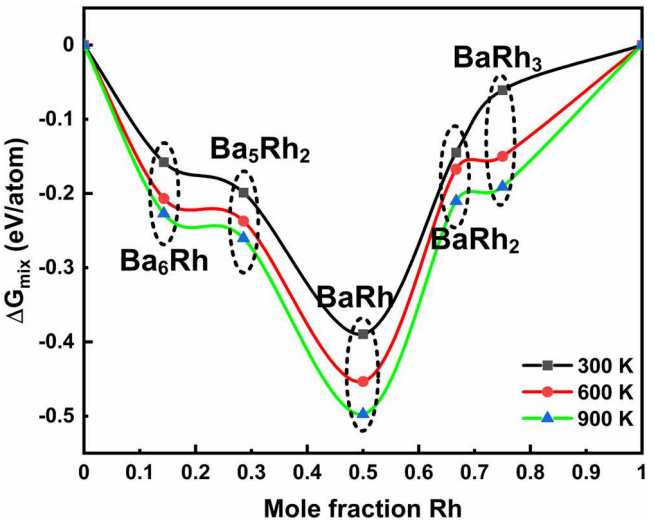

Figure 9. Plot of ΔG_{mix} versus mole fraction of Rh for temperatures 300 K, 600 K, and 900 K.

3.3.6. Determination of melting points at different compositions

MD simulation has been used to calculate the melting points of the Rh-Ba alloy system at different compositions using the solid–liquid coexistence method [78]. Different composition structures have been made using the MD code. Firstly, the NPT ensemble has been

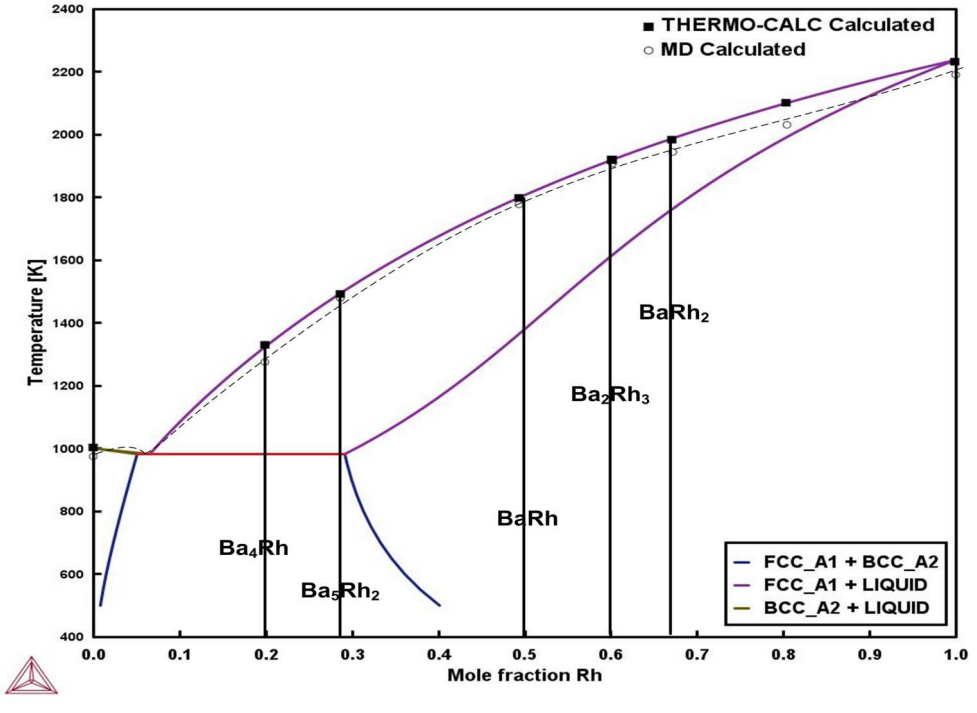

Figure 10. Melting points calculation of the Rh-Ba alloy system using THERMO-CALC [28] and MD simulation. Dashed line represents the MD-calculated liquidus line.

carried out to guess the melting point using the slope change method or the phase change curve method. Thereafter, the NVT ensemble is applied at a temperature over the guessed melting point to get the liquid phase. Then, the creation of a solid–liquid coexistence material system is done, and the NPT ensemble is performed on liquid atoms to the guessed melting point. Finally, equilibration to the desired melting point is carried out as suggested in the literature [79]. Several iterations have been carried out to minimise errors in the determination of melting points. Finally, a liquidus line of the Rh-Ba alloy system has been created using those melting points as obtained through MD simulation and validated with the approximate liquidus line of the system as obtained from THERMO-CALC [28], as depicted in Figure 10. FACTSAGE [80] also generates a similar diagram for this alloy system. Known phases are shown in the diagram. This approximate phase curve is considered, as no phase diagram exists for this alloy system. An approximate phase diagram is also reported for the Pd-Ba alloy [81]. It is clear from the figure that slight deviations in melting points at different compositions have been found, which is because of the defects in the material, as justified in [78]. Overall, a closer agreement between MD simulation and THERMO-CALC [28] for the liquidus line of the Rh-Ba alloy system has been observed.

4. Conclusions

Implementing the DFT datasets into the force-matching programme, the EAM potential for the Rh-Ba alloy system has been generated in order to examine the diffusional characteristics of the C15 $BaRh_2$ laves phase compound, determine the melting points at different compositions, and predict the phase stability at different temperatures of the Rh-Ba alloy system. Additionally, lattice thermal conductivity, radial distribution characteristics, and virtual XRD spectra of the $BaRh_2$ crystal have been reported in our paper to understand some other crystal insights. The performance of the EAM potential has been analysed by evaluating the density, cohesive energy, elastic properties, thermal expansion coefficient, surface energy, and point defect formation energy through MD simulation and verifying these properties using DFT analysis. A good match between MD and DFT results has been noted while examining these properties, except for C_{44}, and the octahedral interstitial formation energy of barium, which will be considered in future interatomic potential development. The EAM potential performs better than the aforementioned universal ML-based potential in terms of accuracy and speed, which justifies the need for the developed potential in order to study the concerned alloy system. The presence of (2 2 0), (3 1 1), (4 0 0), (4 2 2), (5 1 1), and (4 4 0) planes in the XRD pattern as obtained through MD simulation is supported by the DFT-based analysis. Ba-Rh interaction is more probable than Ba-Ba and Rh-Rh interaction, as analysed from radial distribution characteristics. Diffusion is governed by Rh atoms, for both Ba and Rh monovacancy models, as examined from lnD versus $1000/T$ plot in the diffusional characteristics study. Melting points at different compositions of the Rh-Ba alloy system, as obtained through MD simulation, are relatively closer to the melting points as identified from the approximate phase diagram of this alloy system. Further research will be carried out in order to generate a DFT-based phase diagram. The phase stability study tells that the BaRh phase is the most stable phase among others, whose utilisation is still missing.

The developed EAM potential will surely advance computational research on the Rh-Ba alloy system by helping to investigate several metallurgical phenomena like nanoindentation, creep ratcheting, defect analysis, tensile testing, and many more. This paper helps researchers to think of using the dominant thermodynamically favourable phase in several high-temperature engineering applications.

Acknowledgements

The Computer Center of the National Institute of Technology Rourkela is acknowledged for giving us a high-performance computing facility (HPCF) to carry out our research.

Author contributions

Sankhasubhra Mukhopadhyay: Conceptualisation, Methodology, Writing & review – original draft. Soumitra Kumar Dinda: Methodology, Discussion & review – original draft. Snehanshu Pal: Conceptualisation, Methodology, Writing & review – original draft.

Disclosure statement

No potential conflict of interest was reported by the author(s).

Data availability

Data sharing is applicable upon reasonable request to the corresponding author.

Declaration

On behalf of all authors, the corresponding author states that there are no competing interests to declare.

ORCID

Sankhasubhra Mukhopadhyay http://orcid.org/0009-0005-3573-1617
Snehanshu Pal http://orcid.org/0000-0002-4731-7107

References

[1] S. Xie, X.Y. Liu, and Y. Xia, *Shape-controlled syntheses of rhodium nanocrystals for the enhancement of their catalytic properties*. Nano Res. 8 (2015), pp. 82–96. doi:10.1007/s12274-014-0674-x.

[2] M. Jia, G. Jiang, H. Chen, Y. Pang, F. Yuan, Z. Zhang, N. Miao, C. Zheng, J. Song, Y. Li, and H. Wang, *Recent developments on processes for recovery of rhodium metal from spent catalysts*. Catalysts 12 (2022), pp. 1415. doi:10.3390/catal12111415.

[3] R.C. Ropp, *The alkaline earths as metals*, in *Encyclopedia of the Alkaline Earth Compounds*, R.C. Ropp, ed. author, Elsevier, Oxford, 2013. pp. 1–23. doi:10.1016/b978-0-444-59550-8.00001-6

[4] F. Stein and A. Leineweber, *Laves phases: A review of their functional and structural applications and an improved fundamental understanding of stability and properties*. J. Mater. Sci 56 (2021), pp. 5321–5427. doi:10.1007/s10853-020-05509-2.
[5] C. Gong, W. Qi, S. Wang, and H. Lei, *Superconducting properties of $MgCu_2$-type laves phase compounds $SrRh_2$ and $BaRh_2$*. J. Phys.: Condens. Matter 32 (2020), pp. 295601. doi:10.1088/1361-648X/ab7c12.
[6] Q.S. Yang, B.B. Ruan, M.H. Zhou, Y.D. Gu, M.W. Ma, G.F. Chen, and Z.A. Ren, *Superconducting properties of the C15-type laves phase $ZrIr_2$ with an Ir-based kagome lattice*. Chin. Phys. B 32 (2023), pp. 017402. doi:10.1088/1674-1056/aca3a2.
[7] A. Yakoubi, O. Baraka, and B. Bouhafs, *Structural and electronic properties of the laves phase based on rare earth type BaM2 (M = Rh, Pd, Pt)*. Results Phys. 2 (2012), pp. 58–65. doi:10.1016/j.rinp.2012.06.001.
[8] T. Ohta, Y. Nakagawa, Y. Kaneno, H. Inoue, T. Takasugi, and W.Y. Kim, *Microstructures and mechanical properties of $NbCr_2$ and $ZrCr_2$ laves phase alloys prepared by powder metallurgy*. J. Mater. Sci 38 (2003), pp. 657–665. doi:10.1023/A:1021807519728.
[9] M.R. Fellinger, H. Park, and J.W. Wilkins, *Force-matched embedded-atom method potential for niobium*. Phys. Rev. B Condens. Matter Mater. Phys 81 (2010), pp. 144119. doi:10.1103/PhysRevB.81.144119.
[10] A.F. Voter, *Interatomic potentials for atomistic simulations*. MRS Bull. 21 (1996), pp. 17–19. doi:10.1557/S0883769400046248.
[11] A. Oluwajobi and X. Chen, *The effect of interatomic potentials on the molecular dynamics simulation of nanometric machining*. Int. J. Autom. Comput 8 (2011), pp. 326–332. doi:10.1007/s11633-011-0588-y.
[12] I.M. Torrens, *Interatomic Potentials*, 1st ed, Academic Press, New York, 1972.
[13] Q.X. Pei, M.H. Jhon, S.S. Quek, and Z. Wu, *A systematic study of interatomic potentials for mechanical behaviours of Ti-Al alloys*. Comput. Mater. Sci 188 (2021), pp. 110239. doi:10.1016/j.commatsci.2020.110239.
[14] B. Mayer, H. Anton, E. Bott, M. Methfessel, J. Sticht, J. Harris, and P.C. Schmidt, *Ab-initio calculation of the elastic constants and thermal expansion coefficients of laves phases*. Intermetallics (Barking) 11 (2003), pp. 23–32. doi:10.1016/S0966-9795(02)00127-9.
[15] M.I. Mendelev, M. Asta, M.J. Rahman, and J.J. Hoyt, *Development of interatomic potentials appropriate for simulation of solid-liquid interface properties in Al-Mg alloys*. Philos. Mag 89 (2009), pp. 3269–3285. doi:10.1080/14786430903260727.
[16] M.I. Mendelev, M.J. Kramer, C.A. Becker, and M. Asta, *Analysis of semi-empirical interatomic potentials appropriate for simulation of crystalline and liquid Al and Cu*. Philos. Mag 88 (2008), pp. 1723–1750. doi:10.1080/14786430802206482.
[17] G.P. Purja Pun and Y. Mishin, *Development of an interatomic potential for the Ni-Al system*. Philos. Mag 89 (2009), pp. 3245–3267. doi:10.1080/14786430903258184.
[18] M.I. Mendelev, M.J. Kramer, S.G. Hao, K.M. Ho, and C.Z. Wang, *Development of interatomic potentials appropriate for simulation of liquid and glass properties of $NiZr_2$ alloy*. Philos. Mag 92 (2012), pp. 4454–4469. doi:10.1080/14786435.2012.712220.
[19] M.I. Mendelev, S. Han, D.J. Srolovitz, G.J. Ackland, D.Y. Sun, and M. Asta, *Development of new interatomic potentials appropriate for crystalline and liquid iron*. Philos. Mag 83 (2003), pp. 3977–3994. doi:10.1080/14786430310001613264.
[20] L.G. Zhou and H. Huang, *Response embedded atom method of interatomic potentials*. Phys. Rev. B Condens. Matter Mater. Phys 87 (2013), pp. 045431. doi:10.1103/PhysRevB.87.045431.
[21] M.S. Daw and M. Chandross, *Simple parameterization of embedded atom method potentials for FCC metals*. Acta Mater. 248 (2023), pp. 118771. doi:10.1016/j.actamat.2023.118771.
[22] A.F. Voter, *The embedded-atom method*, in *Intermetallic Compounds Vol.1 Principles*, J.H. Westbrook and R.L. Fleischer, eds., John Wiley & Sons Ltd., Chichester, 1994. pp. 77–90.
[23] P. Brommer, M.D. Boissieu, H. Euchner, S. Francoual, F. Gähler, M. Johnson, K. Parlinski, and K. Schmalzl, *Vibrational properties of $MgZn_2$. Z*. Kristallogr. Cryst. Mater 224 (2009), pp. 97–100. doi:10.1524/zkri.2009.1085.

[24] L.A. Heaton and A.J. Samin, *A first step towards understanding thermomechanical behavior of the Nb-Cr system through interatomic potential development and molecular dynamics simulations*. *Sci*. Rep 14 (2024), pp. 14408. doi:10.1038/s41598-024-64920-w.

[25] P. Giannozzi, O. Andreussi, T. Brumme, O. Bunau, M.B. Nardelli, M. Calandra, R. Car, C. Cavazzoni, D. Ceresoli, M. Cococcioni, N. Colonna, I. Carnimeo, A.D. Corso, S.D. Gironcoli, P. Delugas, R.A. Distasio Jr, A. Ferretti, A. Floris, G. Fratesi, G. Fugallo, R. Gebauer, U. Gerstmann, F. Giustino, T. Gorni, J. Jia, M. Kawamura, H.Y. Ko, A. Kokalj, E. Küçükbenli, M. Lazzeri, M. Marsili, N. Marzari, F. Mauri, N.L. Nguyen, H.V. Nguyen, A.O.D.L. Roza, L. Paulatto, S. Poncé, D. Rocca, R. Sabatini, B. Santra, M. Schlipf, A.P. Seitsonen, A. Smogunov, I. Timrov, T. Thonhauser, P. Umari, N. Vast, X. Wu, and S. Baroni, *Advanced capabilities for materials modelling with quantum espresso*. J. Phys.: Condens. Matter 29 (2017), pp. 465901. doi:10.1088/1361-648X/aa8f79.

[26] P. Giannozzi, S. Baroni, N. Bonini, M. Calandra, R. Car, C. Cavazzoni, D. Ceresoli, G.L. Chiarotti, M. Cococcioni, I. Dabo, A.D. Corso, S.D. Gironcoli, S. Fabris, G. Fratesi, R. Gebauer, U. Gerstmann, C. Gougoussis, A. Kokalj, M. Lazzeri, L.M. Samos, N. Marzari, F. Mauri, R. Mazzarello, S. Paolini, A. Pasquarello, L. Paulatto, C. Sbraccia, S. Scandolo, G. Sclauzero, A.P. Seitsonen, A. Smogunov, P. Umari, and R.M. Wentzcovitch, *Quantum espresso: A modular and open-source software project for quantum simulations of materials*. J. Phys.: Condens. Matter 21 (2009), pp. 395502. doi:10.1088/0953-8984/21/39/395502.

[27] A.P. Thompson, H.M. Aktulga, R. Berger, D.S. Bolintineanu, W.M. Brown, P.S. Crozier, P.J. 't Veld, A. Kohlmeyer, S.G. Moore, T.D. Nguyen, R. Shan, M.J. Stevens, J. Tranchida, C. Trott, and S.J. Plimpton, *Lammps – a flexible simulation tool for particle-based materials modeling at the atomic, meso, and continuum scales*. Comput. Phys. Commun 271 (2022), pp. 108171. doi:10.1016/j.cpc.2021.108171.

[28] J.O. Andersson, T. Helander, L.H. Höglund, P. Shi, and B. Sundman, *Thermo-calc & dictra, computational tools for materials science*. Calphad 26 (2002), pp. 273–312. doi:10.1016/S0364-5916(02)00037-8.

[29] Y. Mishin, M.J. Mehl, D.A. Papaconstantopoulos, A.F. Voter, and J.D. Kress, *Structural stability and lattice defects in copper: Ab initio, tight-binding, and embedded-atom calculations*. Phys. Rev. B Condens. Matter Mater. Phys 63 (2001), pp. 224106. doi:10.1103/PhysRevB.63.224106.

[30] D.E. Smirnova, A.Y. Kuksin, S.V. Starikov, V.V. Stegailov, Z. Insepov, J. Rest, and A.M. Yacout, *A ternary EAM interatomic potential for U-Mo alloys with xenon*. Model. Simul. Mater Sci. Eng 21 (2013), pp. 035011. doi:10.1088/0965-0393/21/3/035011.

[31] M. Ernzerhof and G.E. Scuseria, *Assessment of the Perdew-Burke-Ernzerhof exchange-correlation functional*. J. Chem. Phys 110 (1999), pp. 5029–5036. doi:10.1063/1.478401.

[32] P. E, Blöchl, *Projector augmented-wave method*. Phys. Rev. B Condens. Matter Mater. Phys 50 (1994), pp. 17953–17979. doi:10.1103/PhysRevB.50.17953.

[33] A.D. Corso, *Pseudopotentials periodic table: From H to Pu*. Comput. Mater. Sci 95 (2014), pp. 337–350. doi:10.1016/j.commatsci.2014.07.043.

[34] A. Jain, S.P. Ong, G. Hautier, W. Chen, W.D. Richards, S. Dacek, S. Cholia, D. Gunter, D. Skinner, G. Ceder, and K.A. Persson, *Commentary: The materials project: A materials genome approach to accelerating materials innovation*. APL Mater. 1 (2013), pp. 011002. doi:10.1063/1.4812323.

[35] S. Kirklin, J.E. Saal, B. Meredig, A. Thompson, J.W. Doak, M. Aykol, S. Rühl, and C. Wolverton, *The open quantum materials database (OQMD): Assessing the accuracy of DFT formation energies*. *NPJ*. Comput. Mater 1 (2015), pp. 15010. doi:10.1038/npjcompumats.2015.10.

[36] J.E. Saal, S. Kirklin, M. Aykol, B. Meredig, and C. Wolverton, *Materials design and discovery with high-throughput density functional theory: The open quantum materials database (OQMD)*. JOM 65 (2013), pp. 1501–1509. doi:10.1007/s11837-013-0755-4.

[37] P. Brommer, *Development and test of interaction potentials for complex metallic alloys*, Ph.D. diss., University of Stuttgart, Germany, 2008. doi:10.18419/opus-4819.

[38] P. Brommer and F. Gähler, *Potfit: Effective potentials from ab initio data*. Model. Simul. Mater. Sci. Eng 15 (2007), pp. 295–304. doi:10.1088/0965-0393/15/3/008.
[39] Y.Q. Cheng, A.J. Cao, H.W. Sheng, and E. Ma, *Local order influences initiation of plastic flow in metallic glass: Effects of alloy composition and sample cooling history*. Acta Mater. 56 (2008), pp. 5263–5275. doi:10.1016/j.actamat.2008.07.011.
[40] S. Xu, X. Fan, C. Gu, W. Zheng, and D.J. Singh, *Molecular dynamics study of the tensile properties of gold nanocrystalline films irradiated by gallium ions*. J. Nucl. Mater 581 (2023), pp. 154448. doi:10.1016/j.jnucmat.2023.154448.
[41] S. Starikov and D. Smirnova, *Optimized interatomic potential for atomistic simulation of Zr-Nb alloy*. Comput. Mater. Sci 197 (2021), pp. 110581. doi:10.1016/j.commatsci.2021.110581.
[42] F. Ercolessi and J.B. Adams, *Interatomic potentials from first-principles calculations: The force-matching method. Europhys*. Lett 26 (1994), pp. 583–588. doi:10.1209/0295-5075/26/8/005.
[43] Y. Mishin, D. Farkas, M.J. Mehl, and D.A. Papaconstantopoulos, *Interatomic potentials for Al and Ni from experimental data and ab initio calculations*. Mater. Res. Soc. Symp. Proc 538 (1999), pp. 535–540. doi:10.1557/PROC-538-535.
[44] M.S. Daw and M. Chandross, *Simple parameterization of embedded atom method potentials for FCC alloys*. Acta Mater. 248 (2023), pp. 118772. doi:10.1016/j.actamat.2023.118772.
[45] M.J.D. Powell, *A method for minimizing a sum of squares of non-linear functions without calculating derivatives*. Comput. J 7 (1965), pp. 303–307. doi:10.1093/comjnl/7.4.303.
[46] H. Mu, B. Xu, C. Ouyang, and X. Lei, *Highly optimized embedding atom method potential for Pt-Cu alloys. J Alloys*. Compd 696 (2017), pp. 470–480. doi:10.1016/j.jallcom.2016.11.291.
[47] B. Onat and S. Durukanoğlu, *An optimized interatomic potential for Cu-Ni alloys with the embedded-atom method*. J. Phys.: Condens. Matter 26 (2014), pp. 035404. doi:10.1088/0953-8984/26/3/035404.
[48] P. Hirel, *Atomsk: A tool for manipulating and converting atomic data files*. Comput. Phys. Commun 197 (2015), pp. 212–219. doi:10.1016/j.cpc.2015.07.012.
[49] T.M. Project, *Materials data on $BaRh_2$ by materials project*, DOE Data Explorer, United States, 2020; dataset available at doi:10.17188/1274434.
[50] W.M. Haynes, D.R. Lide, and T.J. Bruno, *CRC Handbook of Chemistry and Physics, 95th ed*, CRC Press, Boca Raton, 2014.
[51] T.M. Project. *Materials data on $BaRh_2$ by materials project*. Available at https://legacy.materialsproject.org/materials/mp-568430/.
[52] C. Vailhé and D. Farkas, *Shear faults and dislocation core structures in B2 CoAl*. J. Mater. Res 12 (1997), pp. 2559–2570. doi:10.1557/JMR.1997.0340.
[53] K. Moriguchi and M. Igarashi, *Correlation between lattice-strain energetics and melting properties: molecular dynamics and lattice dynamics using EAM models of Al*. Phys. Rev. B Condens. Matter Mater. Phys 74 (2006), pp. 024111. doi:10.1103/PhysRevB.74.024111.
[54] E. Symianakis and A. Kucernak, *Embedded atom method interatomic potentials fitted upon density functional theory calculations for the simulation of binary Pt-Ni nanoparticles*. Comput. Mater. Sci 133 (2017), pp. 185–193. doi:10.1016/j.commatsci.2017.03.020.
[55] C. Kittel, *Crystal binding and elastic constants*, in *Introduction to Solid State Physics*, in S. Johnson, P. McFadden, and M. Batey, eds., John Wiley & Sons Inc., Hoboken, NJ, 2005. pp. 47–85.
[56] A.O.D.L. Roza, D.A. Pérez, and V. Luaña, *Gibbs2: A new version of the quasiharmonic model code. II. Models for solid-state thermodynamics, features and implementation*. Comput. Phys. Commun 182 (2011), pp. 2232–2248. doi:10.1016/j.cpc.2011.05.009.
[57] X. Gong and A.D. Corso, *Ab initio quasi-harmonic thermoelasticity of molybdenum at high temperature and pressure*. J. Chem. Phys 160 (2024), pp. 244703. doi:10.1063/5.0212162.
[58] B. Samanta and A. Jain, *Experimental investigation of lattice thermal expansion and specific heat capacity of C15 – Cr_2Zr laves phase intermetallic compound by HTXRD and DSC*. Intermetallics (Barking) 148 (2022), pp. 107634. doi:10.1016/j.intermet.2022.107634.
[59] L.M. Hale. *Surface_energy_static – methodology and code*. Available at https://www.ctcms.nist.gov/potentials/iprPy/notebook/surface_energy_static.html.

[60] R. Tran, Z. Xu, B. Radhakrishnan, D. Winston, W. Sun, K.A. Persson, and S.P. Ong, *Data descriptor: surface energies of elemental crystals*. *Sci*. Data 3 (2016), pp. 160080. doi:10.1038/sdata.2016.80.
[61] M.R. Karim, S. Taylor, F. Akasheh, and M.A. Tschopp. *Lammps vacancy formation energy*. Available at https://www.cavs.msstate.edu/icme/code/lammps/tutorials/lammps/vacancy.php.
[62] S. Taylor, F. Akasheh, and M.A. Tschopp. *Lammps interstitial fault energy*. Available at https://www.cavs.msstate.edu/icme/code/lammps/tutorials/lammps/interstitial.php.
[63] A. Togo, L. Chaput, T. Tadano, and I. Tanaka, *Implementation strategies in phonopy and phono3py*. J. Phys.: Condens. Matter 35 (2023), pp. 353001. doi:10.1088/1361-648X/acd831.
[64] J. Li, T. Shi, C. Zhang, P. Zhang, S.A. Ibrahim, Z. Sun, Y. Li, C. Tang, Q. Peng, and C. Lu, *A comparative study on force-fields for interstitial diffusion in α-Zr and Zr alloys*. Materials. (Basel) 17 (2024), pp. 3634. doi:10.3390/ma17153634.
[65] W. Hu, X. Shu, and B. Zhang, *Point-defect properties in body-centered cubic transition metals with analytic EAM interatomic potentials*. Comput. Mater. Sci 23 (2002), pp. 175–189. doi:10.1016/S0927-0256(01)00238-5.
[66] T. Kumagai, D. Nikkuni, S. Hara, S. Izumi, and S. Sakai, *Development of interatomic potential for Zr-Ni amorphous systems*. *Mater*. Trans 48 (2007), pp. 1313–1321. doi:10.2320/matertrans.MF200602.
[67] P.W. Ma and S.L. Dudarev, *Nonuniversal structure of point defects in face-centered cubic metals*. Phys. Rev. Mater 5 (2021), pp. 013601. doi:10.1103/PhysRevMaterials.5.013601.
[68] A. Mazitov, F. Bigi, M. Kellner, P. Pegolo, D. Tisi, G. Fraux, S. Pozdnyakov, P. Loche, and M. Ceriotti, *Pet-mad, a lightweight universal interatomic potential for advanced materials modeling*. (2025), pp. 1–29. doi:10.48550/arXiv.2503.14118.
[69] D. Surblys, H. Matsubara, G. Kikugawa, and T. Ohara, *Application of atomic stress to compute heat flux via molecular dynamics for systems with many-body interactions*. Phys. Rev. E 99 (2019), pp. 051301. doi:10.1103/PhysRevE.99.051301.
[70] P. Roy Chowdhury, T. Feng, and X. Ruan, *Development of interatomic potentials for the complex binary compound Sb_2Te_3 and the prediction of thermal conductivity*. Phys. Rev. B Condens. Matter Mater. Phys 99 (2019), pp. 155202. doi:10.1103/PhysRevB.99.155202.
[71] A. Stukowski, *Visualization and analysis of atomistic simulation data with ovito-the open visualization tool*. Model. Simul. Mater. Sci. Eng 18 (2010), pp. 015012. doi:10.1088/0965-0393/18/1/015012.
[72] N.H. Duc and P.E. Brommer, *Formation of 3d-moments and spin fluctuations in the rare earth-transition metal intermetallics*, in *Advanced Magnetism and Magnetic Materials, Volume 1 Aspects of Rare Earth – Transition Metal Intermetallics*, N.H. Duc, ed., Vietnam National University Press, Hanoi, 2014. pp. 99–264.
[73] M. Denkinger and H. Mehrer, *Diffusion in the C15-type intermetallic laves phase $NbCo_2$*. *Philos*. Mag. A 80 (2000), pp. 1245–1263. doi:10.1080/01418610008212113.
[74] D.O. Poletaev, A.G. Lipnitskii, V.N. Maksimenko, Y.R. Kolobov, A.G. Beresnev, and M.S. Gusakov, *The N-body interatomic potentials for molecular dynamics simulations of diffusion in C15 Cr_2Ta laves phase*. Comput. Mater. Sci 216 (2023), pp. 111841. doi:10.1016/j.commatsci.2022.111841.
[75] Š Svoboda, M. Lebeda, P. Vlčák, Z. Budinská, and J. Drahokoupil, *Molecular dynamics simulation of the diffusion behaviour in Ti – Ag using diffusion couple method*. Results Phys. 64 (2024), pp. 107943. doi:10.1016/j.rinp.2024.107943.
[76] S. Menon, Y. Lysogorskiy, J. Rogal, and R. Drautz, *Automated free-energy calculation from atomistic simulations*. Phys. Rev. Mater 5 (2021), pp. 103801. doi:10.1103/PhysRevMaterials.5.103801.
[77] V.I. Ivashchenko, P.E.A. Turchi, and V.I. Shevchenko, *First-principles study of elastic and stability properties of ZrC-ZrN and ZrC-TiC alloys*. J. Phys.: Condens. Matter 21 (2009), pp. 395503. doi:10.1088/0953-8984/21/39/395503.

[78] A. Arkundato, W. Maulina, L. Rohman, R.D. Syarifah, and M.A. Shafii, *Rigid Procedure to calculate the melting point of metal using the solid-liquid phase (coexistence) method*. JIF 14 (2022), pp. 132–140. doi:10.25077/jif.14.2.132-140.2022.

[79] A.B. Weidmann, L.F.M. Franco, A.K. Sum, and P.A.P. Filho, *Dissociation temperature of gas hydrates through isenthalpic-isobaric molecular dynamics simulations*. J. Chem. Phys 161 (2024), pp. 174505. doi:10.1063/5.0234866.

[80] C.W. Bale, E. Bélisle, P. Chartrand, S.A. Decterov, G. Eriksson, A.E. Gheribi, K. Hack, I.H. Jung, Y.B. Kang, J. Melançon, A.D. Pelton, S. Petersen, C. Robelin, J. Sangster, P. Spencer, and M.A. Van Ende, *Factsage thermochemical software and databases, 2010-2016*. Calphad 54 (2016), pp. 35–53. doi:10.1016/j.calphad.2016.05.002.

[81] S. Pal and S. Mukhopadhyay, *Development of embedded-atom method (EAM) potential for Palladium – Barium alloy*. *Mol.* Simul 50 (2024), pp. 991–1000. doi:10.1080/08927022.2024.2376327.

PHILOSOPHICAL MAGAZINE

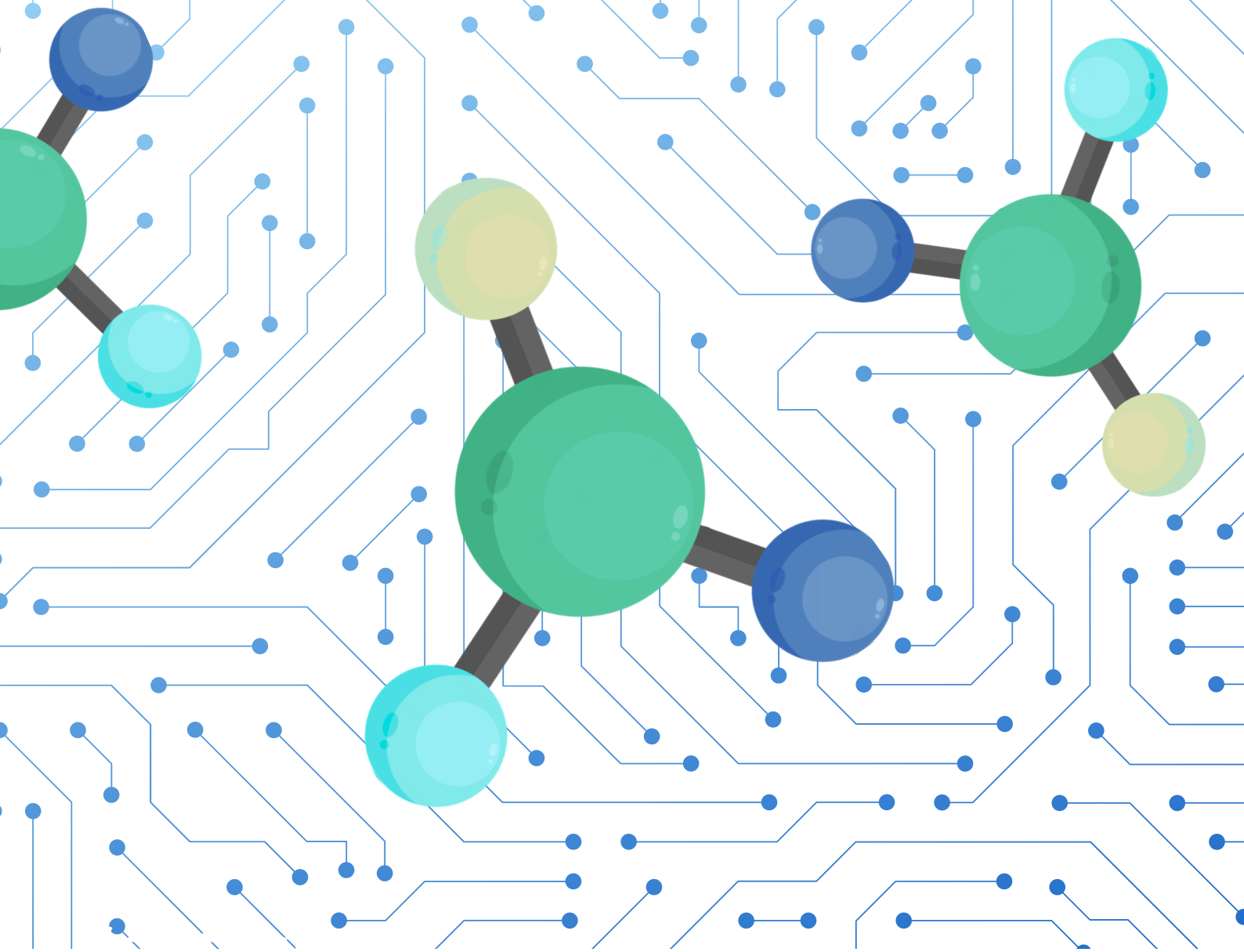

Editorial Department | digitaleditor@philosophicalmagazine.com

Taylor & Francis
by informa